Post-Detonation Afterburning of High Explosives

Fedina, Katja

2017

Document Version:
Publisher's PDF, also known as Version of record

Post-Detonation Afterburning of High Explosives

EKATERINA FEDINA
DEPARTMENT OF ENERGY SCIENCE | FACULTY OF ENGINEERING | LUND UNIVERSITY

Post-Detonation Afterburning of High Explosives

Post-Detonation Afterburning of High Explosives

Ekaterina Fedina

LUND
UNIVERSITY

Thesis for the degree of Doctor of Philosophy in Engineering
Thesis advisors: Prof. Xue-Song Bai, Prof. Christer Fureby
Faculty opponent: Prof. Elaine Oran

To be presented, with the permission of the Faculty of Engineering of Lund University, for public criticism in the Lecture hall M:B, M-building, Ole Römers väg 1, Lund on Friday, 25th of August 2017 at 10:00.

Organization	Document name
LUND UNIVERSITY Division of Fluid Mechanics Department of Energy Sciences Box 43 221 00, Lund, Sweden	DOCTORAL DISSERTATION
	Date of issue June 2017
	Sponsoring organization Swedish Defence Research Agency - FOI
Author(s) Ekaterina Fedina	

Title and subtitle

Post-Detonation Afterburning of High Explosives

Abstract

High performance of an explosive compound with respect to afterburning requires sufficient combustible properties of the explosive, and a careful determination of the most appropriate charge positioning to achieve the desired afterburning effect. Understanding the physical processes of post-detonation afterburning and how these are affected by the surroundings, e.g. the Height of Burst (HoB), facilitates the optimal use of the explosive and also helps in designing protection against it. The use of Large Eddy Simulation (LES) for investigating afterburning properties of an explosive charge can be a cost effective approach to identify the most optimal conditions for subsequent full-scale experiments. Of particular interest are Enhanced Blast eXplosives (EBX), to which metal particles, usually aluminium, are added to the explosive compound in order to increase the afterburning energy release by allowing the metal particles and detonation products combust with air. This presents a further modelling challenge since the combustion becomes multi-phased.

This thesis presents modelling, simulation and experimental efforts in studying this two-phase post-detonation combustion event at different HoB of 1 kg trinitrotoluene (TNT) and TNT/aluminium charges. The main objectives of this work is to demonstrate the use of LES with finite rate chemistry for these types of applications, to elucidate the physical processes involved in near-ground air blasts, to demonstrate what effects the HoB has on the afterburning, and how aluminium particles affect the combustion.

Simulation results, supported by experimental data, show that the main mechanism responsible for the mixing, and therefore afterburning, is the rise of hydrodynamic instabilities, which trigger the build up of a mixing layer. Shock-mixing layer interactions further create more instabilities. Thus, in order to achieve maximum effect of the afterburning during an explosive blast, the existence of a turbulent mixing layer has to be combined with repeated shock propagation through it, by which the duration of the afterburning is maintained. The presence of reacting particles increases the vorticity generated by instabilities since the particles create perturbations in the detonation product cloud, hence disrupting the alignment of the pressure and density gradients. Burning particles intensify mixing even further through volumetric expansion induced by increased heat-release from particle combustion. The mixing intensity in its turn varies with HoB, as the shock propagation pattern is different for all HoB, which means that in order to achieve maximum effect from aluminium inclusion to an explosive, HoB must be considered as a parameter.

Key words: Explosives, combustion, aluminium, LES

Classification system and/or index termes (if any):

Supplementary bibliographical information:	Language
ISSN and key title: 0282-1990	ISBN 978-91-629-0221-6
Recipient's notes	Number of pages / Price
	Security classification

Post-Detonation Afterburning of High Explosives

Ekaterina Fedina

LUND
UNIVERSITY

Faculty Opponent

Prof. Elaine Oran
Department of Aerospace Engineering
University of Maryland, USA

Examination Committee

Dr. Olga Roditcheva
Volvo Car Corporation
NVH Centrum
PVT2C2, Gothenburg, Sweden

Prof. Mirko Salewski,
Technical University of Denmark
Department of Physics
Fysikvej, Building 309, 2800 Kgs. Lyngby, Denmark

Ass. Prof. Geert Brethouwer
Royal Institute of Technology, KTH
Department of Mechanics,
Osquars Backe 18, SE-100 44, Stockholm, Sweden

Deputy member:
Dr. Sven-Inge Möller
Lund Institute of Technology, LTH
Combustion Physics
Professorsgatan 1, Box 118, SE-221 00, Lund, Sweden

Faculty of Engineering , Department of Energy Science
ISBN: 978-91-629-0221-6 (print)
ISBN: 978-91-629-0222-3 (pdf)
ISSN: 0282-1990
ISRN: LUTMDN/TMHP-17/1132-SE
Printed in Sweden by Media-Tryck, Lund University, Lund 2017

Contents

Populärvetenskaplig sammanfattning

I en allt osäkrare värld, blir det desto viktigare att förstå hur man kan försvara sig mot hot. Arbetet som denna avhandling bygger på, handlar om att studera efterförbränning vid explosioner. Det vill säga, hur eldmolnet som bildas när ett visst sprängämne detonerar påverkas av sprängämnets typ och innehåll samt position. Genom att kunna förutsäga efterverkan från en given stridsdel kan man bättre utveckla skydd mot denna.

Sprängämnen innehåller en avsevärd mängd energi som frigörs bakom detonationsfronten och för att kunna bestämma dessa sprängämnens prestanda i olika omgivningar krävs att även efterförbränningsförloppet kan studeras i detalj. Som typexempel kan nämnas sprängämnen med negativ syrebalans (t.ex. trotyl – TNT), dessa sprängämnen innehåller för lite syre i sig och kan därför inte förbrännas helt vid detonation. Om ett sådant sprängämne detonerar i en luftomgivning, möjliggörs ytterligare förbränning då de bränslerika detonationsprodukterna blandas och förbränns med syret i omgivningens luft.

På senare tid har tryckverkande stridsdelar väckt allt större intresse, till stor del beroende på ökad förekomst av så kallade termobariska stridsdelar. Sprängämnet i dessa är av flera skäl komplicerade att prestandabestämma. En orsak till detta är att tryckverkan är en långsammare process än själva detonationen eftersom de bränslerika spränggaserna får möjlighet att förbrännas partiellt eller fullständigt med omgivande luft. Detta ger en ökning av tryckverkan jämfört med vad som skulle vara fallet om ingen efterförbränning skedde. För att ytterligare öka tryckverkan tillsätts ofta extra bränsle, som i de flesta fall består av mycket finkornigt aluminiumpulver. Dessa aluminiumpartiklar avger energi då de oxideras och dynamiken mellan spränggaser och partiklar i ett tidigt skede av explosionen kan öka laddningens verkan. En förutsättning för att efterförbränningen ska ske är dock att bränslet (spränggaser och aluminium) och luftens syre blandas om, samt att blandningen har tillräckligt hög temperatur. En fri laddning som detonerar i luft bildar ofta ett pulserande eldklot, där omblandningen med syret i luften inte är effektiv, vilket i sin tur leder till att eldklotet relativt snabbt kyls av. Om samma laddning detonerar nära marken eller en vägg, eller i en tunnel, kommer en effektivare omblandning att ske vilket leder till bättre förbränning och större verkan. Dessa omständigheter gör att verkan inte bara beror på sprängämnet utan även på omgivningen och hur dessa växelverkar.

För att bestämma verkan vid en given situation är det således nödvändigt att kunna modellera efterförbränningsprocessen detaljerat, exempelvis med avancerade beräkningsme-

toder. Syftet med detta arbete har varit att ta fram en beräkningsmodell för efterförbränning och implementera modellen i beräkningsverktyget OpenFOAM[1]. Kraven på modellen har varit att den ska kunna hantera stötvågsutbredning och förbränning av spränggaser med luft och aluminiumpartiklar.

Avhandlingen beskriver denna beräkningsmodell och olika tillämpningar av denna på efterförbränning vid explosion av 1 kg TNT och 1 kg TNT med aluminium. Explosionerna sker på fyra olika höjder ovanför marken, 0.15 m, 0.50 m, 1.0 m, och 2.0 m. Dessutom har en serie experiment med TNT-laddningar med och utan aluminiumpartiklar utförts för att validera beräkningsverktyget. I experimenten sprängdes laddningarna vid samma höjder som i simuleringarna för att vidare studera inverkan av markreflexer på efterförbränningen.

Analysen av beräknings och experimentdata har visat att man får en förstärkt verkan vid inblandning av aluminium. Förutsättningen för en långvarig efterförbränning har visat sig vara en bra omblandning av luft, spränggaser och aluminium. Detta sker på ett optimalt avstånd från marken, då den markreflekterade detonationsvågen hjälper till att blanda om gaserna.

[1] www.openfoam.org

Abstract

High performance of an explosive compound with respect to afterburning requires sufficient combustible properties of the explosive, and a careful determination of the most appropriate charge positioning to achieve the desired afterburning effect. Understanding the physical processes of post-detonation afterburning and how these are affected by the surroundings, e.g. the Height of Burst (HoB), facilitates the optimal use of the explosive and also helps in designing protection against it. The use of Large Eddy Simulation (LES) for investigating afterburning properties of an explosive charge can be a cost effective approach to identify the most optimal conditions for subsequent full-scale experiments. Of particular interest are Enhanced Blast eXplosives (EBX), to which metal particles, usually aluminium, are added to the explosive compound in order to increase the afterburning energy release by allowing the metal particles and detonation products combust with air. This presents a further modelling challenge since the combustion becomes multi-phased.

This thesis presents modelling, simulation and experimental efforts in studying this two-phase post-detonation combustion event at different HoB of 1 kg trinitrotoluene (TNT) and TNT/aluminium charges. The main objectives of this work is to demonstrate the use of LES with finite rate chemistry for these types of applications, to elucidate the physical processes involved in near-ground air blasts, to demonstrate what effects the HoB has on the afterburning, and how aluminium particles affect the combustion.

Simulation results, supported by experimental data, show that the main mechanism responsible for the mixing, and therefore afterburning, is the rise of hydrodynamic instabilities, which trigger the build up of a mixing layer. Shock-mixing layer interactions further create more instabilities. Thus, in order to achieve maximum effect of the afterburning during an explosive blast, the existence of a turbulent mixing layer has to be combined with repeated shock propagation through it, by which the duration of the afterburning is maintained. The presence of reacting particles increases the vorticity generated by instabilities since the particles create perturbations in the detonation product cloud, hence disrupting the alignment of the pressure and density gradients. Burning particles intensify mixing even further through volumetric expansion induced by increased heat-release from particle combustion. The mixing intensity in its turn varies with HoB, as the shock propagation pattern is different for all HoB, which means that in order to achieve maximum effect from aluminium inclusion to an explosive, HoB must be considered as a parameter.

List of Publications

This thesis is based on the following publications:

I **Predicting Mixing and Combustion in the Afterburn Stage of Air Blasts**

E. Fedina, C. Fureby, A. Helte (2010)
48th AIAA Aerospace Sciences Meeting Including the New Horizons Forum and Aerospace Exposition, 4 - 7 January 2010, Orlando, Florida,
AIAA - 2010-773

II **Numerical Simulation of Afterburning During Explosions**

E. Fedina, C. Fureby (2011)
28th International Symposium on Shock Waves
17 - 22 July 2011, Manchester, UK

III **Investigating Ground Effects on Mixing and Afterburning During a TNT Explosion**

E. Fedina, C. Fureby (2013)
Shock Waves, vol. 23, pp. 251–-261

IV **Combustion in Afterburning Behind Explosive Blasts**

E. Fedina, K.C. Gottiparthi, C. Fureby, S. Menon (2016)
in *Coarse Grained Simulation and Turbulent Mixing*,
Ed. F.F. Grinstein, Cambridge University Press, New York, USA, pp. 393–432

V **Analysis of Heat-Release During TNT/Aluminum Afterburning by Means of Numerical Simulations**

E. Fedina, C. Fureby (2017)
Proceedings of the Combustion Institute, vol. 36, pp. 2841–-2848

Other Publications

Conference Papers

- E. Fedina, C. Fureby, V. Sabelnikov & J. Tegnér; 2009, "On the Sensitivity to Subgrid Turbulence Chemistry Interaction Models in Large Eddy Simulation of Self-Ignition in Hot Confined Supersonic Airflow", 6^{th} Mediterranean Combustion Symposium.

- Berglund M., E. Fedina, C. Fureby, V. Sabelnikov & Tegnér J.; 2009, "On the Influence of Finite rate Chemistry in LES of Self-Ignition in Hot Confined Supersonic Airflow", 6^{th} European Symp. on Aerothermodynamics for Space Vehicles, Verseilles, France. In ESA Special Publication SP-659.

- E. Fedina, C. Fureby, V. Sabelnikov & Tegnér J.; 2009, "Large Eddy Simulation of High Speed Combustion", Joint Meeting of the Scandinavian-Nordic and French Sections of the Combustion Institute Copenhagen, 9-10 November.

- M. Chapius, C. Fureby, E. Fedina, N. Alin, J. Tegnér; 2010, "LES Modeling of Combustion for Propultions Applications Using OpenFOAM". ECCOMAS 2010.

- C. Fureby, E. Fedina; 2010, "A Computational Study of Multi-Burner Annual Aero Gas Turbine", 27^{th} International Congress of the Auronautical Sciences (ICAS 2010).

- L. Sjöqvist, M. Henriksson, E. Fedina, C. Fureby; 2010 "Numerical Laser Beam Propagation using a Large Eddy Simulation Refractive Index Field Representing a Jet Engine Exhaust" SPIE Security & Defence, Technologies for Optical countermeasures VII), (p. 78360K-1-78360K-12).

- E. Fedina, C. Fureby, S.A. Borzov, V.N. Gusev, T.S. Stepanova; 2011, "Combustion LES of CESAR Multi-Burner Annular Combustor", AIAA-2011-785.

- E. Fedina, C. Fureby; 2012, "Numerical Simulations of TNT Afterburning at Different Heights of Blast", 22^{nd} Military Aspects on Blast and Shock (MABS), 4-9 November, Bourgues, France.

- E. Fedina, C. Fureby; 2013, "The Effect of an Equation of State on the Afterburning of TNT Afterburning at Different Heights of Blast", European Combustion Meeting 2013 (ECM2013), 26-28 June, Lund, Sweden.
- E. Fedina, C. Fureby; 2015, "Effect of Aluminium Combustion on TNT Air Blasts", 46^{th} International Annular Conference of ICT, 23-26 June, Karlsruhe, Germany.
- N. Zettervall, E. Fedina, K. Nordin-Bates, E. Heimdal Nilsson, and C. Fureby; 2015, "Combustion LES of a Multi-Burner Annular Aeroengine Combustor using a Skeletal Reaction Mechanism for Jet-A Air Mixtures", AIAA-2015-4020.

Journal Papers

- E. Lindborg, E. Fedina; 2009, "Vertical Turbulent Diffusion in Stably Stratified Flows", Geophysical Research Letters, **36**, L01605.
- M. Berglund, E. Fedina, C. Fureby, V. Sabelnikov & J. Tegnér; 2010, "Finite Rate Chemistry Large-Eddy Simulation of Self-Ignition in Supersonic Combustion Ramjet", AIAA.J., **48**, p 540.
- E. Fedina, C. Fureby; 2011, "A Comperative Study of Flamelet and Finite Rate Chemistry LES for an Axisymetric Dump Combustor", Journal of Turbulence, **12**, p. N24.
- C. Fureby, M. Chapius, E. Fedina, S. Karl; 2011, "CFD Analysis of the HyShot II Scramjet Combustor", Proc. Comb. Inst., **33**, p. 2399.
- M. Chapius, E. Fedina, C. Fureby, K. Hannemann, S. Karl, J. Martinez Schramm; 2013, "A Computational Study of HyShot II Combustor Performance", Proc. Comb. Inst., **34**, p. 2101.
- C. Fureby, E. Fedina, J. Tegnér; 2014, "A Computational Study of Supersonic Combustion Relevant to Air-breathing Engines", Shock Waves, **24**, p. 41.
- G. Bulat, E. Fedina, C. Fureby, W. Meier, U. Stopper; 2015, "Reacting Flow in an Industrial Gas Turbine Combustor: LES and Experimental Analysis", Proc. Comb. Inst. **35**, p. 3175.
- E. Fedina, C. Fureby, G. Bulat, W. Meier; 2017 "Assessment of Finite Rate Chemistry Large Eddy Simulation Combustion Models", submitted to Flow, Turbulence and Combustion

FOI-Internal Report

E. Fedina; 2014, "TNT/Aluminium Afterburning in Air Blasts", FOI-R-3913—SE

Glossary

As an introduction to the subject of post-detonation afterburning of explosives, some commonly used terms, concepts and abbreviations are clarified:

Energetic material: materials that store high amount of chemical energy.

High Explosive: energetic materials that detonate (contrary to deflagrate (burn), such as propellants).

Afterburning: Post-detonation combustion of detonation products (e.g. C, CO, CO_2) with air (O_2).

EBX: Enhance Blast eXplosive, a high explosive containing reacting metal particles for an enhanced blast effect.

TBX: ThermoBaric eXplosive, an explosive with both temperaure and pressure (blast) effects (from latin: 'Thermo'-heat, 'baric'-pressure). Generally consist of a high-explosive core surrounded by a secondary, fuel rich charge.

HoB: Height of Burst.

TNT: 2,4,6-Tri-Nitro-Toluene, high explosive.

NM: Nitromethane, high explosive.

C4: Composition 4, high explosive.

IEF: Improvised Explosive Formulation.

Al: Aluminium.

RT: Rayleigh-Taylor instastability, [1]. Arises to when a contact surface between two fluids with different densities is impulsively accelerated.

RM: Richtmeyer-Meshkov instability, [2]. Arises when pressure and density gradients are not parallel.

Chapter 1

Introduction

For well over a century various applications in mining, construction and weapon development have promoted studies of high explosive performance. The physical complexity of detonation of an explosive charge and the post-detonation flow, involving extremely high pressures and temperatures, phase transitions, turbulence, shocks, mixing, instabilities, chemical reactions and shock-turbulence interactions puts very high demands on the physical modelling and the numerical simulation techniques, not to mention an experimental set-up and measurement techniques. The task of researching these events is daunting.

During the early stages of a post-detonation of a high explosive, the explosive material is rapidly converted to a hot, dense, high-pressure gas. The explosion products expand at high velocities causing a radially expanding shock wave. Only a small part of the stored chemical energy is released in the detonation process itself. The remaining energy is dissipated more slowly as the detonation product cloud expands, and the detonation products mix with the ambient air and subsequently burn. This post-detonation afterburning process has little effect on the initial blast wave because it occurs much slower than the original detonation. However, later stages of the blast wave can be affected by the afterburning, particularly for explosions in confined spaces, e.g. in tunnels and buildings, and in the proximity of the ground. Hence the afterburning can play a crucial role when evaluating the performance of an explosive compound, for both protection or offensive purposes.

The interest in understanding the effects of afterburning have increased with an increased use of EBX and TBX charges in combat. These explosives are devastating during post-detonation phases, due to afterburning, for both infrastructure and human lives. In EBX, metal particles, usually aluminium, are added to the explosive compound in order to increase the afterburning energy release by allowing the metal particles and detonation products combust with air. This presents another modelling challenge since the combustion becomes two-phased.

The purpose of this work is to be able to evaluate the performance of high explosives. This thesis aims to contribute with developing knowledge about the theory and modelling of the afterburning of high explosive detonation products with and without the addition

of particles to the explosive compound.

To reach this, the following tasks were posed at the beginning of this work:

- Develop and implement a two-phase code in OpenFOAM, [3, 4];
- The code should be able to handle post-detonation flow, including shocks, turbulence, combustion and motion and burning of aluminium particles;
- Validate the code against available experimental data,
- Simulate 1 kg TNT and 1 kg TNT/Al afterburning at different HoB and investigate the effects of Al addition to an explosive as well as the ground effects on flow and afterburning.

The outcome of finishing these tasks and the research results that accompanied, constitute this thesis, which is based on five papers I to V. Papers I and II deal with the homogeneous afterburning of TNT in unconfined conditions. Paper III deals with near-surface effect on flow and combustion of homogeneous TNT charge. Paper IV investigates the near-surface effects and the effects of Al inclusion. Paper V finishes with an in-depth analysis of the heat-release during TNT/Al afterbuning at different HoB.

Hence, Chapter 2 provides an overview of the general features of post-detonation flows. The modelling approaches are presented in Chapter 3 for the gas-phase and in Chapter 4 for solid-phase, respectively. The chemical kinetics employed through out this work are given in Chapter 5. Finally, the main simulation results are presented in Chapter 7. The key points are summarized and suggestions on future work are offered in Chapter 8.

This work has shown that the performance of high explosive with regards to afterburning varies depending on geometrical surroundings of the detonation. That is, different performance can be obtained if the same charge is detonated at different HoB. This effect is seen regardless of presence of Al particles, indicating that HoB must be considered as a parameter during performance evaluation of an explosive. Moreover, EBX simulations have shown it to be feasible to use LES with finite rate chemistry as a tool to investigate the problems.

Chapter 2

General Scenarios of Post-Detonation Afterburning

This chapter describes the three situations of the post-detonation afterburning that will be considered throughout this thesis. These are the *homogeneous afterburning* - when only the detonation products combust with air after the detonation, *heterogeneous afterburning* - when detonation products and metal particles burn with air after the detonation. Both homogeneous and heterogeneous afterburning can occur unconfined, i.e. in the open air/atmosphere, or confined, i.e., inside a closed room or chamber, or semi-confined, i.e. *near-surface afterburning*, e.g. above ground. In this chapter, a concise physical background is provided regarding these three 'scenarios' and previous work done by other authors in these fields is presented. The circle will be complete in Chapter 7 when the simulation results from this work will be presented for these three si.

Prior to detailing each of the scenarios, the conditions that need to be met for the post-detonation afterburning to occur, is briefly summarized in Fig. 2.1.

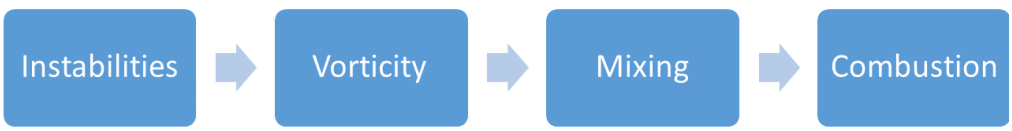

Figure 2.1: General mechanism of post-detonation afterburning.

More precisely, the detonation products must be mixed with an oxidizer to combust, and in afterburning during explosions this is usually attained by a type of hydrodynamic instability that generates vorticity, creating mixing, which then leads to combustion. What differs between the following scenarios is the way the instabilities are generated and the sustaining mechanism for the subsequent mixing. Also, as combustion can also occur with

the metal particles, another degree of complexity is added to the simple scheme in Fig. 2.1.

The research regarding afterburning from homogeneous and heterogeneous explosives have been conducted (in the open literature) by mainly five research groups. A.L Kuhl *et.al.* at Livermore in the USA, [5–21] , have conduted research on model development and small scale experiments for both homogeneous and heterogeneous explosives. D.L. Frost and F. Zhang *et.al.* at McGill University and Defence R&D in Canada, [21–35], have done a lot of work on heterogenrous explosives, both experimentally and numerically, focusing on the effect of particles of different metal and sizes in different explosives. S. Menon *et.al.* at George Institue of Techology, USA, [36–42], have focued on model developement and simualtion of unconfined homogeneous and heterogeneous TNT (w/o Al) and NM (w/o inert iron, Fe, particles). Finally, some contribution have also been seen from ADD, Korea, [43–45], simulating confined afterburning of TNT/Al and also from France, by B. Khasainov and B. Veyssiere at Laboratoire de Combustion et Détonique, [46–48], who's early work focused on two-phase model development.

2.1 Homogeneous Afterburning

The bulk of the research on homogeneous afterburning has been carried out by A.L. Kuhl *et.al.*. In [5, 6] Kuhl *et.al.* explained that unconfined, homogeneous afterburning, can be divided in four stage as illustrated in Fig. 2.2.

Stage 1: Strong blast wave This stage occurs during t_1 and t_2 in Fig. 2.2. The outgoing blast wave heats up and accelerates the ambient air as it propagates through it. Meanwhile a rarefaction wave propagates inwards, initially boosting the acceleration caused by the blast wave, and later forcing an opposite directed acceleration of the detonation gases. The interface between the detonation products and shock compressed air is impulsively accelerated inducing RT instabilities, [1], to grow due to large density gradients across the contact surface as well as its impulsive acceleration. A short time after the initial blast the in-going rarefaction wave will overexpands the flow, [42], and thereby causes a second shock. Therefore a thin mixing layer is formed between the initial blast wave and the secondary shock.

Stage 2: Implosion The secondary shock will eventually strengthen by means of detonation gases accelerating it. Subsequently, the shock will strengthen to the point of implosion. The implosion further entrains the air into the mixing layer, enhancing the combustion, Fig. 2.2, t_3.

Stage 3: Reshock As Fig. 2.2, t_4, shows, when the secondary shock reflect from the origin it is set outwards and interacts with the existing RT instabilities. This mis-alaigns pressure and density gradients in the flow and in so doing deposits additional vorticity into the mixing layer. This is what gives rise to RM instabilities, [2], enhancing the turbulent mixing.

Stage 4: Asymptotic mixing: The primary and secondary shocks have now weaken sufficiently and what is left in the vicinity of the detonation centre is a 'constant-pressure' mixing layer, in which the remainder of fuel is consumed, Fig. 2.2, t_5.

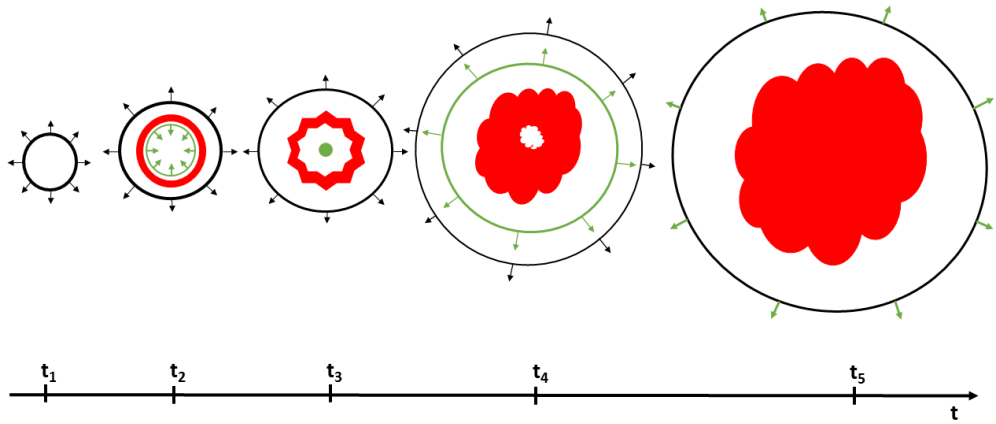

Figure 2.2: Schematics of a homogeneous explosion. Red: fireball, black: primary shock, green: secondary shock.

In this scenario, the general afterburning mechanism can be summarized as shown in Fig. 2.3.

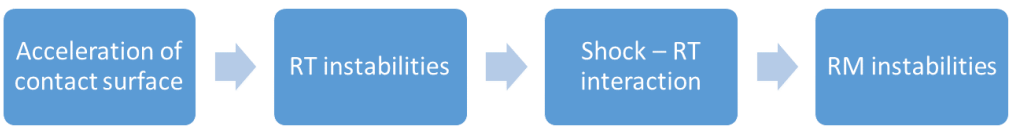

Figure 2.3: General mechanism of homogeneous afterburning.

These four stages of turbulent mixing, during which the afterburning (combustion) of the detonation product gases occurs, illustrate the main features that are necessary in a model aiming at describe and simulate the event. The majority of the turbulent mixing is done by the large scale turbulent dynamics. However, the energy that is released by the large mixing scales, due to combustion, is fed into the smaller dissipative scales by the turbulent energy cascade, [49]. These small scales are important for viscous and chemical kinetics that are responsible in releasing the chemical heat of combustion back to the mixing layer. Furthermore, capturing shock propagation is of key importance, since these waves will contribute to the large scale mixing generation.

Kuhl *et.al.* have in their work adopted the inviscid approach, arguing that since the processes are so fast that one can assume chemical time scales and gas viscosiuty and infinately small. During their work they applied 3D Adaptive Mesh Refinement (AMR) code, focusing on very fine computational resolution of these afterburning events and was able to study evolution of the mixing layer in [5], Fig. 2.4a and the effect of the turbulence of the afterburning in [20], Fig. 2.4b. Also Balakrishnan and Menon, [36, 37], have studied unconfined homogeneous afterburning, focusing on mixing layer dynamics, as illustrated by temperature contours in Fig. 2.4c.

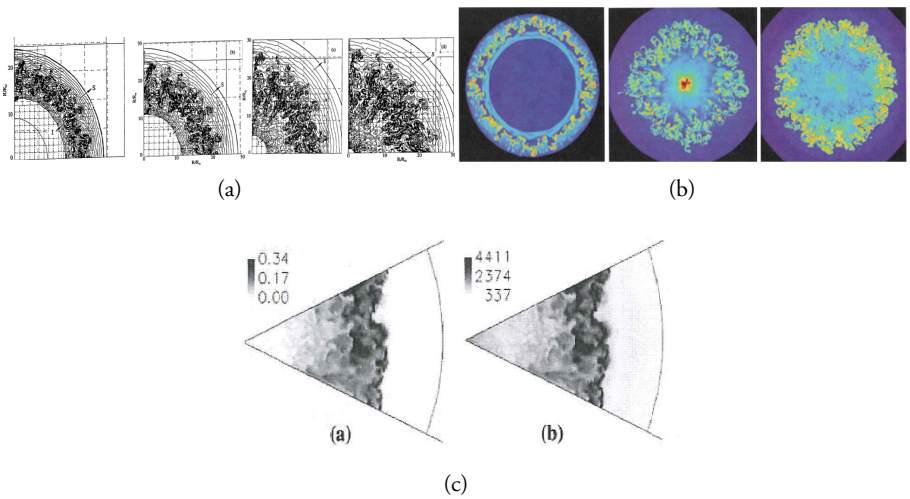

Figure 2.4: (a) Development of spherical mixing layer during implosion stage, [5], (b) spherical combustion cloud during a TNT explosion, featured in terms time series of temperature planes, [20], and (c) Countors of expothermicity in terms of CO_2 mass fraction and temperature from a TNT post-detonation afterburning, [37].

2.2 Heterogeneous Afterburning

When particles are included into the explosive charges, whether these are inert or reacting, the flow field, combustion, and thus the afterburning process becomes even more complicated. Amplification of impulse from an explosive charge is known to occur when solid metal particles are added to an explosive, due to the momentum and energy delivered by the particles. When such a charge is detonated, the high-pressure combustion products rapidly expand to drive a blast wave, which attenuates due to the effects of spreading, [39]. At the same time the metal particles pick up momentum from the gas due to drag, penetrate the contact surface and generate perturbations, which grow into RT instabilities that are essentially three-dimensional and give rise to enhanced mixing, compared to homogeneous

charge, of the hot detonation products and the shock-compressed air. If the initial charge contains reactive metal particles, the afterburn can provide a significant contribution to the total performance of the charge, [39]. Once the particle reach the ignition temperature, they start to burn and thereby react with the detonation products. These reactions can occur by two different mechanisms, i.e. *aerobic* that is oxidation by oxygen in the shock compressed air, if the explosive compound is oxygen deficient or *anaerobic*, that is by means of oxidation with oxidants in the detonation products (can occur in, among other applications, underwater detonations).

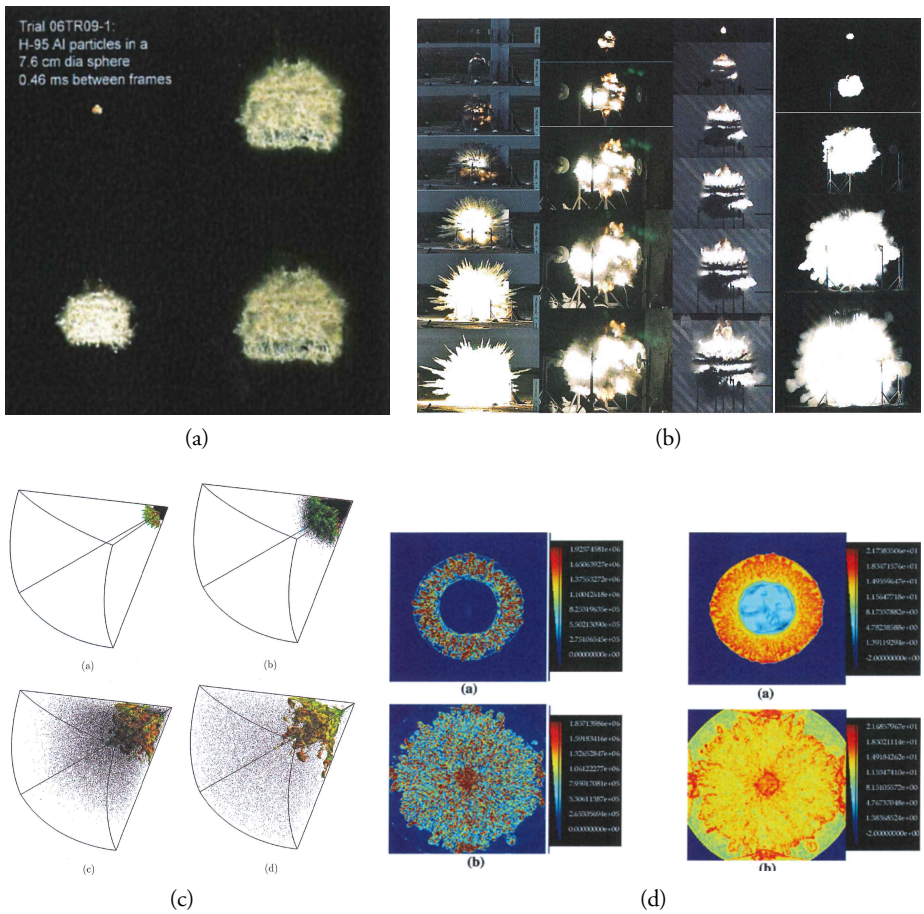

Figure 2.5: (a) Snap-shots from an experiment containg Al particles, 0.46 ms between frames, [30], (b) study in variation of aluminium particle combustion regimes by varying particle size and charge diameter, [23], (c) mixing layer evolution during afterburning of NM/Fe explosion, [42], and (d) explosively dispersed aluminium cloud combustion, featured in terms of vorticity (left) and baroclinique torque (right), [21].

Heterogeneous afterburning has been studied by many in recent year as this is of interest in both civilian and military applications. EBX and TBX charges have become 'standard' and it is required to know how these type of charges affect the infrastructure and the troops on the ground. Also, heterogeneous afterburing can occur during dust explosions and thus that can frequent in mining industries. Zhang and Frost *et.al.* have conduted much of the experimental and also numerical work in this field, studying both effect from inert particles of the blast and afterburning, [32], and reacting particles of different sizes and metals, [23], Fig. 2.5a and b. Moreover, Balakrishanan and Menon have investigated mixing layer dynamics and combustion durign NM/Fe and TNT/Al afterburning, [42], Fig. 2.5c. Finally, Kuhl *et.al.* have participated in this field as well, by simulating and experimentally studying afterburning from TNT/Al afterburning in unconfined and confined enviroment, [11,21], Fig. 2.5d.

Hence, to summarize the heterogeneous afterburning, Fig. 2.6 illustrates the schematics of this scenario. Basically, every feature of the homogeneous explosion (Fig. 2.2) becomes enhanced (that is why heterogeneous explosives are often called Enhanced Blast eXplosives). The shocks are stronger, the mixing layer is more perturbed by particles and the combustion is intensified.

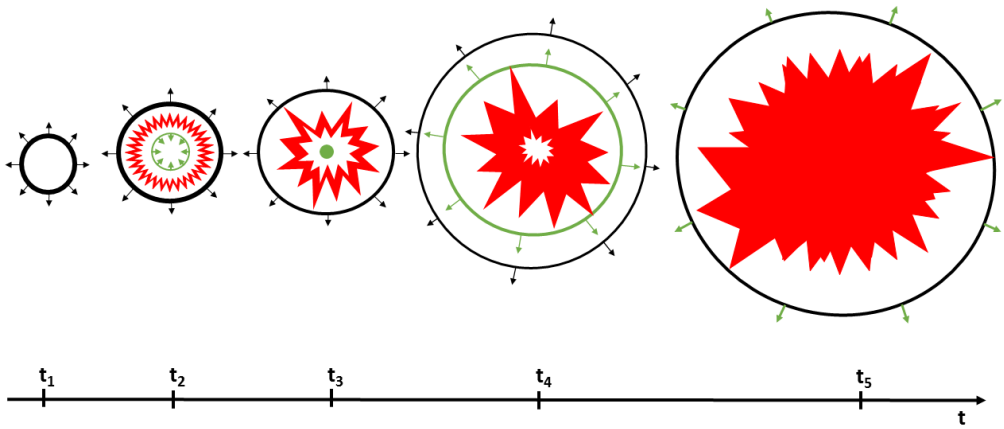

Figure 2.6: Schematics of heterogeneous explosion. Red: fireball, black: primary shock, green: secondary shock.

The main mechanism is the presence of particles, which enhance the blast loading, create perturbations on the contact surface between the detonation products and air, and generate RT instabilities faster and on larger variety of scales, Fig. 2.7.

Balakrishnan *et.al*, [36], and Ripley *et.al*, [25], found that the secondary shock is stronger when aluminium particles are added due to the increase in afterburn energy release and the decay rate of pressure is slower behind the primary shock. These features are found to be dependent on the particle concentration. The pressure decay is less and the second

Figure 2.7: General mechanism of heterogeneous afterburning.

shock is stronger with a high particle load.

In addition to the particle loading, the shape and size of the particles needs to be considered to get a desired performance, flakes and spherical particles have different effect on the detonation and combustion properties. Depending on the size of the particles, the boost in combustion can be at early times, (small particles - immediate heat release) or late (large particles, improved mixing), proper 'after'burn.

2.3 Near Surface Effects on Afterburning

Thus far, only unconfined afterburning scenarios have been discussed and one can imagine that the effect of full or partial confinement will affect the flow and combustion regardless of it being homogeneous or heterogeneous. The effect of complete confinement is threefold: (i) shock propagation pattern alters and (ii) volume expansion is inhibited and (iii) the access to oxidizer is limited, hence heterogeneous/anaerobic combustion is preferred. Kuhl *et.al.*, [11] and Kim *et.al.*, [44] have studied confined afterburning, due to the simplicity of replicating bomb calorimeter experiments and applications of interest in the dust explosions and tunnel systems. Common conclusions from these studies are that combustion is enhanced due to confinement and the impulse is enhanced due to combustion.

Complete confinement will not be featured in this work, but rather, semi-confinement, i.e. near surface explosion scenario. This semi-confined case has not been given much attention, with respect to the numerical simulations of mixing and afterburning in the vicinity of a surface and the effect HoB has on these properties.

As been showed by [24, 25, 50, 51], near-surface afterburning is very much affected by shock-mixing layer interaction. The features of afterburning are the same as for the scenarios above (instabilities, vorticity, mixing, combustion), but the first aforementioned depends much on the shock propagation pattern, which in turn is depended on HoB above ground. Figure 2.8 illustrates the general schematics of (a) shock propagation pattern and (b) the combustion zone evolution for a near surface explosion. As the primary shock expand, it impacts and reflects from the ground and travels back inwards, as two separate shocks (t_1 and t_2 in Fig. 2.8a). These shocks will pass through the thin mixing layer, depositing vorticity and instigating mixing (t_1 and t_2 in Fig. 2.8b). Thereafter, these shocks will merge, travelling outwards and also downwards again. Meanwhile, behind these reflected shocks, low pressure regions are created, entraining air into the mixing layer and giving the combustion region the well-known 'mushroom' shape (t_3 in Fig. 2.8a and b). The

shock system will grow more complex, extending into the Mach stems at the ground and propagating up and down through the mixing layer (t_4 and t_5 in Fig. 2.8a) extending the combustion region, as each passage generates more RM instabilities (t_3 in Fig. 2.8b). The shape of the 'mushroom' combustion region will depend on the shock passage patten, i.e. the HoB, (t_4 and t_5 in Fig. 2.8b).

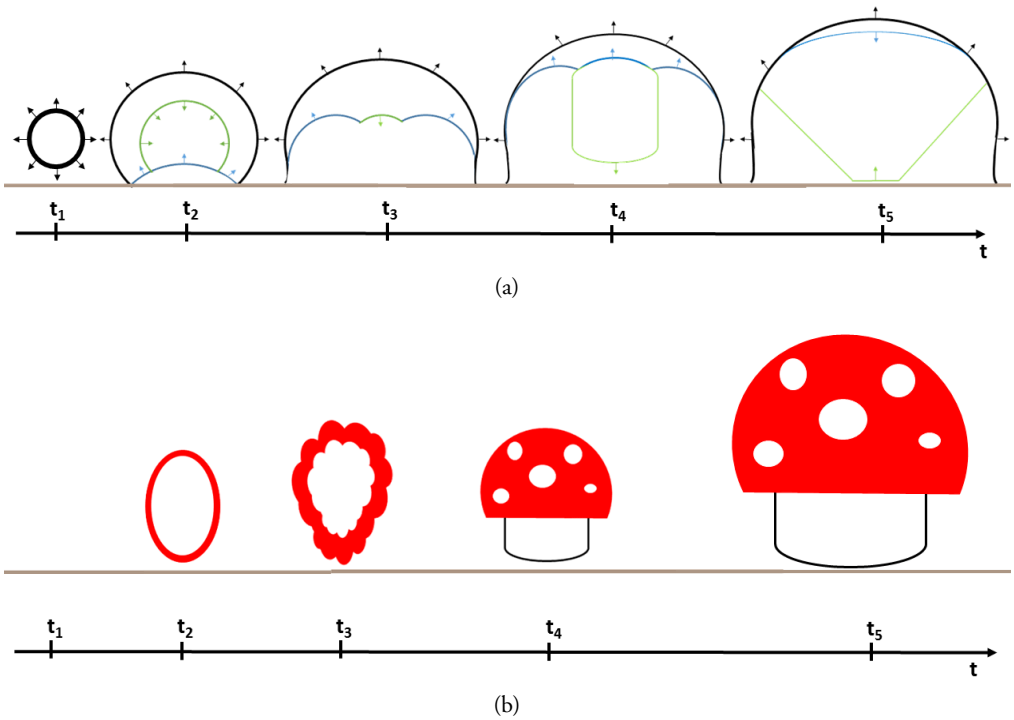

Figure 2.8: Schematics of near-surface afterburning. (a) shock propagation and (b) combustion zone evolution. Red: fireball, black: primary shock, green: secondary shock.

Hence, the general mechanism for the near-surface afterburning is summarized in Fig. 2.9.

Figure 2.9: General mechanism of near-surface afterburning.

Including reacting particles to a TNT charge and varying the HoB has not been shown to alter the major features of the afterburning processes, [52], i.e. the expansion of the primary shock and the ground reflections interacting with the mixing layer and the com-

bustion products. The enhanced blast effect is nevertheless present, as is the prolonged afterburning, with the presence of the particles contributing to enhanced mixing compared to homogeneous cases and aluminium reactions with air contributing to a more prolonged afterburning.

Ripley *et.al.*, [25] and Ritzel *et.al.*, [24], have studied near-surface phenomenology of the thermobaric explosion in Northen Lights trial series, [53]. In their work, they found that, as in confined simulations, mixing and heating caused by ground reflected shock promoted the afterburing and thereby also increased the blast pressure. Also, here the effect as slightly different depending on the particles size. They also found effect of the particle jetting for particles $> 50\mu$ m and hypothesized that these jets where what actually drove the primary blast wave and contributed to the enhanced blast, Fig. 2.10.

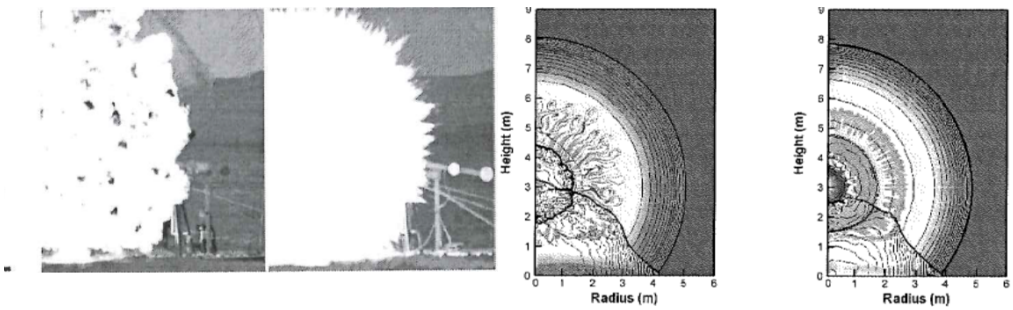

Figure 2.10: Left: C4 trial and IEF trails, right: flow field and temperature from CFD simulation of the same trails, [24, 53].

To be able to capture these jetting effect in particular, Ripley *et.al.*, [25], postulated that current CFD codes (Euler-Euler) had to be able to handle particle-particle interaction and also wishfully, the agglomeration effects.

Conclusively, to be able to simulate these three scenarios, the following features are wished to be captured by means of numerical modelling:

- shocks - requires spatial resolution and proper numerics;
- mixing and instabilities - puts demands on turbulence modelling;
- combustion - need to address turbulence chemistry interaction and chemical kinetics;
- heterogeneous afterburning - two-phase flow, particle combustion and particle-particle interaction need to be incorporated.

Thus, the next three chapters will describe how the list above was implemented.

Chapter 3

Gaseous Combustion and Modelling

3.1 Flame Physics

When dealing with afterburning it is natural to first discuss the flame physics and to account for the flame types that can occur. But prior to that it should be distinguished between the concepts of detonation and deflagration. Flame propagation of a *detonation* is caused by a pressure wave and the flame propagation is the sustained by exothermic chemical reactions (supersonic propagation), while a *deflagration* is flame propagation caused by exothermic chemical reactions and sustained by molecular transport (subsonic propagation). The post-detonation afterburning is, confusingly, a flame that burns as a deflagration but is initiated by a detonation (of an explosive charge).

In a deflagration regime, it is commonly distinguished between *laminar* flames, when the flame is propagating though/in a laminar flow and *turbulent* flames, when the flame is burning in turbulent flow, the flame can interact with turbulence and affect the flow scales, which in turn can greatly affect the fuel consumption and flame topology. As mixing is crucial part of afterburning, only turbulent cases will be considered here. There are two main types of turbulent flame and these are now briefly described.

3.1.1 Premixed Flame

Schematics for a turbulent premixed flame are illustrated in Fig. 3.1a. The fuel and oxidizer are homogeneously premixed and the flame propagates through this mixture with a speed s_u (one can distinguish between the laminar flame speed and a turbulent flame speed), leaving combustion products behind. The temperature rise occurs in the reaction zone between the combustion products and reactants. To characterise premixed flames, certain length, velocity and time scales can be defined. These are a laminar flame thickness, δ_u, that is a flame length scale; an integral length scale, ℓ_I, that is a representative flow length scale, reprsenting the scale of the most energetic eddies in the turbulence cascade, [49]; the laminar flame speed s_u; the velocity of the turbulent eddies, u', which is a representative

velocity of the eddies with the length scale ℓ_I; a turbulence time scale, τ_f, that represents the flow time scale; and the chemical time scale, τ_c, that represents the time scale for chemical reactions.

Several non-dimensional numbers can also be defined, such as the turbulent Damköhler number, $Da = \tau_f/\tau_c$, and the turbulent Reynolds number $Re_t = \ell_I u'/\nu$, with ν being the kinematic viscosity. Depending on these quantities, the turbulent premixed flames can be put into different combustion regimes according to Borghi or Williams diagrams, [54–56], e.g. such as in Fig. 3.1b, that easily illustrate which mechanisms are controlling the turbulent combustion and thus provide hints as to which modelling approach is appropriate for which case. For instance, for $Da > 1$ the turbulent time scale, τ_f, is larger than the chemical one, τ_c, and hence *reaction sheets* form, whereas for $Da < 1$ the turbulent scales rapidly mix reactants, which leads to *distributed reaction zones*. If both scales are of similar size, $Da \approx 1$, strong turbulence-chemistry interaction effects are expected.

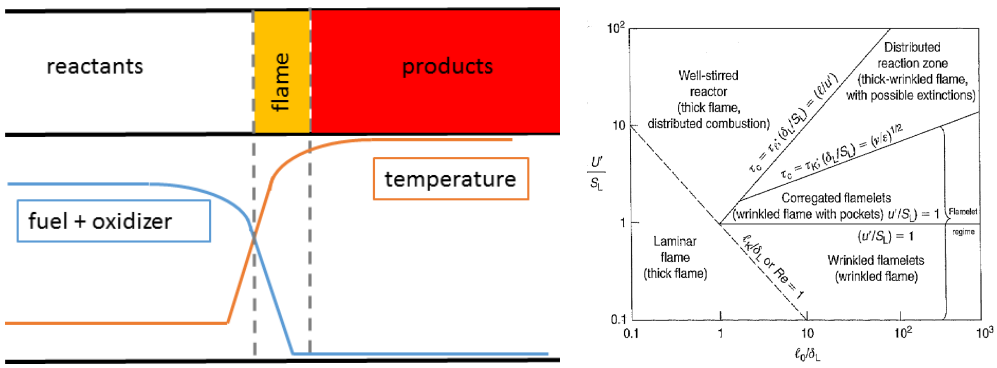

(a) (b)

Figure 3.1: (a) Schematics of a premixed flame and (b) an example of a Borghi diagram for premixed flames, [57].

3.1.2 Diffusion Flame

A diffusion flame is a non-premixed flame, in which the burn rate is determined by the rate at which fuel and oxidizer are brought together, or *diffused* to react with each other. A schematic picture of a diffusion flame is shown in Fig. 3.2a. The peak temperature is found in the reaction zone between the fuel and the oxidizer. In a turbulent diffusion flame the reactants are also affected by turbulent motion on their respective way to each other, and turbulence, as in the premixed case, can alter the reactant species diffusion speeds. It is also difficult to define flame scale to aid in flame classification as the τ_c is dependent on τ_f and τ_f is different depending on the case and the enviroment (strained/unstrained, steady/unsteady, etc.), [58], but some attempts are made, an example of which is shown in Fig. 3.2b. The diffusion flame are also more sensitive to mixing and flame streching,

as these can quench easibly when the turbulent motions become faster than the diffusion rate of reactants. Hence, different flame stabilization mechanisms are of importance for industrial diffusion flame, mechanisms such as triple flames, pilot flames, swirl-stablized flame and auto-ignition, [58], to mention a few.

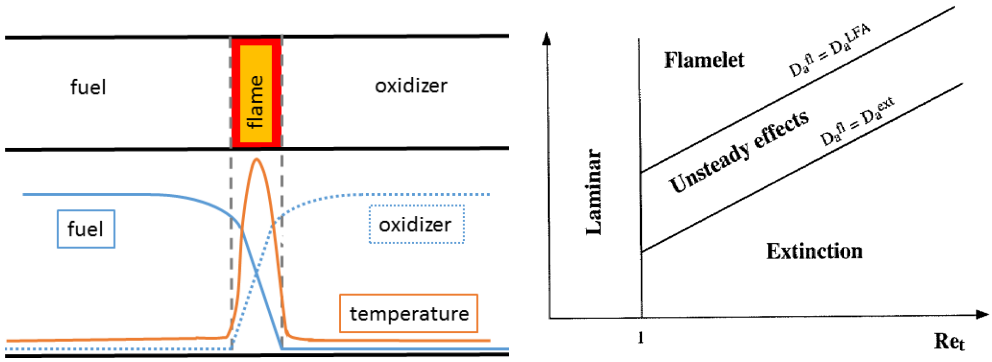

Figure 3.2: (a) Schematics of a diffusion flame and (b) an example of a non-premixed regiem diagram, [58].

3.1.3 'Post-detonation' Flame

The post-detonation afteburning flame is a turbulent diffusion flame, as the Fig. 3.3 shows. The figure shows fuel (carbon and aluminium), oxygen and temperature profiles taken along the centre radius and time-averaged over five time instances to schematically demonstrate the nature of this type of flame. Fig. 3.3 shows the flame profiles very similar to Fig. 3.2a with some variations due to HoB and also more fluctuated profiles for cases with aluminium.

A post-detonation afterburning flame is a bit different compared to traditional industrial diffusion flames. The high temperature region is present through the mixing layer due to post-detonation enviroment, the fuel and oxidizer are brought together not only by molecular diffusion but also by means of vorticity generated by the hydrodynmic instabilities. Compared to the common diffusion flames, the 'risk' of quenching here is low, as the whole combustion region does contain high temperature and the combustion is stabilized by auto-ignition, as the hot fuel is mixing with oxygen in the mixing layer. As long there is fuel, a post-detonation flame will burn and with auto-ignition occurring, the chemical kinetics are becoming important.

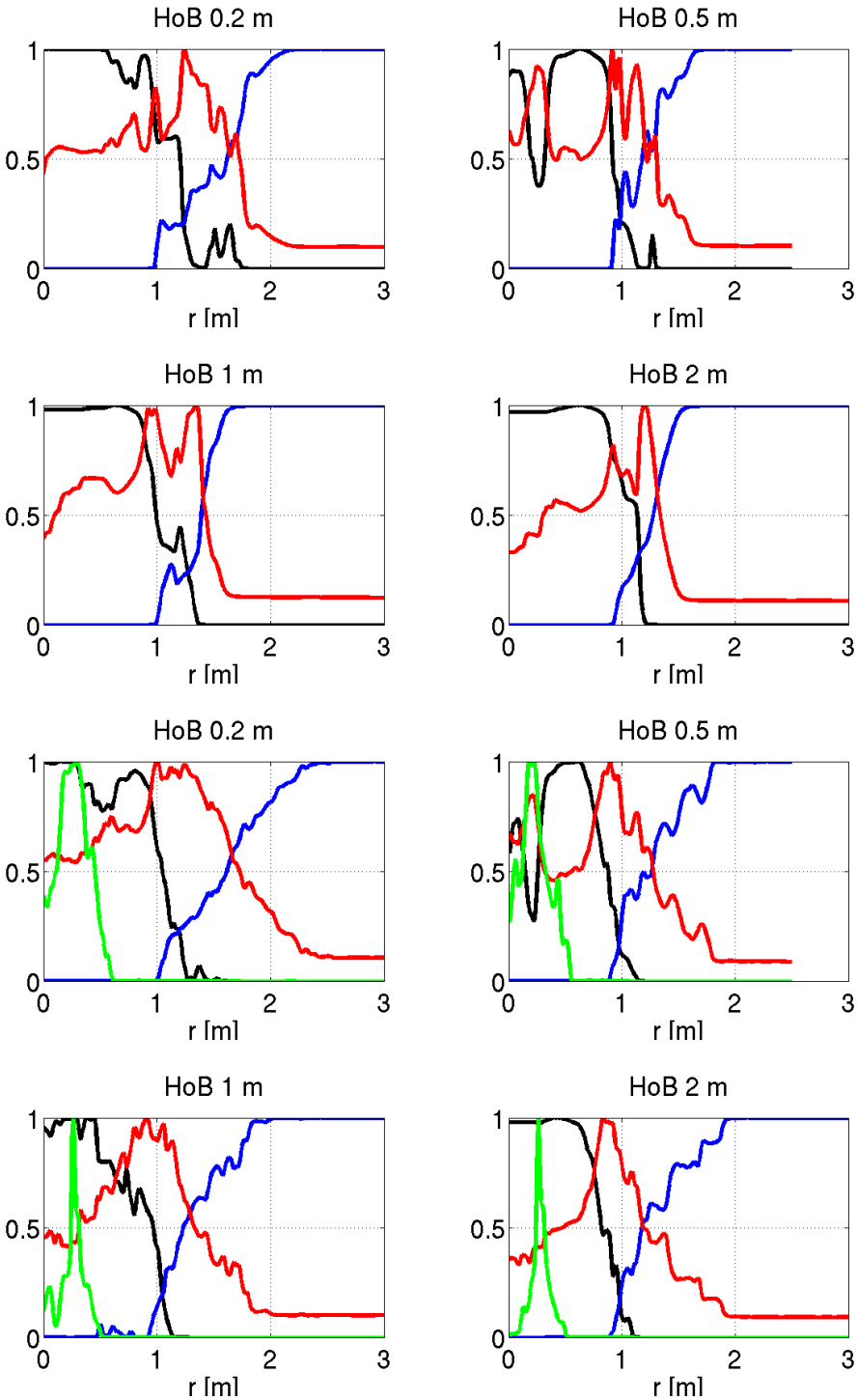

Figure 3.3: Legend: (–) $< \mathrm{C} >$,(–) $< \mathrm{O}_2 >$,(–) $< T >$,(–) $< \mathrm{Al} >$,

3.2 Combustion Modelling

The governing equations for a two-phase reacting flow consist of balance equations for mass, momentum, energy and species mass fraction. These equations, closed by equations of state (thermal and caloric) and constitutive equations form, the Navier-Stokes equations,

$$\begin{cases} \partial_t(\rho) + \nabla \cdot (\rho \mathbf{u}) = S_p, \\ \partial_t(\rho \mathbf{u}) + \nabla \cdot (\rho \mathbf{u} \otimes \mathbf{u}) = -\nabla p + \nabla \cdot \Big((\beta - \frac{2}{3}\mu) \nabla \cdot \mathbf{u}\mathbf{I} + 2\mu \mathbf{D} \Big) + \mathbf{F_p} \\ \partial_t(\rho h) + \nabla \cdot (\rho h \mathbf{u}) = -\dot{p} + \Big((\beta - \frac{2}{3}\mu) \nabla \cdot \mathbf{u}\mathbf{I} + 2\mu \mathbf{D} \Big) \cdot \mathbf{u} + \nabla \cdot \Big(\kappa \nabla T \Big) + H_p, \\ \partial_t(\rho Y_i) + \nabla \cdot (\rho \mathbf{u} Y_i) = \nabla \cdot \frac{\mu}{Sc_i} \nabla Y_i + \dot{w}_i. \end{cases} \tag{3.1}$$

Here ρ is the density, $\mathbf{u}$ the velocity, p the pressure, T the temperature, β the bulk viscosity, μ the dynamic viscosity, $\mathbf{I}$ the unity tensor and $\mathbf{D}$ is the symmetric part of the velocity gradient, $\nabla \mathbf{u}$. The energy is expressed in the form of h, the enthalpy, and $\dot{w}_i$ is the reaction rate, Y_i the mass fraction of species i. S_p, $\mathbf{F_p}$ and H_p are source terms from particle–fluid interaction and are described further in Chapter 4.

3.2.1 Equations of State

The thermal and caloric Equations of State (EoS) describe the intrinsic relations between the state variables (e.g. pressure, density and temperature) and the energy, enthalpy in this case, in the fluid mixture.

Caloric EoS

The caloric EoS states the relation between the energy and specific heats. In this work the following EoS is adopted,

$$h = \sum_i^N (Y_i h_{f,i}^\theta) + \sum_i^N \Big(Y_i \int_{T_0}^T c_{p,i}(T) \mathrm{d}T \Big), \tag{3.2}$$

in which $h_{f,i}^\theta$ is the enthalpy of formation at standard temperature and pressure for the species i, $c_{p,i}$ the specific heat at constant pressure for species i and T_0 the ambient temperature of the surroundings. Here, the specific heats are assumed to be linear functions of T, resulting in that $c_{p,i}(T) = A + BT$, where A and B are species–specific constants.

Thermal EoS

the thermal EoS describes the relation between pressure, density and temperature and is most often species dependent. There are several thermal EoS's that are commonly used in detonation and post-detonation flow applications, the three most common being the ideal

gas law, Noble–Abel EoS and Jones–Wilkins–Lee (JWL) EoS. The ideal gas law, which was used in papers I and II, is expressed as

$$p = \rho R_0 \sum_i (Y_i/M_i)T, \tag{3.3}$$

where M_i is the molar masses of species i and R_0 the universal gas constant.

The Nobel–Abel EoS, following [44, 59], is expressed as

$$p = \frac{\rho R_0 \sum_i (Y_i/M_i)T}{(1 - An)}, \tag{3.4}$$

in which A is an empirical constant that accounts for the co–volume where reactions take place and n is the number of moles per unit volume. Noble-Abel EoS has been used in simulations for papers III-V, with $A = 8.9 \cdot 10^{-6}$ $\mathrm{m}^3/\mathrm{mol}$.

Finally, the JWL–EoS, [60, 61] is expressed as:

$$p = A_{jwl}\Big(1 - \frac{\omega}{R_1\sigma}\Big)\exp\left(-R_1\sigma\right) - B_{jwl}\Big(1 - \frac{\omega}{R_2\sigma}\Big)\exp\left(-R_2\sigma\right) + \omega\rho c_v T. \tag{3.5}$$

Here, A_{jwl}, B_{jwl}, R_1, R_2 and ω are explosive compound specific constants, $\sigma = \rho_{TNT}/\rho$, where ρ_{TNT} is the density of TNT and $c_v = c_p - R_0 \sum_i (Y_i/M_i)$ is the specific heat capacity at constant volume. This EoS is mostly used in early detonation events, as the expression in Eq. 3.5 becomes the ideal gas law at 'normal' pressures.

3.2.2 Constitutive Equations

The constitutive equations describe the response of the fluid mixture to external forces and in most flow situations the fluid mixture can be assumed to be a Newtonian fluid with Fourier heat conduction and Fickian diffusion. Throughout this work, following [62], it is assumed just that, i.e. that the gas mixture is linearly viscous, with Fourier heat conduction and Fickian diffusion. The viscosity, μ, is modelled by Sutherland's law, the species and thermal diffusivities are modelled as $D_i = \rho\nu/Sc_i$ and $\kappa = \mu/Pr$, respectively, where Sc_i is the Schmidt number of species i and Pr is the Prandtl number.

3.2.3 Modelling Approaches

With the governing equations properly closed, the choice of the modelling approach must be made. The choice is between Direct Numerical Simulation (DNS), on one end of the modelling spectra, in which all spatial and temporal scales are resolved, [49], but which is currently limited by the required computational effort to canonical problems; the Reynolds Averaged Navier-Stokes (RANS) models, on the other end of the modelling spectra, which are based on ensemble-averaged or time-averaged Eq. 3.1, meaning that all of the unsteadiness of the turbulence has to be modelled, and finally Large Eddy Simulation (LES), which

is a compromise between DNS and RANS. In the LES approach, the scales of the flow are separated into large-scale, energetic eddies (scales of ℓ_I and τ_f) that are transiently resolved on the grid and the small, low energy scales, the effect of which on the flow needs to be modelled by subgrid terms. Hence, for post-detonation afterburning, where the interest lies in the dynamic processes of shock propagation, mixing and combustion, the LES approach is chosen for its ability to provide time accurate solutions, as opposed to RANS, and at affordable cost, compared to DNS.

3.3 Large Eddy Simulation

The LES approach, [63], that is adopted throughout this work, is based on low-pass filtering the the governing equations, Eq. 3.1; this removes the influence of the smallest scales, the effects of which are separately modelled using subgrid models. The dependent variables are decomposed as $f = \tilde{f} + f''$, where $\tilde{f}$ is the resolved part, commonly expressed using a Favré filter such that, $\tilde{f} = \overline{\rho f}/\bar{\rho}$, and a fluctuating part, f'', the effects of which are modelled by the subgrid models. The filtering is applied to the resolved part through $\bar{f} = G * f$ with $G = G(\mathbf{x}, \Delta)$ being the filter with the filter width Δ. The filter G must satisfy $\int_{CV} G(\mathbf{x}, \Delta)\mathrm{d}^3\mathbf{x} = 1$ having compact support in the computational domain, CV. Filtering the Navier-Stokes equation, Eq. 3.1, results in the reactive LES equations as follows,

$$\begin{cases} \partial_t(\bar{\rho}) + \nabla \cdot (\bar{\rho}\tilde{\mathbf{u}}) = S_p, \\ \partial_t(\bar{\rho}\tilde{\mathbf{u}}) + \nabla \cdot (\bar{\rho}\tilde{\mathbf{u}} \otimes \tilde{\mathbf{u}}) = -\nabla\bar{p} + \nabla \cdot \left(\bar{\mathbf{S}} - \mathbf{B}\right) + \mathbf{F_p} \\ \partial_t(\bar{\rho}\tilde{h}) + \nabla \cdot (\bar{\rho}\tilde{h}\tilde{\mathbf{u}}) = -\dot{\bar{p}} + \tilde{\mathbf{S}} \cdot \nabla\tilde{\mathbf{u}} + \nabla \cdot \left(\kappa\nabla\tilde{T} - \mathbf{b}_h\right) + H_p, \\ \partial_t(\bar{\rho}\tilde{Y_i}) + \nabla \cdot (\bar{\rho}\tilde{\mathbf{u}}\tilde{Y_i}) = \nabla \cdot \left(\frac{\mu}{Sc_i}\nabla\tilde{Y_i} - \mathbf{b}_i\right) + \overline{\dot{w}}_i, \end{cases} \tag{3.6}$$

in which $\bar{}$ and $\tilde{}$ denote filtered and Favre filtered quantities, respectively. $\bar{\mathbf{S}} = \left((\beta - \frac{2}{3}\mu)\nabla \cdot \tilde{\mathbf{u}}\mathbf{I} + 2\mu\tilde{\mathbf{D}}\right)$ is the viscous stress tensor, and the subgrid (unresolved) stress and flux terms are $\mathbf{B} = \bar{\rho}(\widetilde{\mathbf{u} \otimes \mathbf{u}} - \tilde{\mathbf{u}} \otimes \tilde{\mathbf{u}})$, $\mathbf{b}_i = \bar{\rho}(\widetilde{\mathbf{u}Y_i} - \tilde{\mathbf{u}}\tilde{Y_i})$ and $\mathbf{b}_h = \bar{\rho}(\widetilde{\mathbf{u}h} - \tilde{\mathbf{u}}\tilde{h})$, [64].

3.3.1 Subgrid Modelling

To close the filtered reacting LES equations, Eq. 3.6, a subgrid model is required to describe the effects of the unresolved flow on the resolved flow, using the resolved variables, [63]. In LES, subgrid models can be characterized as either structural or functional, [63]. *Structural subgrid models* attempt to describe the structure of the subgrid stress tensor and flux vectors. An expample of such model is the so-called Mixed Model, [65], that combines the scale similarity model with an eddy viscosity model. *Functional subgrid models*, on the other hand, aim at describing the effect and not the structure of the subgrid stress and flux terms, that is to say these models attempt to mimic the kinetic energy cascade from the

large energetic scales to small dissipative scales. Examples of functional models include the Smagorinsky model, [66] and the One Equation Eddy Viscosity Model, [67]. Another functional model, which is employed in this work, papers I and II, is the Hyperviscosity subgrid model.

Hyperviscosity Model

Most subgrid models are designed for low Mach number flows and therefore usually fail when strong shocks are present. Around shocks the dilatation, $\nabla\tilde{\mathbf{u}}$, is significant. In order to extend the use of the subgrid viscosity models to high Mach number flows and flows with shocks, Cook & Cabot, [68], developed a subgrid viscosity model for shock-turbulence interactions. This model is based on the shock-capturing artificial viscosity approach of von Neumann & Richtmyer, [69], and the Smagorisky subgid model, [66], which, coincidentally, was developed based on the work of von Neumann & Richtmyer. More specifically, the subgrid stress and flux-vector terms are modelled as,

$$\mathbf{B} \approx -\beta_k \nabla\tilde{\mathbf{u}} - 2\bar{\rho}\mu_k\widetilde{\mathbf{D}}, \quad \mathbf{b_h} \approx \bar{\rho}(\tfrac{\mu_k}{Pr})\nabla\tilde{h}, \quad \mathbf{b_i} \approx \bar{\rho}(\tfrac{\mu_k}{Sc_{t,i}})\nabla\tilde{Y}_i, \tag{3.7}$$

in which μ_k and β_k are the subgrid viscosity and subgrid bulk viscosity to be modelled. Following Cook & Cabot, [68], we here adopt the subgrid viscosity and subgrid bulk viscosity models,

$$\mu_k = C_\mu^r \rho \Delta^{(r+2)} \overline{|\nabla^r \mathbf{D}|} \quad \text{and} \quad \beta_k = C_\beta^r \rho \Delta^{(r+2)} \overline{|\nabla^r \mathbf{D}|} \tag{3.8}$$

in which the overbar denotes a truncated Gaussian filter function. Inclusion of the bulk viscosity term is the key to capturing shocks without destroying vorticity, i.e., β_k can be made large, to smooth shocks, without impacting small–scale turbulence in regions where $\nabla\tilde{\mathbf{u}} \approx 0$. Additionally, by setting $r > 0$, the viscosity keys directly on the ringing, rather than indirectly on gradients. This eliminates the need for ad-hoc limiters and switches to turn off β_k in special cases, e.g. expansion and isentropic compression, [70]. It also removes the need for a dynamic procedure [71] to turn off μ_k in regions of uniform shear. For the simulations reported in papers I and II, $r = 2$, $C_\mu^r = 0.05$ and $C_\beta^r = 0.1$.

Implicit Large Eddy Simulation Model

Papers III-V employ the Implicit LES model, another subgrid modelling approach and an alternative to conventional LES, [72–74]. The primary reason for the development of ILES was the absence of a universal theory of turbulence, the pragmatic and empirically-based development of subgrid models and the fact that the leading-order truncation error of the numerical methods used to solve the LES equations often interact with the subgrid flow model. More specifically, ILES are based on the original (unfiltered) flow equations instead of the filtered ones and invoke non-oscillatory constraints via non-linear limiters in finite volume formulations to implicitly act as a filtering (and nonlinear adaptive regularization) mechanism for the small scales. Using Modified Equations Analysis (MEA) Grinstein &

Fureby, [75], were able to derive expressions for the implicit (or build-in) subgrid models in a finite volume framework utilizing a hybrid flux formulation. More specifically, for the reacting flow equations (Eq. 3.6) the implicit (built-in) subgrid models are

$$\begin{aligned}
\mathbf{B} &= \bar{\rho}\Big(C(\nabla\tilde{\mathbf{u}})^{\mathrm{T}} + (\nabla\tilde{\mathbf{u}})C^{\mathrm{T}} + \chi^2(\nabla\tilde{\mathbf{u}})\mathbf{d}\cdot(\nabla\tilde{\mathbf{u}})\mathbf{d}\Big) + \mathrm{h.o.t},\\
\mathbf{b}_h &= \bar{\rho}\Big(C(\nabla\tilde{h}) + \chi^2(\nabla\tilde{h}\cdot\mathbf{d})(\nabla\tilde{\mathbf{u}})\mathbf{d} + \mathrm{h.o.t},\\
\mathbf{b}_i &= \bar{\rho}\Big(C(\nabla\tilde{Y}_i) + \chi^2(\nabla\tilde{Y}_i\cdot\mathbf{d})(\nabla\tilde{\mathbf{u}})\mathbf{d}\Big) + \mathrm{h.o.t},
\end{aligned} \tag{3.9}$$

in which $C = \chi(\tilde{\mathbf{u}}\cdot\mathbf{d})$, χ a non-linear function of the flux limiter, Γ, used to switch between the underlying high-order and low-order numerical flux reconstruction schemes and $\mathbf{d}$ vector between two neighbouring cells. These implicit subgrid models are of the same mathematical character as the subgrid viscosity models, but with the subgrid viscosity being a fourth-rank tensor instead of a scalar. This allows these models to better handle simultaneous flow and grid anisotropies and non-uniformities, but make them dependent of the selection of flux limiters with monotonicity preserving flux limiters were found to perform the best, [76].

3.3.2 Turbulence Chemistry Interaction

Besides the subgrid flow modelling, combustion modelling entailing the ability to model the turbulent reaction front is the other challenge for combustion LES. Two main classes of LES combustion models can be distinguished: flamelet models and finite rate chemistry models, both containing sub-classes and many different models. *Flamelet models* assume that the flame is thin compared to the length scales of the flow ($\sim \ell_I$), and the flame behaves like an interface between fuel and oxidizer (in non-premixed combustion), or between reactants and products (in premixed combustion). The flow and chemistry are usually decoupled, and the chemistry is represented by one-dimensional laminar flame, combined in a flamelet library, which is modified by the turbulence in a separate step, before the equations for the flame propagations are solved. *Finite rate chemistry models* assume nothing about the flow or flame but attempt to solve the species equations using models for the low-pass filtered reaction rates. Many different finite rate chemistry models are available including thickened flame models, [77], scale separation combustion models, eg. Eddy Dissipation Concept (EDC), [78] and Parially Stirred Reactor (PaSR) models, [79, 80], presumed and transported probability density function models, [81], and [82], respectively, all with their own advantages and disadvantages.

Throughout this work the Partially Stirred Reactor models is used, which is a type of scale separation model. The reason for choosing this model is that is has proven to give good predictions of turbuelnce chemistry interations in a wide variety of applications, [83–86].

Partially Stirred Reaction Model

The Partially Stirred Reactor (PaSR) model, [80], as any scale separation models, is based on the assumption that combustion takes place in fine-structure regions $(*)$ characterized by intense chemical activity and vorticity, embedded in regions of lower levels of vorticity and chemical activity, the surrounding, $(^0)$. Since most of the mixing occurs in the fine structures, the reactions also take place there as the reactants are mixed at scales down to the molecular scales. The fine structures topologically form complex regions, composed of a muddle of interacting tube–, ribbon– and sheet–like structures [87], in which most of the dissipation and mixing takes place. The conditions in the fine structures and surroundings are related by the subgrid balance equations of mass and energy

$$\begin{cases} \rho\Big(Y_i^* - Y_i^0\Big)/\tau^* \approx \dot{w}_i(\rho Y_i^* T^*), \\ \rho\sum_{i=1}^N \Big(Y_i^* h_i^* - Y_i^0 h_i^0\Big)/\tau^* \approx \sum_{i=1}^N h_{i,f}^\theta \dot{w}_i(\rho Y_i^* T^*), \end{cases} \tag{3.10}$$

in which τ^* is the subgrid time. By introducing the reacting volume fraction, γ^*, as the ratio of the volume of the fine structures to the LES cell volume, and thereby expressing the species mass fraction and temperature as $\tilde{Y}_i = \gamma^* Y_i^* + (1-\gamma^*)Y_i^0$ and $\tilde{T} = \gamma^* T^* + (1-\gamma^*)T^0$, respectively, these balance equations may be reformulated as

$$\begin{cases} \rho\Big(Y_i^* - \tilde{Y}_i\Big) = (1-\gamma^*)\tau^* \dot{w}_i(\rho Y_i^* T^*), \\ \rho\sum_{i=1}^N \Big(Y_i^* h_i^*(T^*) - \tilde{Y}_i \tilde{h}_i(\tilde{T})\Big) = (1-\gamma^*)\tau^* \sum_{i=1}^N h_{i,f}^\theta \dot{w}_i(\rho Y_i^* T^*). \end{cases} \tag{3.11}$$

The reacting volume fraction is defined as $\gamma^* = \Delta V^*/\Delta^3$, in which Δ^3 is the cell volume, in which the LES variables are constant. This implies that it is possible to lump the fine structure and surrounding fluid components together in different parts of the LES cell. The lumped fine structures are collectively described by the chemical time scale, τ_c, as the reactions are assumed to take place within these structures. Since the dependent variables are constant in each LES cell, the fine structure volume can be approximated as $\Delta V^* = \Delta^2|\tilde{\mathbf{u}}|\tau_c$. Similarly, the cell volume can be estimated as $\Delta^3 = \Delta^2|\tilde{\mathbf{u}}|(\tau_c + \tau^*)$. The definition of the reacting volume fraction the results in,

$$\gamma^* = \tau_c/(\tau_c + \tau^*). \tag{3.12}$$

In Eq. 3.12 the chemical time scale must be representative of the overall combustion reaction, and is here represented by $\tau_c \approx \delta_u/s_u \approx \nu/s_u^2$. The modelling of the fine structure residence time, τ^*, is based on the observation that the fine structure area to volume ratio, $\Delta S^*/\Delta V^*$, is defined by the dissipative length scale $l_D = (\nu\Delta/v')^{1/2}$, determined by the molecular viscosity, ν, and the subgrid velocity stretch v'/Δ, and that the velocity influencing these structures is the Kolmogorov velocity, v_K, such that $\tau^* = l_D/v_K$. Combining the expression for l_D and v_K, utilizing the Kolmogorov length and time scales,

$l_K = (\nu^3/\epsilon)^{1/4}$ and $\tau_K = (\nu/\epsilon)^{1/2}$, in which $\epsilon = (v')^3/\Delta$ is the dissipation, finally yields in the fine structure residence time being modelled as a geometrical mean of the Kolmogorov time scale and the shear time, τ_Δ,

$$\tau^* = \sqrt{\tau_\Delta \tau_K} = \nu^{1/4}\Delta^{3/4}v'^{-5/4} \tag{3.13}$$

in which $\tau_\Delta = \Delta/v'$. This shear time scale was recently found by [88] to accurately model the statistics of dissipation, and therefore also of small–scale mixing, which, in turn, is essential to the onset of chemical reactions. The values of γ^* in the afterburning regions vary typically between 0.1 to 0.3.

The filtered reaction rates can thus be expressed as

$$\overline{\dot{w}_i(\rho, Y_i, T)} = \gamma^* \dot{w}_i(\rho, Y_i^*, T^*) + (1-\gamma^*)\dot{w}_i(\rho, Y_i^0, T^0) \tag{3.14}$$

where the last term on R.H.S is very small and is usually neglected, so that the resulting filtered balance equation for species i can be approximated as,

$$\partial_t(\bar{\rho}\tilde{Y_i}) + \nabla\cdot(\bar{\rho}\tilde{\mathbf{u}}\tilde{Y_i}) = \nabla\cdot(D_i\nabla\tilde{Y_i} - \mathbf{b}_i) + \gamma^*\dot{w}_i(\rho, Y_i^*, T^*). \tag{3.15}$$

3.4 Numerical Methods

The LES equations are solved using a fully explicit finite volume scheme, based on the C++ library OpenFOAM, [4], as the computational platform. The code employs an unstructured collocated Finite Volume (FV) method [76], in which the discretization is based on Gauss's theorem together with an explicit time integration scheme. Given the vector of unknown variables, $\bar{\mathbf{v}} = \left(\bar{\rho}, \bar{\rho}\tilde{\mathbf{u}}, \bar{\rho}\tilde{h}, \bar{\rho}\tilde{Y_i}\right)^T$, the semi–discretized equations are

$$\partial_t(\bar{\mathbf{v}}) + \frac{1}{\delta V}\sum_f \left(\mathbf{F}_f^C(\bar{\mathbf{v}}) - \mathbf{F}_f^D(\bar{\mathbf{v}}) + \mathbf{F}_f^B(\bar{\mathbf{v}})\right) = s(\bar{\mathbf{v}}), \tag{3.16}$$

where $\mathbf{F}_f^C(\bar{\mathbf{v}})$, $\mathbf{F}_f^D(\bar{\mathbf{v}})$, $\mathbf{F}_f^B(\bar{\mathbf{v}})$ and $s(\bar{\mathbf{v}})$ are the convective, diffusive, subgrid fluxes and the source terms, respectively. The flux–reconstruction scheme for the convective fluxes, $\mathbf{F}_f^C(\bar{\mathbf{v}})$, is based on hybridizing a high–order linear–reconstruction algorithm, $\mathbf{F}_f^{C,H}(\bar{\mathbf{v}})$, with a low–order upwind–biased reconstruction algorithm, $\mathbf{F}_f^{C,L}(\bar{\mathbf{v}})$, using a non–linear van Leer flux limiter [89, 90], resulting in a TVD convection scheme. To minimize the non–orthogonality errors in the viscous and subgrid fluxes, $\mathbf{F}_f^D(\bar{\mathbf{v}})$ and $\mathbf{F}_f^B(\bar{\mathbf{v}})$, respectively, these are split into orthogonal and non–orthogonal parts. Central difference approximations are applied to the orthogonal part whilst face interpolation of the gradients of the variables is used for the non–orthogonal parts. The time–integration is performed

by a second order accurate TVD Runge–Kutta scheme [91], such that

$$\bar{\mathbf{v}}^{*} = \bar{\mathbf{v}}^{n} - \Delta t\Big(\frac{1}{\delta V}\sum_{f}\Big(\mathbf{F}_{f}^{C}(\bar{\mathbf{v}}^{n}) - \mathbf{F}_{f}^{D}(\bar{\mathbf{v}}^{n}) + \mathbf{F}_{f}^{B}(\bar{\mathbf{v}}^{n})\Big) - s(\bar{\mathbf{v}}^{n})\Big)$$

$$\begin{aligned}\bar{\mathbf{v}}^{n+1} &= \frac{1}{2}(\bar{\mathbf{v}}^{n} + \bar{\mathbf{v}}^{*}) \\ &\quad - \frac{1}{2}\Delta t\Big(\frac{1}{\delta V}\sum_{f}\Big(\mathbf{F}_{f}^{C}(\bar{\mathbf{v}}^{*}) - \mathbf{F}_{f}^{D}(\bar{\mathbf{v}}^{*}) + \mathbf{F}_{f}^{B}(\bar{\mathbf{v}}^{*}\Big) - s(\bar{\mathbf{v}}^{*})\Big).\end{aligned}$$

Chapter 4

Solid Phase Combustion and Modelling

When aiming to model metal particle combustion, it is preferred to know which are the primary mechanisms that govern the combustion and thus need be accounted for in the model. Depending on the volatile properties of metal, metal particle combustion can occur in two different ways. *Heterogeneous combustion* occurs on the particle surface, by means of surface oxidation reactions. This is true for non-volatile metals. *Homogeneous combustion* occurs in the gas phase, this is true for volatile metals that easily vaporize.

Depending on these two mechanisms, if the time scales for mass and energy transport during combustion are considered, the metal particle combustion is the be classified as either *kinetically controlled*, that is when the (surface) reaction rate is slower than the transport of the reaction products away from the surface. The combustion usually occurs through surface reactions, with quite uniform profile of fuel and oxidizer around the particle, as is illustrated in Fig. 4.1a. Or, *diffusionally controlled*, when the surface reactions are fast, compared to diffusion rates away from the surface, which create spatial gradients in gaseous fuel and oxidizer quantities as well as in temperature, as in Figs. 4.1b where the gas flame surrounds the particle and in Figs. 4.1c, as a detached diffusion flame.

In which regime the metal combustion occurs can depend (and change between regimes) on the size of the particle, the pressure and the oxidizer(s). It is not uncommon that a particle may experience both diffusion and kinetically controlled regimes during its lifetime, [92]. However, for aluminium combustion, with particles of mid-micron size, the Al-oxygen (and CO_2, H_2O) combustion, will take form of a detached diffusion flame, [92,93].

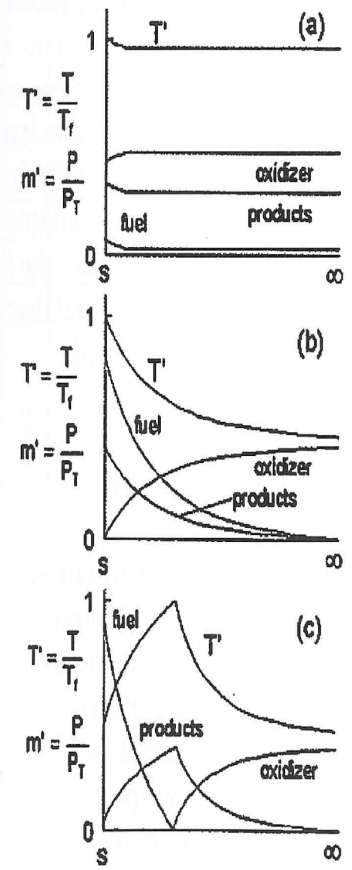

Figure 4.1: Metal particle burning regimes: (a) kinetically controlled, (b) diffusion controlled, without enveloped flame and (c) diffusion controlled, with enveloped flame, [92].

4.1 Aluminium Flame

When an aluminium (Al) particle is burning, the combustion process that converts the solid Al into the gaseous combustion products is more complex than what is modelled in this work. Figure 4.2 shows a schematic overview of an Al particle combustion, as a detached diffusion flame. This combustion process is basically threefold, [93].

1. **Melting and oxidation**
   When the temperature of the surrounding gas starts to reach the melting temperature of Al the solid Al melts into liquid Al, which at the boiling point temperature (T = 2971 K) undergoes phase change into the gaseous Al. When the gaseous Al is present, it oxidises with surrounding gas forming Al sub–oxides, e.g. AlO, AlO_2.

2. **Condensation**
   Aluminium sub–oxides condense to a liquid aluminium oxide, Al_2O_3. This condensation plays a major role in Al combustion and is the source of considerable amount of heat release during combustion. The condensed aluminium oxide can also deposit back on the particle surface and form an oxide cap, which in its turn changes the Al gasification rate since the cap blocks the vaporization from the region it covers, due to the fact that Al_2O_3 has a higher boiling temperature than solid Al. This in turn alters the temperature and other quantities around the particle.

3. **Dissociation**
   In the flame zone the heat is sufficient to dissociate the liquid Al_2O_3 back to gaseous aluminium sub–oxides and oxygen.

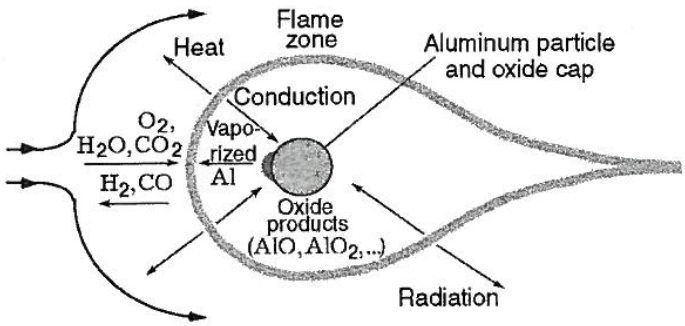

Figure 4.2: A schematic view of an aluminium particle combustion and oxidation process, [93].

It should also be noted that the burn time for Al particles is not modelled according to the standard 'D^2 – law', which states that the burning time of a droplet/particle is proportional to its area, [94], which is common in hydrocarbon combustion. Here, as Eq. 4.7 will show, the diameter has an exponent of 1.8. This is done to account for the oxide cap formation (on the Al particle surface), which reduces the exposed area of Al able to combust, [93].

In the Al combustion model used in this work, the processes of condensation and dissociation have been sacrificed to the benefit of cost–effectiveness of the code. There are models described in [19, 93, 95–97], which can be adopted to model these processes, here however several approximations and assumptions have been made:

1. An unburned Al particle is always covered by a very thin coating of aluminium oxide, Al_2O_3, which has to melt before the aluminium can be gasified and Al sub–oxides start to form, in this work however, this coating is disregarded from, hence

2. The vaporization of Al occurs when $T \geq 2971$ K and the amount of gaseous Al is determined by Eqs. 4.6 and 4.7;

3. The condensation reaction is modelled by a global reaction taken from [95], to incorporate this exothermic heat release;

4. Dissociation reaction is neglected.

The reaction mechanism used for Al combustion is presented in Tab. 5.1, Chapter 5.

4.2 Governing Equations in Lagrangian Frame

The solid particles are assumed to be spherical and do not deform during collisions. For simplicity, the following particle description is applied on a 'computational particle' in the solver. This means that the physical system that contains N_p total number of particles is simulated using N_c number of computational particles, where each computational particle contains $n = N_p/N_c$ 'real', physical particles. The density of the computational and the physical particle is kept the same, so the volume (or diameter) and the mass of the physical particle are scaled up for the computational particle in order to maintain the density by

$$\begin{cases} v_p = nV_D, \\ d_p = Dn^{1/3}, \end{cases} \tag{4.1}$$

where v_p and d_p are the volume and the diameter of a computational particle, respectively and V_D and D are the volume and the diameter for the physical particle.

In the present Lagrangian frame a particle P is defined by its centre $\mathbf{x_p}$, its diameter d_p, its velocity $\mathbf{U_p}$ and its mass m_p. Each particle position vector is calculated from the equation

$$\frac{\mathrm{d}\mathbf{x_p}}{\mathrm{d}t} = \mathbf{U_p}, \tag{4.2}$$

and the motion of a particle is govern by Newtons law of motion, as is shown by the governing equations for particle motion and combustion, [42, 98]

$$\begin{cases} \frac{\mathrm{d}m_p}{\mathrm{d}t} = \dot{m}_p = -\pi d_p^2 \rho_p \frac{\mathrm{d}d_p}{\mathrm{d}t}, \\ m_p \frac{\mathrm{d}\mathbf{U_p}}{\mathrm{d}t} = \mathbf{D_p} - \frac{1}{6}\pi d_p^3 \nabla p, \\ m_p c_{p_p} \frac{\mathrm{d}T_p}{\mathrm{d}t} = \pi d_p \kappa_g Nu(T - T_p) - \dot{m}_p L_v + \pi d_p \epsilon \sigma (T^4 - T_p^4). \end{cases} \tag{4.3}$$

Here, $\mathbf{D_p}$ is the drag force, c_{p_p} the specific heat capacity of the particle, T_p the particle temperature, κ_g the thermal conductivity of the gas phase, Nu the Nussel number, L_v the latent heat of vaporisation for the particle, ϵ the emissivity of the particle and σ the Stefan–Boltzmann constant. The drag force acting on particle is defined as

$$\mathbf{D_p} = \frac{1}{2}\rho C_D A |\mathbf{u} - \mathbf{U_p}|(\mathbf{u} - \mathbf{U_p}), \tag{4.4}$$

in which A is the cross section area of the particle and C_D is the drag coefficient taken as, [42],

$$C_D = \frac{24}{Re_r} + \frac{4.4}{\sqrt{Re_r}} + 0.42, \tag{4.5}$$

where $Re_r = \rho d_p |\mathbf{U_p} - \mathbf{u}|/\mu$ is the relative Reynolds number. It should be noted that there are many expressions for the drag coefficient in the literature and there seems to be no general rule for when the different expressions are used. In this application the drag coefficient definition in Eq. 4.5 is chosen due to its common usage in afterburning application by other groups, [14, 16, 19, 42, 47]. Many of these drag coefficient expressions are summarized in [42].

The burning rate of a particle, $\frac{\mathrm{d}d_p}{\mathrm{d}t}$ is expressed as,

$$\frac{\mathrm{d}d_p}{\mathrm{d}t} = -\frac{d_p}{t_b}, \tag{4.6}$$

where t_b is the burn time of the particle, which is the most important modelling parameter in particle combustion. Since this applications deals with aluminium particles, several burn time models are available in [99–105]. Here the burn time model for an aluminium particle is taken from [106], which is also used in [100, 102] and takes into account the surrounding pressure and temperature as well as the oxidizer used in aluminium combustion, according to:

$$t_b = \frac{a d_p^n}{X_{eff} p^{0.1} T^{0.2}} \quad \text{s.} \tag{4.7}$$

Here, $a = 4.64 \cdot 10^5$ and $n = 1.8$ are constants, [106], $X_{eff} = C_{O_2} + 0.6 C_{H_2O} + 0.22 C_{CO_2}$ is the effective concentration of the oxidisers present. Even thou it is known that aluminium will afterburn and react with water vapour and carbon dioxide, as is the case in anaerobic afterburning, in this however work, only aluminium combustion with oxygen is considered, $X_{eff} = C_{O_2}$.

4.2.1 Particle Collision Model

This two–phase model includes collisions between particles, as it has been shown in [25], to be important for the particle flow and combustion. These collisions are modelled by the Hard Sphere collision model, [94]. A pair of particles will collide if only (i) they are in the same cell and (ii) if they are moving towards each other. The particle deformation is neglected, that is, throughout the collision process, the distance between the particle centres of mass is constant and equal to the sum of particle radii.

Figure 4.3 shows a schematic overview of a particle collision and the definitions of the particle velocities and the impulsive force. The equation of motion for two particles, with masses m_1 and m_2 and velocities before collision $\mathbf{v_1}$ and $\mathbf{v_2}$, respectively, after a collision is given by,

$$\begin{cases} m_1(\mathbf{v_1'} - \mathbf{v_1}) = \mathbf{J}, \\ m_2(\mathbf{v_2'} - \mathbf{v_2}) = -\mathbf{J}, \end{cases} \tag{4.8}$$

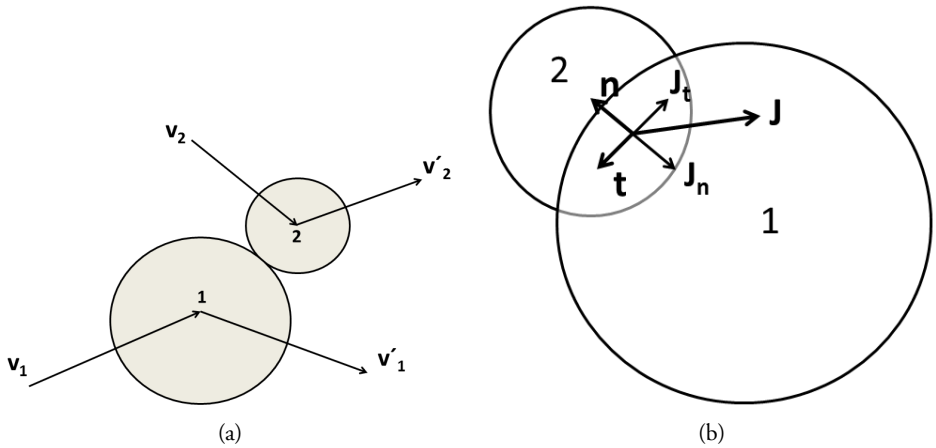

Figure 4.3: A schematic view of (a) particle collision and (b) impulsive force during particle collision.

where $\mathbf{v_1'}$ and $\mathbf{v_1'}$ are the post–collision velocities of particle 1 and 2, respectively and $\mathbf{J}$ is the impulsive force acting on particle 1 (and also on particle 2 as a reaction force). The impulsive force consist of two contributions, a contribution of motion in a normal direction, $J_n\mathbf{n}$, and a contribution to motion due to sliding, $J_t\mathbf{t}$, that is $\mathbf{J} = J_n\mathbf{n} + J_t\mathbf{t}$, where $\mathbf{n}$ and $\mathbf{t}$ are normal and tangential unit vectors, respectively, as shown in Fig. 4.3b. The sliding contribution to the impulsive force is only non–negligible in cases with dense particle flow, hence in this application we assume that the particles, post–collision, will travel in the normal direction only, yielding $\mathbf{J} = J_n\mathbf{n}$. The normal component of the impulsive force is defined as, [94]

$$J_n = -\frac{m_1 m_2}{m_1 + m_2}(1+e)\Big(\mathbf{n}\cdot(\mathbf{v_1} - \mathbf{v_2})\Big). \tag{4.9}$$

Combining Eqs. 4.8 and 4.9 and solving for the post–collision particle velocities yields,

$$\begin{cases} \mathbf{v_1'} = -\frac{m_2}{m_1+m_2}(1+e)\Big(\mathbf{n}\cdot(\mathbf{v_1} - \mathbf{v_2})\Big)\mathbf{n} + \mathbf{v_1} \\ \mathbf{v_2'} = \frac{m_1}{m_1+m_2}(1+e)\Big(\mathbf{n}\cdot(\mathbf{v_1} - \mathbf{v_2})\Big)\mathbf{n} + \mathbf{v_2}, \end{cases} \tag{4.10}$$

and in case of particles having the same masses, Eq. 4.10 simplifies to

$$\begin{cases} \mathbf{v_1'} = -\frac{1}{2}(1+e)\Big(\mathbf{n}\cdot(\mathbf{v_1} - \mathbf{v_2})\Big)\mathbf{n} + \mathbf{v_1} \\ \mathbf{v_2'} = \frac{1}{2}(1+e)\Big(\mathbf{n}\cdot(\mathbf{v_1} - \mathbf{v_2})\Big)\mathbf{n} + \mathbf{v_2}. \end{cases} \tag{4.11}$$

Here, e is the coefficient of restitution and the normal unit vector is defined as $\mathbf{n} = \frac{\mathbf{x_2}-\mathbf{x_1}}{|\mathbf{x_2}-\mathbf{x_1}|}$ where $\mathbf{x}$ is the position of the particle before the collision.

4.2.2 Source Terms

The particle influence the fluid by depositing combusted mass, exerting force and taking heat for combustion, this is expressed in source terms S_p, $\mathbf{F_p}$ and H_p, respectively. The source terms in Eq. 3.6 are calculated as contributions that are generated by a particle in each cell visited along it path during one Eulerian time step. The contribution of all particles, which have been in cell k (of volume V_k) during the Eulerian time step is calculated as sums over all particle contributions per number of particles, N_k, visiting the cell, resulting in the following expressions for the source terms

$$S_p = \frac{1}{V_k N_k} \sum_p \dot{m}_p \tag{4.12}$$

$$\mathbf{F_p} = \frac{1}{V_k N_k} \sum_p \Big(- \mathbf{D_p} + \frac{1}{6}\pi d_p^3 \nabla p + \dot{m}_p \mathbf{U_p} \Big) \tag{4.13}$$

$$H_p = \frac{1}{V_k N_k} \sum_p \Big(\pi d_p \kappa_g N u (T_p - T) + \dot{m}_p h_p - \mathbf{D_p U_p} + \frac{1}{6}\pi d_p^3 \nabla p \mathbf{U_p} \Big). \tag{4.14}$$

Chapter 5

Chemical Kinetics

In order to simulate any combustion process using finite rate chemistry LES, a model of the reaction progress for all species most be used. Such model consists of a set of reactions, called a reaction mechanism, ranging from one reaction up to several thousands, where each reaction has a certain reaction rate, which is usually modelled by an Arrhenius law.

The choice of the reaction mechanism is commonly a trade-off between computational capability and accuracy. *Global reaction mechanisms*, consisting of only a few reactions and species, only include global reactions, that is reactions that do not physically occur but rather expresses the overall chemical process. At the other extreme are the *detailed reaction mechanisms* that include all intermediate reaction steps and typically involve hundreds or thousands of reactions, and hundreds of species. Detailed reaction mechanism consist only of elementary reactions, that is reactions that do physically occur, but these mechanisms, due to their size are generally considered too comprehensive and hence too computationally expensive for finite rate LES. Most recently the use of *skeletal reaction mechanisms*, which are the simplified versions of the detailed mechanism, have gained increasing acceptance, [107, 108]. The aim of a skeletal mechanism, which mostly contains elementary reactions, is to reduce the number of reaction and yet retain most of the features of the detailed mechanism.

The most common hydrocarbon fuel in premixed combustion simulations is methane, CH_4, for which there are several of reaction mechanisms in each category, from global to detailed. When designing a reaction mechanism, typical variables such as laminar flame speed, ignition delay time, flame temperature and species concentrations of major species such as CO_2, H_2O and CO, are aimed to be modelled correctly at initial gas pressure and temperatures, for as wide range of equivalence rations, as possible. These variables describe overall characteristics of the flame and are of more or less importance depending on the flame type (e.q. flame speed is more important for premixed flames, while ignition delay time is more important for non-premixed, high speed flames). Two typical reaction mechanisms validation plots, for CH_4, of the laminar flame speed, s_u and the ignition delay time, τ_{ign}, as a function of equivalence ratio, ϕ, and the inverse of temperature, respectively,

are presented in Fig. 5.1, where different lines represent different reaction mechanisms and the symbols, the experimental data. Such plots are rare, if completely non-existent for post-detonation afterburning flames.

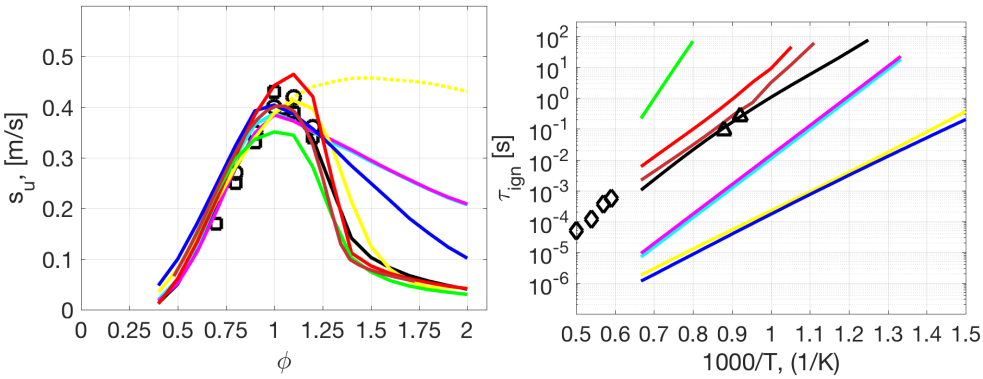

(a) (b)

Figure 5.1: Comparison of (a) laminar flame speeds, s_u at 1 atm and 300 K, and (b) ignition delay times, τ_{ign} at 1 atm.

To use finite rate chemical kinetics in this application is a rather unconventional. Kuhl *et.al.* and Balakrishnan [42], to mention some, have used infinitely fast chemistry, often under the assumption that $Da, Re \rightarrow \infty$ and the fact that the afterburning region is effectively a diffusion flame. One drawback with using finite reaction rates is that the mechanisms are oversimplified and/or developed (i.e. tailored) for other applications and in the case of aluminium combustion, such application is solid rocket combustion. Basically, there is no praxis as what is valid or appropriate regarding chemical kinetics in afterburning applications. The application of finite rate kinetics is therefore left up to individual researcher.

Despite the error that simplified kinetic mechanism brings, it also brings an opportunity to investigate heat-release, turbulence chemistry interaction, etc., and actually add a degree of physical accuracy given that the mechanism used is designed for similar applications that it is applied in. Also, as the stabilizing mechanism in afterburning combustion might occur through auto-ignition, chemistry and subsequent afterburning will be greatly affected by finite rate combustion.

The research of finite rate LES for premixed flames has already evolved past infinitely fast chemistry and global reaction mechanism, with skeletal mechanisms emerging as new and improved way of simulating turbulence chemistry interaction and flame propagation. The importance of including a reaction mechanism into an LES combustion simulation is acknowledged. The research in finite rate LES for non-premixed flames is lagging behind, and this work represents the initial steps in the similar evolution, as for premixed flames, attempting to show feasibility with these kind of simulations. By including a reaction

mechanism, the flow and combustion are better represented, physically.

Hence, this work uses finite reaction rates of Arrhenius form

$$\dot{w}_i = M_i P_{ij} \dot{w}_j \quad \text{with} \quad \dot{w}_j = A_j T^n e^{(-T_{a_j}/T)} \prod_{j,i} (\rho Y_i / M_i)^{\alpha_i} \tag{5.1}$$

considering only the forward reactions, in which P_{ij} is the stoichiometric coefficients, $\dot{w}_j$ the reaction rate of j^{th} reaction step, A_j the Arrhenius pre–exponential factor, $T_{a,j}$ the activation temperature and α_i the reaction orders of reaction step j.

5.1 TNT Combustion

For TNT combustion there exists a detailed mechanism for TNT decomposition, [109], but that does not necessary apply to afterburning. There is a potential to develop a skeletal mechanism but since the carbon that is the main fuel in TNT first burns as a carbon particle, there is a lack of experimental species data, the choice here was to use a global mechanism for carbon afterburning, to capture the main exothermic reactions from the TNT afterburning. Hence, in all of the simulations a reduced TNT mechanism developed by Tran, [110], is employed, implemented here as a two–step mechanism:

$$\begin{array}{lrcl} (\mathrm{C0}) & \mathrm{C_7H_5N_3O_6} & \rightarrow & 1.5\mathrm{N_2} + 2.5\mathrm{H_2O} + 3.5\mathrm{CO} + 3.5\mathrm{C_{(g)}} \\ (\mathrm{C1}) & \mathrm{C_{(g)}} + \frac{1}{2}\mathrm{O_2} & \rightarrow & \mathrm{CO} \\ (\mathrm{C2}) & \mathrm{CO} + \frac{1}{2}\mathrm{O_2} & \rightarrow & \mathrm{CO_2} \end{array}$$

where (C0) represents the initial decomposition of TNT ($\mathrm{C_7H_5N_3O_6}$) into $\mathrm{N_2}$, $\mathrm{H_2O}$, CO and $\mathrm{C_{(g)}}$, where the subscript (g) entails that the carbon is assumed to be in gaseous state. The decomposition of $\mathrm{C_7H_5N_3O_6}$ into detonation products is much more complicated than described by the one–step mechanism above, e.g. [109], and includes a wide range of species appearing typically in small concentrations. However, in order to simplify the computational model to something tractable for LES we adopt this decomposition reaction (C0) that is given by modified the Kistiakowsky-Wilson rule, [111]. The subsequent two exothermic reactions represent the afterburn process, in which C and CO are oxidized into CO and $\mathrm{CO_2}$, respectively.

5.2 Aluminium Combustion

Several 'detailed' mechanism are available in the open literature for combustion of Al-$\mathrm{H_2O}$, [112], Al-$\mathrm{CH_4}$-air, [113], mixtures, and different 'submechanisms' that consider Al/C/H/O oxidation, [95, 114–117]. All of these are usually tailored for a certain Al combustion regime (diffusion/kinetic), depending on the application. The experimental data is usually available for a singe spherical particle combustion.

For TNT/Al combustion in this work, a global submechamism outlined in Tab. 5.1 has been used. This mechanism has been complied based in the most important reactions

in aluminium combustion outlined in [93], aiming at capturing the processes described in previous chapter.

Table 5.1: Rate parameters for $C - O_2$ and $Al - O_2$ reaction mechanisms.

No.	Reaction	A[m, kg, mol, s, K]	m	T_a[K]	Reference
C1	$C + \frac{1}{2}O_2 \rightarrow CO$	$4.84 \cdot 10^{11}$	0	5000	[110]
C2	$CO + \frac{1}{2}O_2 \rightarrow CO_2$	$6.29 \cdot 10^{12}$	0	8000	[110]
A1	$Al_{(g)} + O_2 \rightarrow AlO + O$	$1.13 \cdot 10^{11}$	0	80	[93]
A2.	$AlO + O_2 \rightarrow AlO_2 + O$	$3.36 \cdot 10^{11}$	0	10008	[93]
A3	$AlO_2 \rightarrow AlO + O$	$5.08 \cdot 10^{10}$	0	48312	[95]
A4.	$O + O + M \rightarrow O_2 + M$	$2.41 \cdot 10^{13}$	-0.5	0	[93]
A5	$2AlO + \frac{1}{2}O_2 \rightarrow Al_2O_3$	$7.27 \cdot 10^{22}$	0	0	[95]

Chapter 6

Experimental Compaign

For the purpose of the validation of the mathematical two–phase model presented in the previous chapter and to gain further understanding of the afterburning events an experimental campaign was conducted in June 2013. A summary of the charges and the HoB's is presented in Table 6.1. The experiments were set-up to both examine the effect of aluminium particles in the explosive compound and how the HoB affect the afterburning.

Table 6.1: Summary of the conducted experiments

No.	Charge	Weigh [kg]	HoB [m]
1	TNT	0.9103	0.15
2	TNT	0.9425	0.5
3	TNT	0.9093	1
4	TNT	0.9002	2
5	TNT/Al	1.0514	2
6	TNT/Al	1.0146	1
7	TNT/Al	1.0666	0.5
8	TNT/Al	1.0009	0.15
9	TNT	0.913	0.5
10	TNT	1.845	1
11	TNT	1.87	0.5

6.1 Experimental Set-Up and Measurements

A schematic view of the experimental setup is shown in Fig. 6.1a, the charge was hanged at four different heights above ground; at 0.15 m, 0.5 m, 1.0 m and 2.0 m. Three pressure sensors were placed 2 m apart from the charge centre and a pyrometer, for temperature measurements was placed along the 2.0 m radius, pointing upwards to measure the tem-

perature approximately 1.5 m in the air. Figures 6.1b and c show the pressure sensors and the pyrometer in the experimental set-up, respectively.

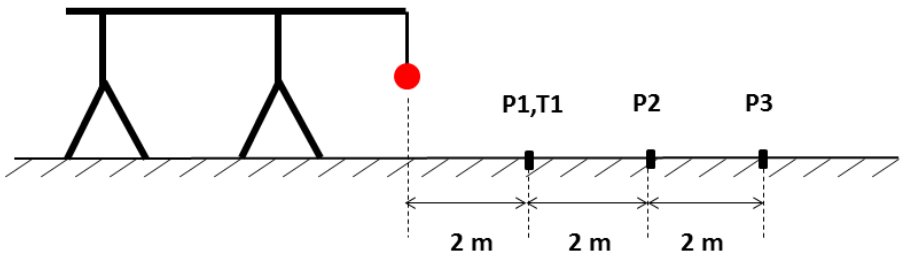

(a)

(b)

(c)

Figure 6.1: (a) A schematic view of the experimental set-up and pressure sensor locations, (b) pressure sensors P1–P3 and (c) pyrometer, T1.

The pressure signals were recorded by a HBM high speed transient data acquisition system, Gen7i, which sampled the data at 1 MHz with the resolution of 16 bit. Piezoelectric pressure sensors from PCB (P1–P3) were used and were placed flush on the ground. The sensors have to be charged and amplified. This was done by a PCB584 signal conditioner with 100 kHz bandwidth. An extra wire was put directly into the charge. On detonation this wire was short–cut and the exact time of detonation was recorded. The temperature measurement was done with an Optris LT1MH pyrometer, capable of measuring temperature between 650 and 1800 degrees Celsius at a rate of 1 kHz.

All of the experiments were filmed with a high speed video camera, Photron FASTCAM-ultima APX 120KC, the setup of which is shown in Fig. 6.2a. The camera enables 6000 fps with a resolution of 512x512 pixels. The shutter speed was set fixed at 4 μs. Experiments 8–11 (Tab. 6.1) were also filmed from the air by a UAV, a model helicopter equipped with a camera, shown in Figs. 6.2b and c. The model helicopter is of a type DJI Phantom, which is a multi–rotor vehicle, commonly named "Quadrocopter", since it is equipped with four propellers and a control system that enables some autonomy, which can be used to hover at a position with an accuracy of $\pm$0.8 m in the vertical direction and $\pm$2.5 m in the hori-

zontal direction. The experiments were filmed using Gopro Hero 3 Black Edition camera fitted to the Quadrocopter, the camera had a resolution of 960x1280 pixels and a frame speed of 100 fps.

(a) (b) (c)

Figure 6.2: Filming of the experiments was done by (a) Photron APX camera on the ground and (b) & (c) Quadrocopter from the air in experiments 8–11.

Eleven charges were made for this campaign, 9 charges weighing 1 kg and 2 charges weighing 2 kg. TNT (2,4,6–trinitrotoluene) was chosen as the base charge due its good afterburning qualities and the reasonably well documented physical and thermodynamic properties. All of the charges were moulded into spherical shapes with a small hollowed–out cavity at the top of each charge for the booster charge and the trigger wire. Figure 6.3 shows the charges used in the experiments. A 30 g plastic explosive (PETN model 46) booster was used for 1 kg charges and a 45 g booster of the same explosive for the 2 kg charges. Four of the charges were enhanced with aluminium particles of type A100 (mean particle diameter of 42 μm), with a weigh distribution TNT/Al = 80/20 %.

(a) (b)

Figure 6.3: (a) Charges used in the experiments and (b) an example of the charge in the experimental setup.

Figure 6.4 shows the charges at the four different HoB's that were used during the experiments, the charges were put into a netted bag, by which these were hung from the

scaffolding to a fixed height. To ensure that the wind and the pendulum effect did not move the charge from its position, the charge was secured by three thin wires that were weighted down by rocks, as seen in Fig. 6.4.

(a) (b)

(c) (d)

Figure 6.4: Four HoB varied in the experiments (a) 0.15 m, (b) 0.5 m, (c) 1.0 m and (d) 2.0 m.

6.2 Experimental Results

Figure 6.5 presents results from pressure (a–c) and Fig. 6.6 presents the temperature measurements from 1 kg charges. A common trend for all pressure probes is that the inclusion of aluminium increases pressure magnitude, as expected. The use of aluminium also increases the shock speed, whereas the heat release from the aluminium reactions induces a volumetric expansion in the flow, which in turn accelerates the shock further. The highest pressure magnitudes are found for HoB 2 m cases. Examining the first probe, P1, in Fig.

6.5a one observes that HoB 0.5 m has the next highest pressure magnitude after HoB 2 m. This effect of an "intermediate" HoB resulting in significant blast effect has been noted also in [50] and is due to a self–sustaining system of ground reflected shocks that pulsate up and downwards, creating Mach–stems, [118], of merged shocks, thereby increasing the pressure magnitude of the shock travelling parallel to the ground towards the pressure probe. This pulsating shock system is clearly visible for TNT/Al–HoB 0.5 m as quite long pressure decrease after the primary shock spike. For the remaining probes P2 and P3 in Fig. 6.5b and c, respectively, the shock magnitudes have decreased by a factor of two, the highest pressures for TNT/Al are found for HoBs 0.5 m and 1 m, with HoB 0.5 m exhibiting stronger secondary shock at 10 ms in Fig. 6.5b, due to aforementioned reasons. At P3, 6 m away from the detonation center, the shock magnitudes for all cases are almost equal and quite intermittent as the secondary shock has caught up with the primary shock.

Regarding the temperature measurements in Fig. 6.6 the first observation made is that the time scale of the measurements is quite long due to the sampling frequency of the pyrometer, compared to the pressure measurements, hence the 'long term' effect of the afterburning can be examined. The highest temperatures are achieved for the cases with aluminium inclusion, as expected. There are clear trends in the temperature dependence on the HoB; the highest temperature is attained for 2 m and 0.15 m followed by 1 m and 0.5 m. The reason for the lowest temperature for 0.5 m case is yet again the pulsating shock system which elongates the combustion region (seen from films) compared to other cases, where the combustion region has a spherical expansion (HoB 2 m and 1 m) and half–spherical (HoB 0.15 m). The elongated shape of the combustion region in HoB 0.5 m makes that only the edges of it are exposed to the pyrometer measurement position.

To briefly investigate the validity of the experimental data, the pressure traces for pure TNT at P1–P3 were compared to calculation in CONWEP, [119], which provides conventional weapon calculations based on experimental data database and empirical relationships. The result of the comparison is shown in Tab. 6.2 in terms of maximum value of the pressure peak. The experimental data and the data from CONWEP correlate well for P2 and P3, for P1 however the experiments show much higher pressure peak values. This can be attributed to the fact that CONWEP is not calibrated for near–ground detonations, and since the results from P2 and P3 are satisfactory, the experimental data is deemed reliable.

Table 6.2: Validation of experimental data. Comparisons of the pressure peak values [kPa] for the experimental data (left) and data taken from CONWEP, [119] (right).

HoB [m]	P1	P2	P3	HoB [m]	P1	P2	P3
2	441	100	45	2	276	87	44
1	372	88	35	1	243	66	32
0.5	375	86	32	0.5	220	56	28
0.15	297	67	27	0.15	232	50	25

To make further use of films that where made during experiments an image post-

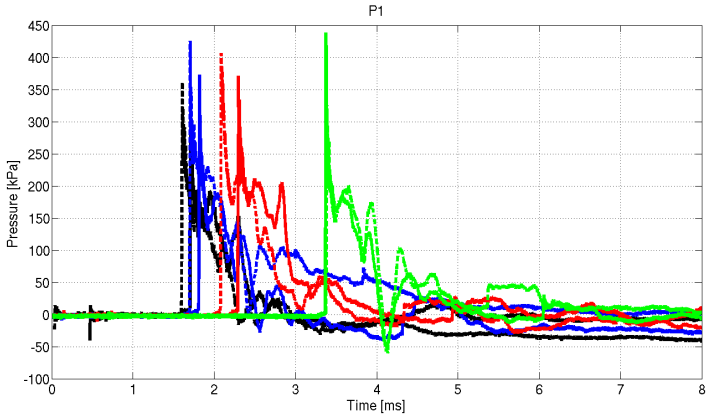

(a) P1

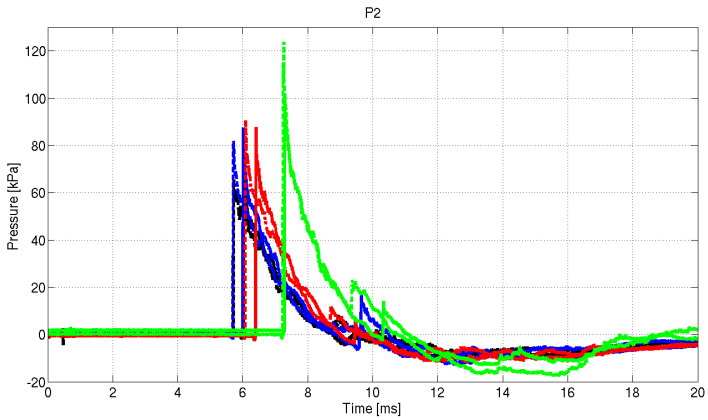

(b) P2

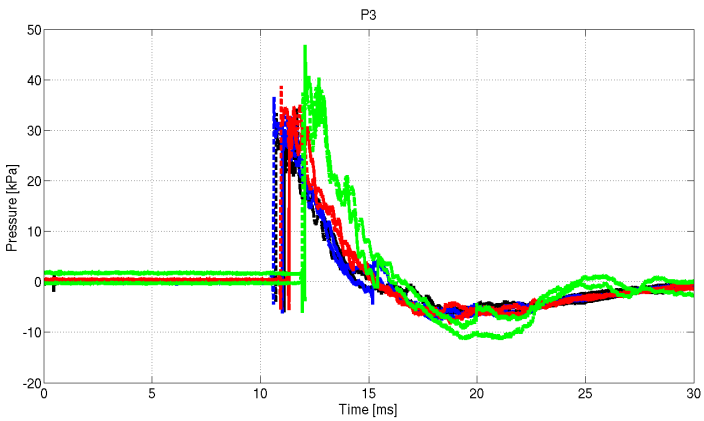

(c) P3

Figure 6.5: Pressure traces. Legend: TNT–HoB 0.15 m (–), TNT–HoB 0.5 m (–), TNT–HoB 1 m (–), TNT–HoB 2 m (–), TNT/Al–HoB 0.15 m (– –), TNT/Al–HoB 0.5 m (– –), TNT/Al–HoB 1 m (– –), TNT/Al–HoB 2 m (– –).

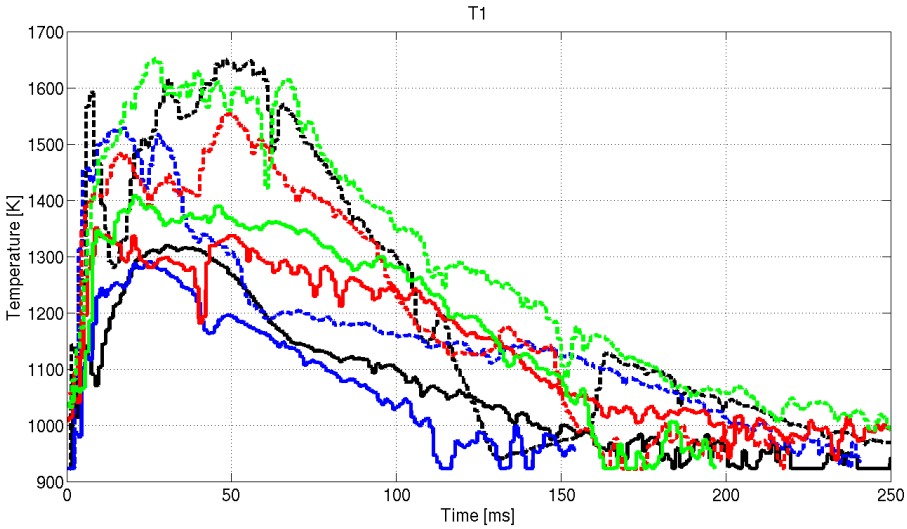

Figure 6.6: Temperature traces. Legend: TNT–HoB 0.15 m (–), TNT–HoB 0.5 m (–), TNT–HoB 1 m (–), TNT–HoB 2 m (–), TNT/Al–HoB 0.15 m (– –), TNT/Al–HoB 0.5 m (– –), TNT/Al–HoB 1 m (– –), TNT/Al–HoB 2 m (– –).

processing was conducted of these films, from which data regarding the spatial expansion of the combustion region and the light intensity was extracted to further elucidate the afterburning qualities of the charges examined at different HoB. The image post–processing was done in MATLAB, and every frame from the film was separated into its RGB (Red, Green, Blue) components, these pixel groups were then plotted separately, as is shown in Fig. 6.7 where in the top left corner is the original film frame, in the top right corner the red component, in the bottom left corner the green component and in the bottom right corner the blue component for (a) TNT/Al–HoB 0.15 m and (b) TNT–HoB 0.15 m respectively. In order to only visualise the combustion region, and avoid the shock wave illumination and the background, a limiter was used on the RBG components to show only the combustion region (detonation product cloud). The limiter varied depending on the case, since the TNT/Al charges were much more bright than the pure TNT charges. This can be seen in Fig. 6.7, comparing (a) and (b) where the same limiter was used on both cases. From these images, an ”illuminated” area could be extracted – a relative area of combustion region, that is the region of the images that is non–black, giving a qualitative value of the area of the combustion region. Also, by summing all the RGB values for the non–black pixels a qualitative value of a ”relative (light) intensity” was obtained, which should correlate to the heat radiated from the combustion region. Due to the use of the limiter, the following image post–processing results can only be viewed as qualitative, giving general information regarding the light intensity and combustion region expansion.

Figures 6.8 and 6.9 show the results from the image post–processing in terms of Rela-

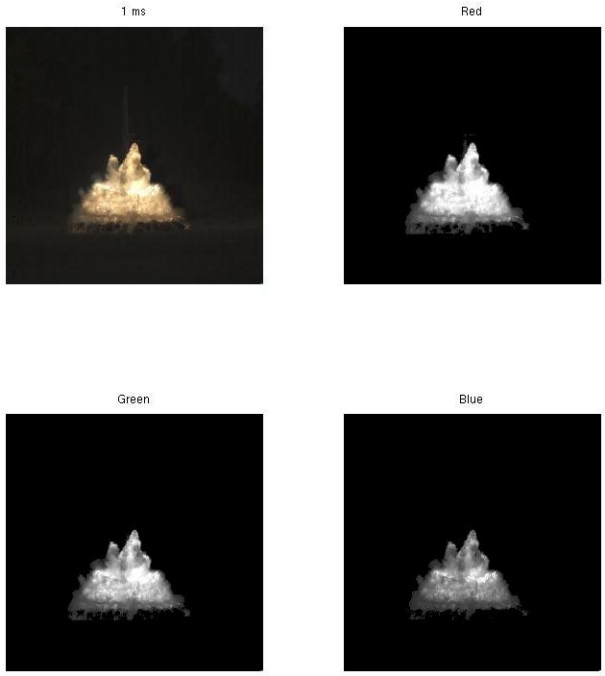

(a)

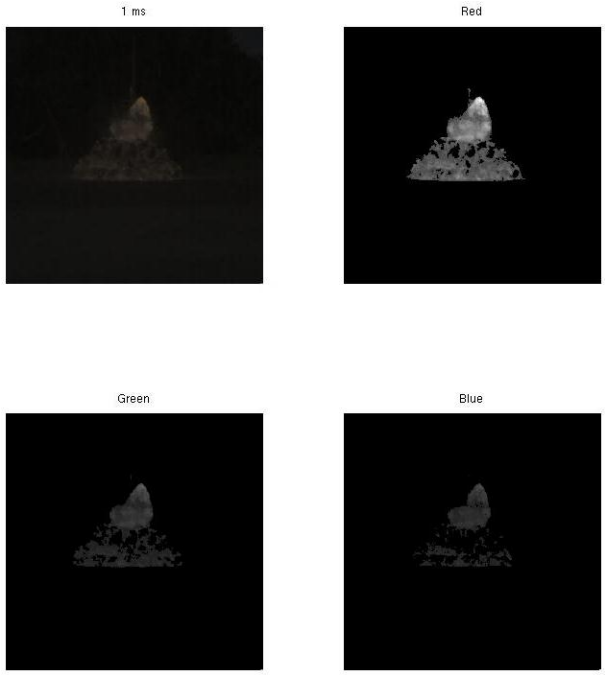

(b)

Figure 6.7: Image post–processing example: (a) TNT/Al–HoB 0.15 m, (b) TNT–HoB 0.15 m.

tive Intensity (RI) and Relative Area (RA), respectively, for all the cases. The RI and RA are presented as normalized with maximum value of RI and RA, respectively of all cases. Examining Fig. 6.8a, the RI for the TNT/Al cases shows a spike in intensity in early times (0–10 ms) and slow decrease afterwards, aluminium combustion is more "light" intense than the pure TNT (carbon) combustion. Early fluctuations in RI are seen TNT/Al cases attributed to the mixing layer evolution as the ground reflected shocks establish the mixing layer and a stable combustion region. From 10 ms and onwards the primary shock has propagated away from the combustion region and the ground reflections have weakened, culminating in the final plateau in the RI curve before the remaining fuel is consumed at seemingly linear rate as the RI decreases. For pure TNT cases the RI profiles fluctuate more at early times (0–10 ms), due to the mechanism of combustion region evolution due to shock and mixing layer interaction and flow instability generation. These initial fluctuations are 50% less in RI than for TNT/Al cases, due to the fact that carbon combustion is not as "bright" as aluminium combustion. At later times, as the mixing layer is established, and the combustion is slowly intensified to peak, after which a linear decrease is visible as for TNT/Al cases. From these results it appears that the aluminium inclusion provides a boost in the heat radiation at earlier times compared to pure TNT charges, which in their turn require an established mixing layer (fuel and air mixed well) prior to combustion. From Fig. 6.8a it is visible that the afteburning phase for the pure TNT cases occurs at 30–50 ms, while for the TNT/Al cases this phase takes place during 0–30 ms, this is when, after initial fluctuations the afteburning plateaus before finally subsiding. The inclusion of aluminium is clearly enhancing the energy content in the system. The highest RI of the TNT/Al cases is achieved for the HoB 2 m case, while for the pure TNT cases the HoB 1 m, closely followed by HoB 0.5 m shows highest values of RI. This suggests that for TNT/Al afterburning, the shock – mixing layer interaction (established through ground reflection) is not as important for afterburning processes as for the pure TNT cases. TNT/Al afterburning are seemed mainly dependent on the supply of the oxidizer to combust, and the aluminium – oxygen combustion clearly dominates over the carbon – oxygen combustion. Figure 6.8b shows RI profiles for times 0–10 ms, to elucidate what happens at early times. TNT/Al cases exhibit an almost immediate rise of RI, which stabilizes after $\sim$ 1 ms at basically constant level. Pure TNT cases on the other hand have an initial peak in RI due to the detonation, where after RI decreases to a level of $\sim$ 40% of TNT/Al cases, fluctuating slightly as the mixing layer stabilizes, entraining air through the reflected shock - RT instability, interaction and building up enough combustible mixing.

Figure 6.9 presents RA profiles for times (a) 0–100 ms and (b) 0–10 ms. For TNT/Al cases an even increase in the area of the combustion region is seen, with minor initial fluctuations. For the pure TNT cases, the initial fluctuations have greater magnitude. After 10 ms, the fluctuations cease and a steady increase in RA starts that correlates well with the RI profiles. Looking at the time period for 0–10 ms in Fig. 6.9b, the area of the combustion region for the TNT/Al charges expands gradually, while yet again the area for the pure TNT charges fluctuates due to strong up– and downwashes created by the ground

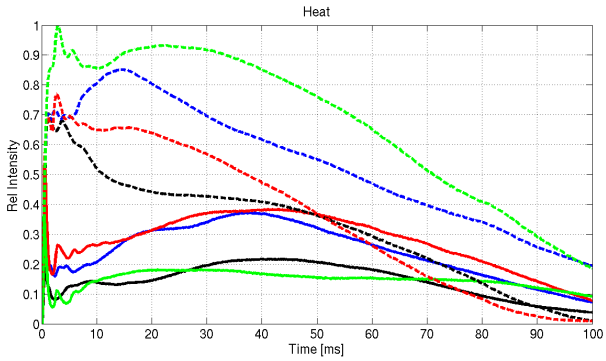

(a) Relative intensity for time 0–100 ms.

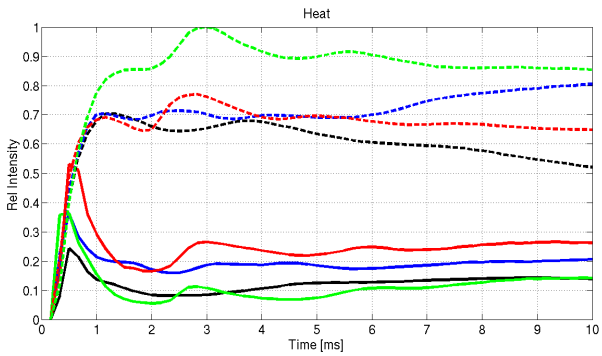

(b) Relative intensity for time 0–10 ms.

Figure 6.8: Imaging results. Legend: TNT–HoB 0.15 m (–), TNT–HoB 0.5 m (–), TNT–HoB 1 m (–), TNT–HoB 2 m (–), TNT/Al–HoB 0.15 m (– –), TNT/Al–HoB 0.5 m (– –), TNT/Al–HoB 1 m (– –), TNT/Al–HoB 2 m (– –).

reflected shocks, contracting and expanding the mixing layer. This also correlates with the RI profiles, where the peaks and valleys in both RI and RA for pure TNT charges can be attributed to the shock passages though the combustion region. This process occurs also for the TNT/Al charges, but is not at all visible due to the dominating aluminium combustion. Overall there are few discrepancies between the pure TNT and TNT/Al cases, however the TNT/Al clearly enables a larger combustion region. For TNT cases, the largest combustion region is associated with the highest intensity case, while for the TNT/Al cases the largest combustion region is attained after the intensity peak, indicating that the combustion cloud includes the aluminium oxide (Al_2O_3) that is present as a crown around the periphery of the combustion region.

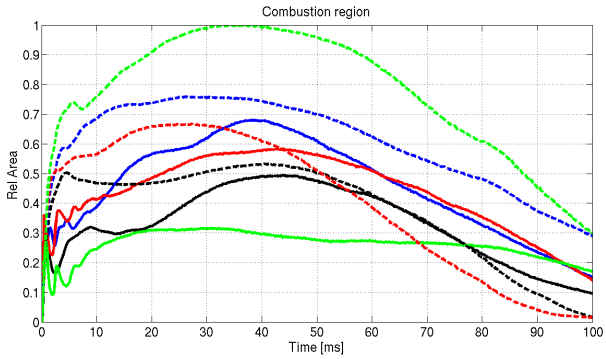

(a) Relative area for time 0–100 ms.

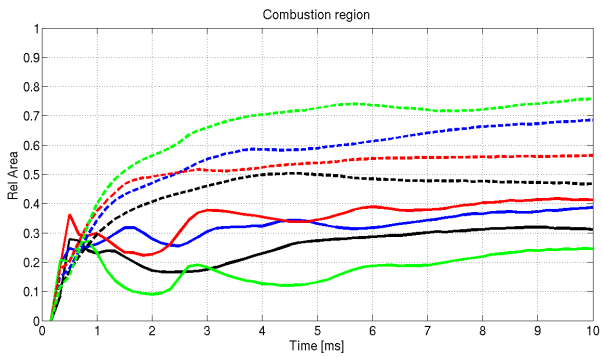

(b) Relative area for time 0–10 ms.

Figure 6.9: Imaging results. Legend: TNT–HoB 0.15 m (–), TNT–HoB 0.5 m (–), TNT–HoB 1 m (–), TNT–HoB 2 m (–), TNT/Al–HoB 0.15 m (– –), TNT/Al–HoB 0.5 m (– –), TNT/Al–HoB 1 m (– –), TNT/Al–HoB 2 m (– –).

Chapter 7

Simulations of Afterburning - Main Results

This chapter presents simulation results using the two–phase model described in Chapters 3 and 4. Table 7.1 shows the simulations that have been conducted and in the following section the simulation setup and the key simulation results are presented.

Table 7.1: Summary of performed simulations.

Case	Explosive	HOB	Comment
1	TNT (1.4kg)	unconfined	Paper I,II
2	TNT (1.4kg)	0.5 m	Paper I,II
3	TNT	0.2 m	Paper IV
4	TNT	0.5 m	Paper IV
5	TNT	1.0 m	Paper IV
6	TNT	2.0 m	
7	TNT/Al	0.2 m	Paper V
8	TNT/Al	0.5 m	Paper IV, V
9	TNT/Al	1.0 m	Paper IV, V
10	TNT/Al	2.0 m	Paper V

7.1 Simulation Set-Up

The simulation setup described here is valid for papers III-V. The simulation setup for papers I-II is very similar and for details on that, see papers I and II.

An explosive charge (TNT or TNT/Al) with a 20 cm radius was computationally detonated in air at four different HoB (0.2 m, 0.5 m, 1.0 m and 2.0 m). Figure 7.1 shows the computational domains for all HoBs. The computational domains have a rectangular shape of sizes outlined in the figures, with a spatial resolution of 0.01 m, resulting in domains from containing 75M to 222M cells. The detonation product cloud was initiated at

a given HoB above ground, while the rest of the domain was filled with air at atmospheric conditions. The ground was modelled by a no–slip boundary condition and a constant temperature of 298 K while all other boundary conditions were Neumann zero–gradient conditions. The initial conditions, representing the explosive decomposition and the for-

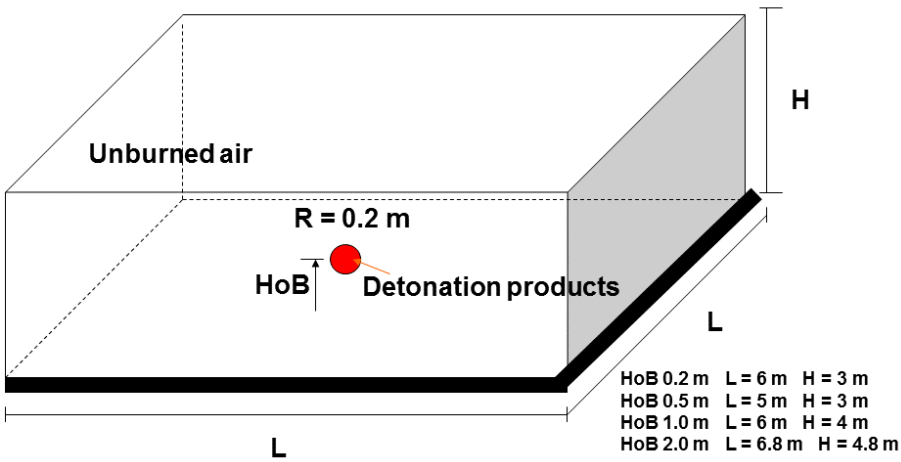

Figure 7.1: Compuational domain and setup.

mation of the initial cloud of hot Detonation Products (DP) at high temperature are shown in Fig. 7.2 and consisted of one–dimensional (1D) radial profiles of pressure, velocity, temperature and density spherically mapped onto the 3D grid, initial mass fractions of species were uniformly set through the radius of the detonation cloud and these values are presented in Tab. 7.2. It was assumed that initial aluminium present in the system has not yet started to react with air, hence no aluminium–oxygen combustion product were initiated, only solid and gaseous aluminium were present at time zero. The unburned air was set to have atmospheric pressure and temperature, as well as the air mass fractions oxygen, O_2, and nitrogen, N_2, of 0.23/0.77 respectively.

Table 7.2: Initial conditions for species.

Quantity	DP (cases 1 and 2)	DP (cases 3 and 4)	Air
Y_C	0.185	0.185(1-Y_{Al})	0
Y_{CO}	0.4317	0.4317(1-Y_{Al})	0
Y_{CO_2}	0	0	0
Y_{H_2O}	0.1982	0.1982(1-Y_{Al})	0
Y_{O_2}	0	0	0.23
Y_{N_2}	0.1851	0.1851(1-Y_{Al})	0.77

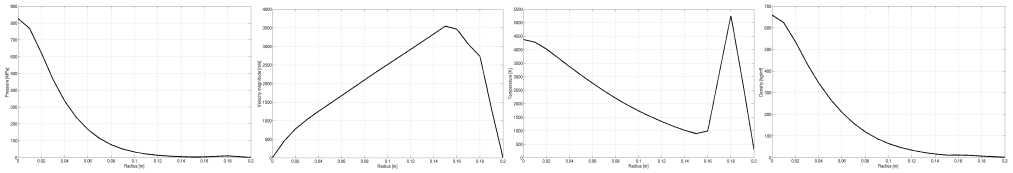

(a) (b) (c) (d)

Figure 7.2: 1D radial initial conditions for (a) pressure, (b) velocity, (c) temperature and (d) density.

7.2 Homogeneous Afterburning

As was mentioned in Chapter 2, the two key features critical for the mixing and afterburning of an explosion event are the RT and RM instabilities, which arise during the explosion. The RT instabilities are generated at the interface of two fluids of different densities, when this interface is accelerated, the heavier fluid will entrain into the lighter one, forming bubble shaped structures. During an explosion the interface between the shock compressed air and the detonation products is accelerated by means of a rarefraction wave propagating inwards, forming RT instabilities. In Fig. 7.3 the logarithm of the density is featured for different times of Case 1 to illustrate the development of these instabilities. The color schemes is dark for the heavy gas and light for light gas. At times 0.15 ms and 0.4 ms the first bubble structured RT instabilities emerge due to the rarefraction wave propagation (dark bubbles penetrating into the lighter surroundings). These instabilities form a thin mixing layer where combustion starts to take place (will also be seen in Figs. 7.5-7.8). The rarefraction wave will subsequently overexpand the flow, thereby creating a second shock, which will subsequently strengthen to the point of implosion. When this secondary shock eventually reflects from origin after the implosion, it will interact with the present RT instabilities, creating misaligned pressure and density gradients, thus giving rise to RM instabilities that arise due to these baroclinic effects. RM instabilities have almost the same shape as the RT, tending more to the mushroom shaped structures seen in Fig. 7.3 at times 0.8 ms, 1.2 ms and 2.0 ms (darks structures emerging at light background). These instabilities, RM and RT, will be seem to govern the mixing regions thus shaping the combustion patters in Fig. 7.4.

To better understand the interrelated processes of mixing and afterburning of the unconfined TNT-air explosion, Fig. 7.4 presents simultaneous contours of the carbon mass fraction, $\tilde{Y}_{\mathrm{C}}$, heat–release, Q, vorticity magnitude, $|\tilde{\omega}|$, in which $\tilde{\omega} = \frac{1}{2}\nabla \times \tilde{\mathbf{u}}$ is the vorticity, and the magnitude of the baroclinic production term, $(\nabla\bar{\rho} \times \nabla\bar{p})/\bar{\rho}^2$, at 3.0 ms, which is in the early stages of the afterburning stage from Case 1. The heat release, Q, is defined as

$$Q = \sum_i \left(M_i P_{ij} \overline{\dot{w}_j} h^{\theta}_{f,i} \right), \tag{7.1}$$

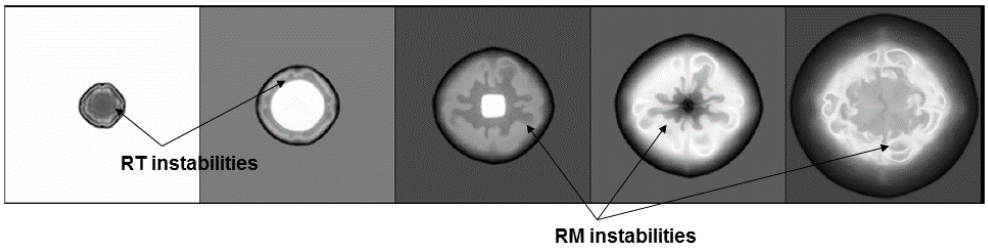

Figure 7.3: Time series of the unconfined TNT case of logarithm of density at times: from left to right: 0.15 ms, 0.4 ms, 0.8 ms, 1.2 ms and 2 ms.

where M_i is the molar mass of species i, P_{ij} the stoichiometric coefficients, $h^{\theta}_{f,i}$ the standard enthalpy of formation of species i and $\overline{\dot{w}_j}$ the filtered reaction rates.

The baroclinic production term results from reformulating the momentum equation into an equation for vorticity [120] whereby the baroclinic production term appears as a source term together with the vortex stretching and volumetric expansion terms, $(\nabla\tilde{\mathbf{u}})\tilde{\omega}$ and $(\nabla\cdot\tilde{\mathbf{u}})\tilde{\omega}$, respectively, such that

$$\partial_t(\tilde{\omega})+\nabla(\tilde{\omega})\tilde{\mathbf{u}}=(\nabla\tilde{\mathbf{u}})\tilde{\omega}+(\nabla\cdot\tilde{\mathbf{u}})\tilde{\omega}+(\nabla\bar{\rho}\times\nabla\bar{p})/\bar{\rho}^2+\nabla\times\left(\frac{1}{\bar{\rho}}\nabla\cdot(\bar{\mathbf{S}}-\mathbf{B})\right). \quad (7.2)$$

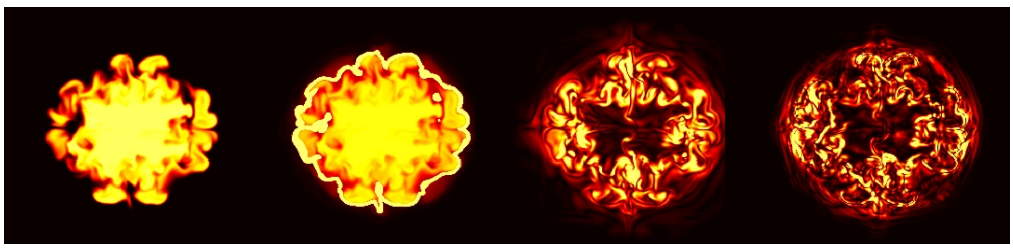

Figure 7.4: From left to right: $\tilde{Y}_{\mathrm{C}}$, Q, $|\tilde{\omega}|$ and $|\nabla\bar{\rho}\times\nabla\bar{p}|/\bar{\rho}^2$ for the unconfined TNT case, at 3 ms.

As will be seen in Figs. 7.5-7.8, the topological structure of the explosion cloud behind the outwards propagating shock wave is convoluted and partially fragmented due to the preconditioning caused by the implosion and secondary shock, and the associated RT and RM instabilities. In Fig. 7.4 $\tilde{Y}_{\mathrm{C}}$ represents the remaining fuel that (together with $\tilde{Y}_{\mathrm{CO}}$) continues to burn if additional air is supplied through convective mixing. Heat-release is seen to occur in topologically fragmented structures surrounding the fuel ($\tilde{Y}_{\mathrm{C}}$ and $\tilde{Y}_{\mathrm{CO}}$) distribution that still dominates the core of the detonation. The rate of heat release is controlled by the convective mixing of fuel and air from either side of the heat release zone, as a highly

turbulent diffusion flame. Comparing the Q and $|\tilde{\omega}|$ maps suggest that the vorticity is primary responsible for the fragmentation and the convective mixing between fuel and air as the vortex structures, taking the shape of slender filaments, wraps around the Q structures. The heat release affects the flow in different ways; (i) the increase in temperature causes the molecular viscosity to rise, thereby increasing the vortex diffusion, (ii) the heat release causes volumetric expansion, which in turn widens the vortical structures as understood by inspecting the vorticity equation, whereas the baroclinic production term, caused by the misalignment between the density and pressure gradients, generates vorticity by means of the misalignment between $\nabla\bar{\rho}$ and $\nabla\bar{p}$. By using the relation $T\nabla s = \nabla h - \nabla p/\rho$, the pressure gradient can be re–expressed in terms of the gradients of the enthalpy, $\nabla\bar{h}$, and entropy, $\nabla\bar{s}$, such that

$$\partial_t(\tilde{\omega}) + (\tilde{\omega})\tilde{\mathbf{u}} = (\nabla\tilde{\mathbf{u}})\tilde{\omega} + (\nabla\cdot\tilde{\mathbf{u}})\tilde{\omega} + \frac{1}{\bar{\rho}}\nabla\bar{\rho}\times\left(\nabla\tilde{h} - \tilde{T}\nabla\tilde{s}\right) + \nabla\times\left(\frac{1}{\bar{\rho}}\nabla\cdot(\bar{\mathbf{S}} - \mathbf{B})\right) \quad (7.3)$$

the right hand side of which is dominated by a delicate balance between the volumetric expansion $(\nabla\tilde{\mathbf{u}})\tilde{\omega}$ and the exothermicity $\frac{1}{\bar{\rho}}\nabla\bar{\rho}\times\nabla\tilde{h} \approx \frac{1}{\bar{\rho}}\nabla\bar{\rho}\times\nabla\tilde{h}_s \approx \frac{1}{\bar{\rho}}\sum_i\left(\nabla\bar{\rho}\times\nabla\tilde{Y}_i h^{\theta}_{f,i}\right)$. This illustrates how the exothermicity, through the baroclinic production term, generates vorticity in directions orthogonal to both $\nabla\bar{\rho}$ and $\nabla\tilde{Y}_i$, thereby resulting in the observed vorticity distribution being dominated by filaments wrapping around the larger structures of Q.

7.3 Influence of Ground Reflection

Figures 7.5–7.8 present the simulation results for HoB of 0.15 m, 0.5 m, 1.0 m and 2.0 m, respectively (cases 4 to 6 in Tab. 7.1). The results are shown in terms of λ_2 (defined in Eq. 7.4) (red-white) to visualize the shock propagation, mixing and flow features, and in terms of mass fraction of carbon dioxide (copper) to show the evolution of the afterburning and mixing regions for different times. λ_2 is defined as

$$\lambda_2 = \sqrt{|\nabla\widetilde{u_x}\cdot\nabla\widetilde{u_x} + \nabla\widetilde{u_y}\cdot\nabla\widetilde{u_y} + \nabla\widetilde{u_z}\cdot\nabla\widetilde{u_z}|} - |\nabla\times\tilde{\mathbf{u}}| \quad (7.4)$$

There are common features for all HoB, such as shock-turbulent mixing layer interaction, the rise of RT instabilities, due to impulsive acceleration of the interface between the detonation products and air, and, later, the development of the RM instabilities, as the ground reflected shocks affect the existing RT instabilities when they propagate through them. However, the HoB has a natural effect on the development of different kinds of shock systems, thereby also affecting the mixing and afterburning evolution patterns.

Figure 7.5 shows the results for HoB of 0.15 m above ground. The primary blast wave expands in all directions and at $\sim$ 0.2 ms the primary shock collides with and reflects from the ground. The ground reflected shock travels upwards, interacting with the thin

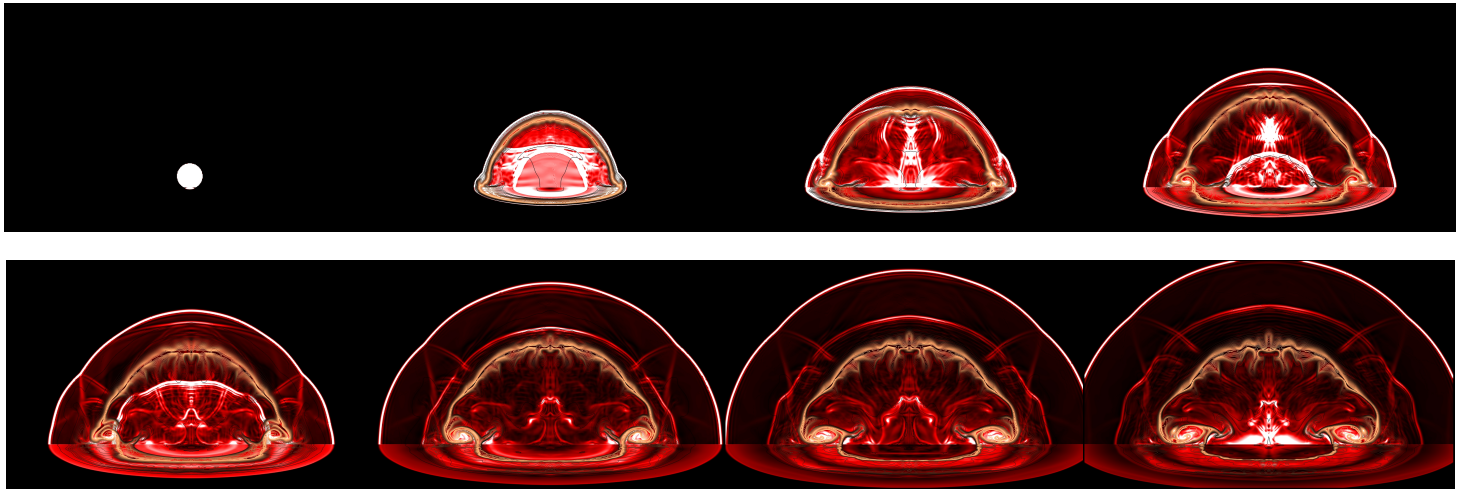

Figure 7.5: Case 3, TNT–HoB 0.2 m. Time series of simulation results in terms of red–white maps of λ_2 on which the contours of $\widetilde{Y_{CO_2}}$ in copper color at the centerplane are superimposed. Times are: top row 0 ms, 0.5 ms, 1 ms, 1.5 ms and the bottom row: 2 ms, 3 ms, 3.5 ms and 4 ms.

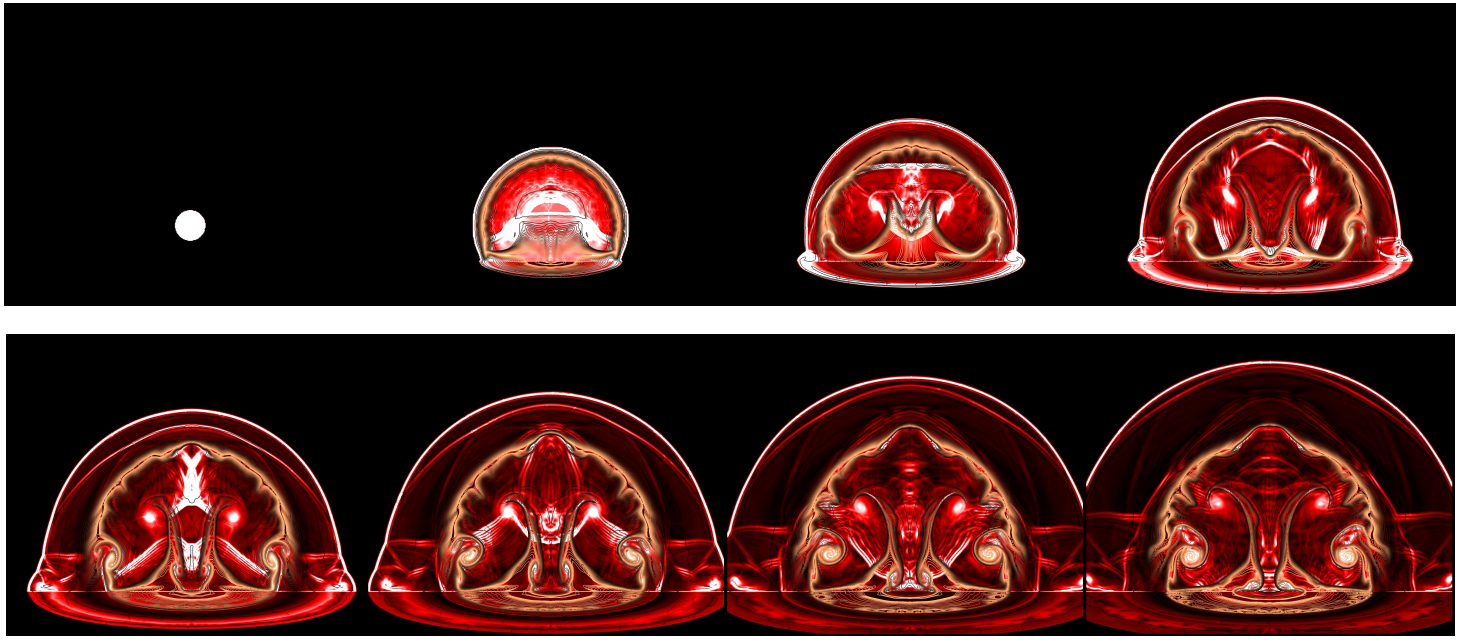

Figure 7.6: Case 4, TNT–HoB 0.5 m. Time series of simulation results in terms of red–white maps of λ_2 on which the contours of $\widetilde{Y_{CO_2}}$ in copper color at the centerplane are superimposed. Times are: top row 0 ms, 0.5 ms, 1 ms, 1.5 ms and the bottom row: 2 ms, 2.5 ms, 3 ms and 3.5 ms.

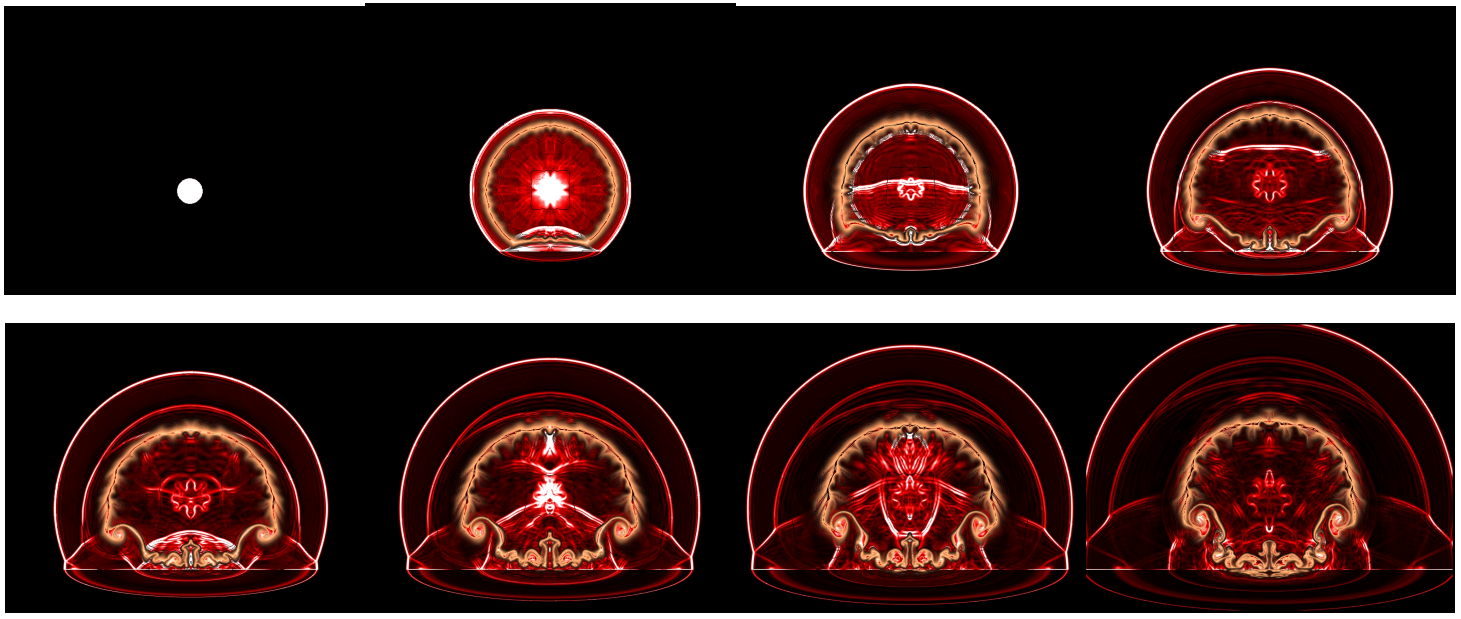

Figure 7.7: Case 5, TNT–HoB 1.0 m. Time series of simulation results in terms of red–white maps of λ_2 on which the contours of $\widetilde{Y_{CO_2}}$ in copper color at the centerplane are superimposed. Times are: top row 0 ms, 0.8 ms, 1.5 ms, 2 ms and the bottom row: 2.5 ms, 3 ms, 3.5 ms and 4.5 ms.

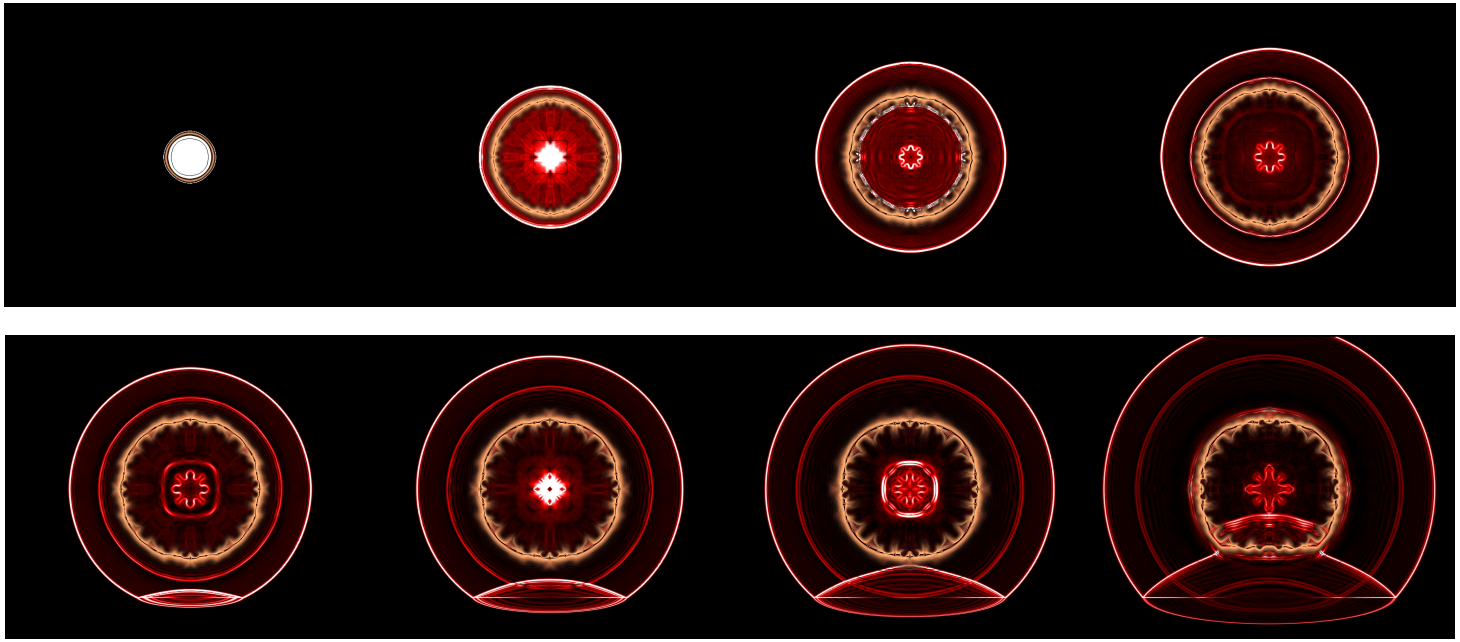

Figure 7.8: Case 6, TNT–HoB 2.0 m. Time series of simulation results in terms of red–white maps of λ_2 on which the contours of $\widetilde{Y_{CO_2}}$ in copper color at the centerplane are superimposed. Times are: top row 0 ms, 0.8 ms, 1.5 ms, 2 ms and the bottom row: 2.5 ms, 3 ms, 3.5 ms and 4.5 ms.

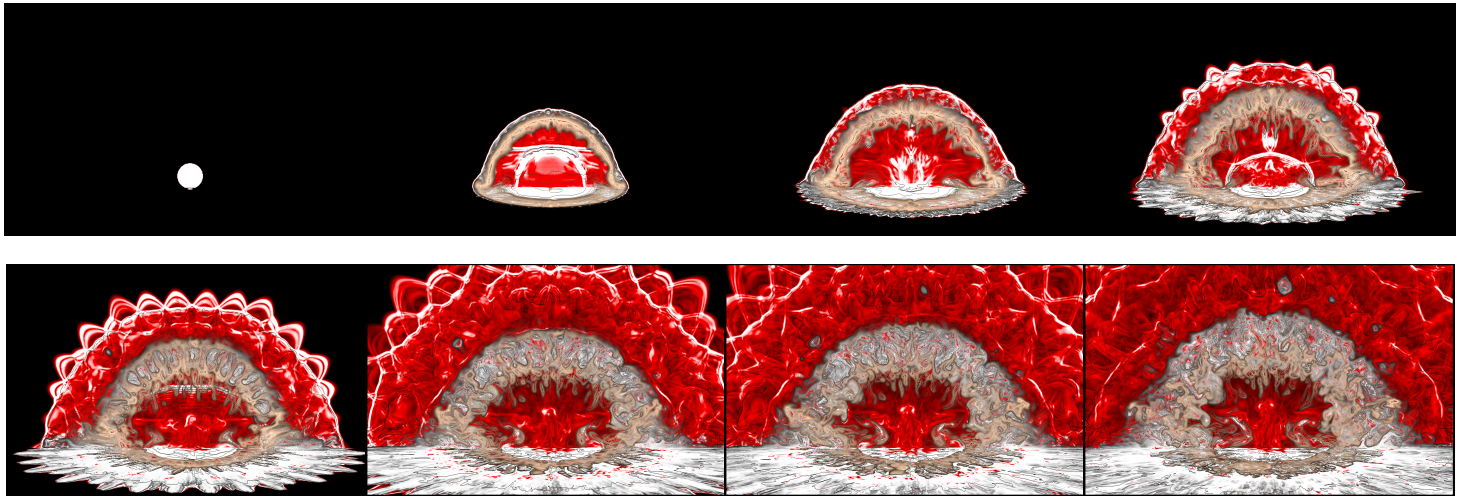

Figure 7.9: Case 7, TNT/Al–HoB 0.2 m. Time series of simulation results in terms of red–white maps of λ_2 on which the contours of $\widetilde{Y_{CO_2}}$ in copper color and contours of $\widetilde{Y_{Al_2O_3}}$ in grey color at the centerplane are superimposed. Times are: top row 0 ms, 0.5 ms, 1 ms, 1.5 ms and the bottom row: 2 ms, 3 ms, 3.5 ms and 4 ms.

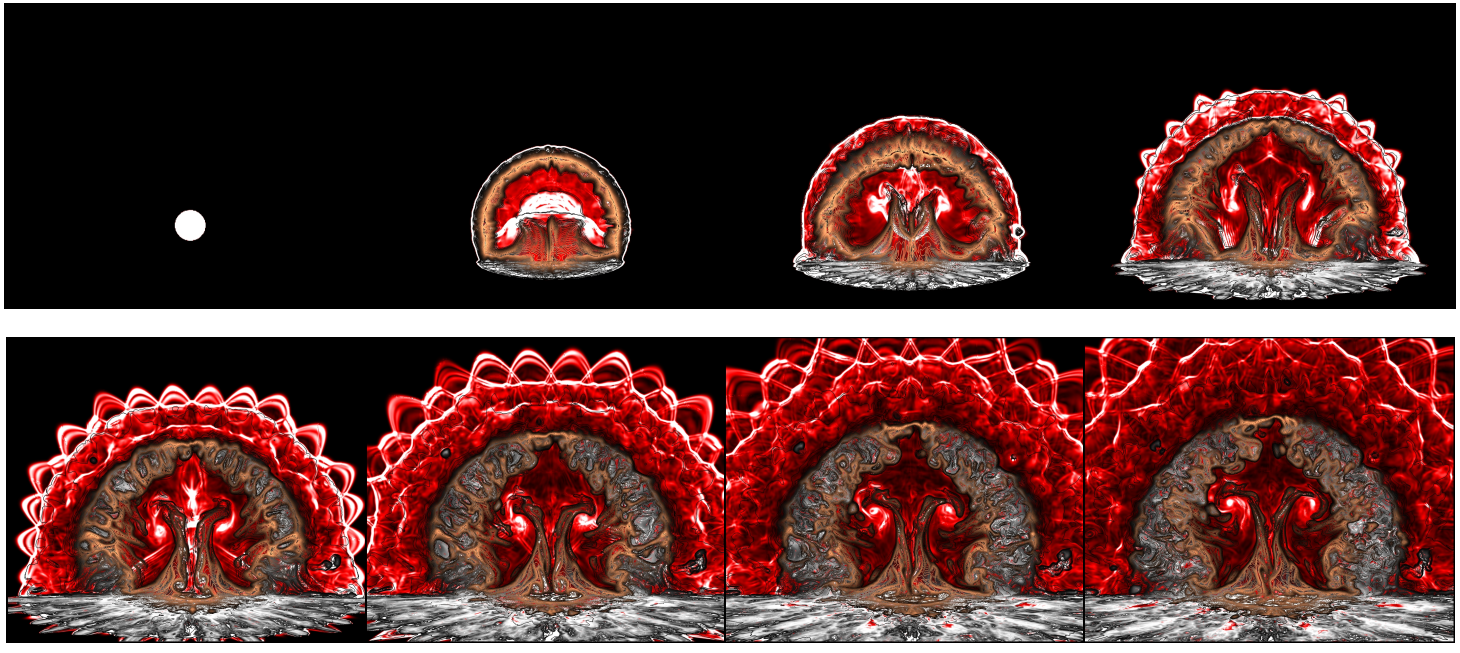

Figure 7.10: Case 8, TNT/Al–HoB 0.5 m. Time series of simulation results in terms of red–white maps of λ_2 on which the contours of $\widetilde{Y_{CO_2}}$ in copper color and contours of $\widetilde{Y_{Al_2O_3}}$ in grey color at the centerplane are superimposed. Times are: top row 0 ms, 0.5 ms, 1 ms, 1.5 ms and the bottom row: 2 ms, 2.5 ms, 3 ms and 3.5 ms.

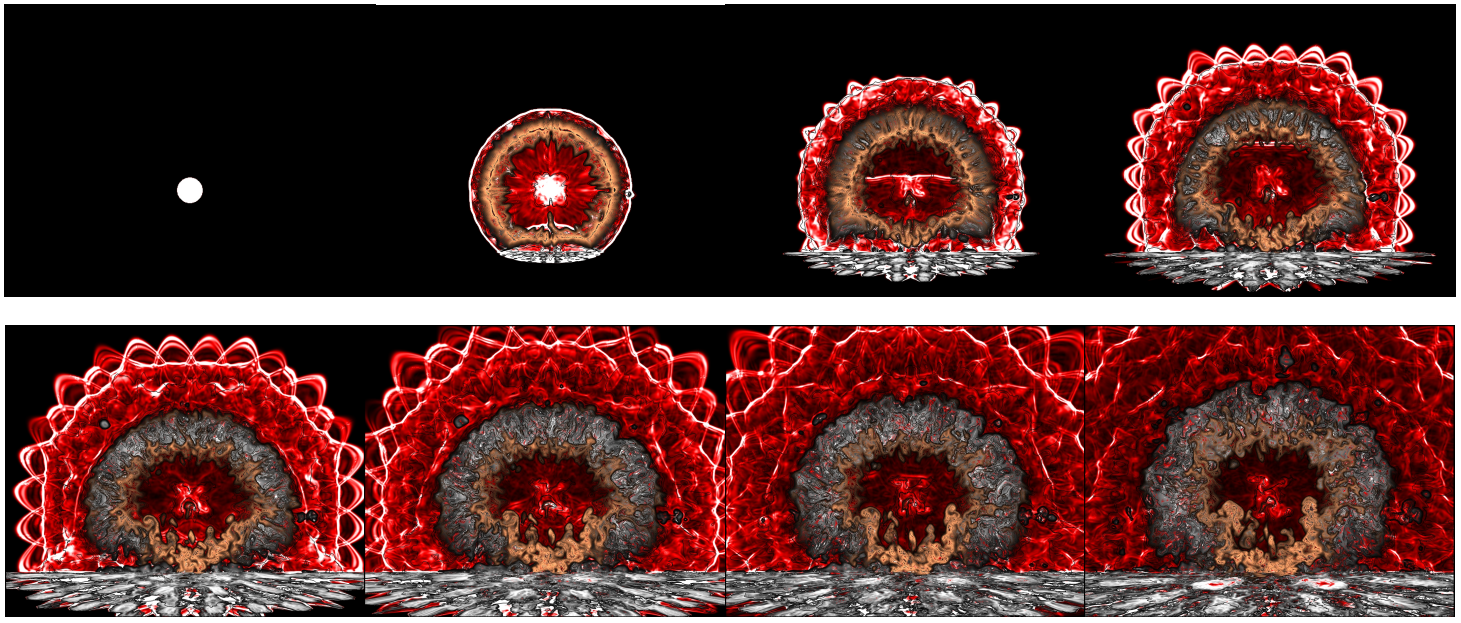

Figure 7.11: Case 9, TNT/Al–HoB 1.0 m. Time series of simulation results in terms of red–white maps of λ_2 on which the contours of $\widetilde{Y_{CO_2}}$ in copper color and contours of $\widetilde{Y_{Al_2O_3}}$ in grey color at the centerplane are superimposed. Times are: top row 0 ms, 0.8 ms, 1.5 ms, 2 ms and the bottom row: 2.5 ms, 3 ms, 3.5 ms and 4.5 ms.

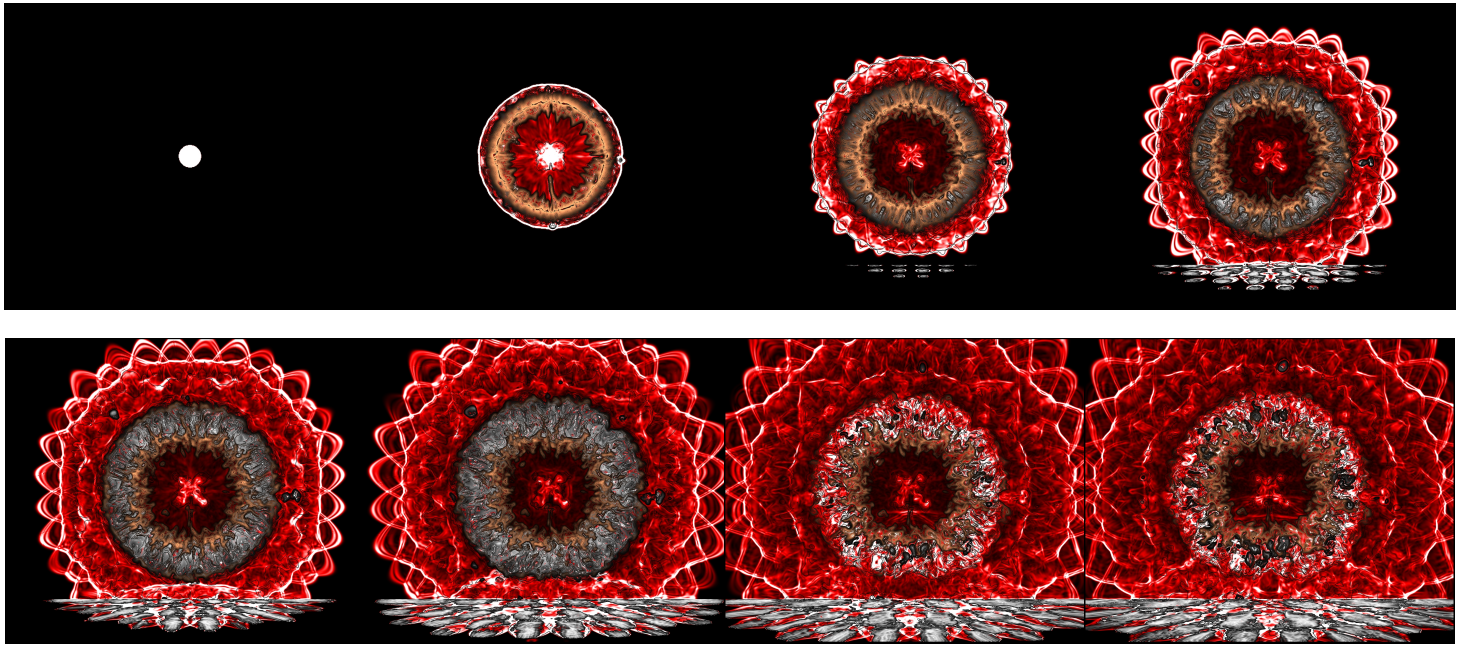

Figure 7.12: Case 10, TNT/Al–HoB 2.0 m. Time series of simulation results in terms of red–white maps of λ_2 on which the contours of $\widetilde{Y_{CO_2}}$ in copper color and contours of $\widetilde{Y_{Al_2O_3}}$ in grey color at the centerplane are superimposed. Times are: top row 0 ms, 0.8 ms, 1.5 ms, 2 ms and the bottom row: 2.5 ms, 3 ms, 3.5 ms and 4.5 ms.

mixing layer and giving rise to RT instabilities. Simultaneously, near ground level, high-density regions are formed due to collision. The ground reflected shock that collides with a rarefaction wave propagating inwards at $\sim$ 1.0 ms and creates two up- and down going shock waves, which elongate the mixing layer. At $\sim$ 1.5 ms the second collision with the ground occurs, the aftermath of which forms strong vorticity regions near ground as RM instabilities are developed, that is seen as two rings in the CO_2 contours at 1.5 ms. The new ground reflected shock travels upwards again, leaving low pressure regions behind it, which entrains more air into the mixing and afterburning regions. As the previous up- and downwashes of shock system meet again in the center of the domain, another shock gets sent towards the ground and the third ground collision occurs at $\sim$ 3.3 ms. In this system, the mixing layer does not get a chance to develop and thicken as the primary blast wave expands it sideways and the frequent traffic of the vertically moving shocks though it inhibit the growth of the instabilities, which are responsible for the mixing. Only large, energy dense, vortex structures survive the shock passages and hence the afterburning region remains thin.

Figure 7.6 shows the flow at a HoB of 0.5 m above ground. The initial blast wave expands outwards in the air as well as parallel to the ground. After the blast wave is reflected by the ground, at 0.5 ms it propagates inwards into the mixing layer, initially as two separate shocks, creating behind it a low pressure region that entrains air into the combustion zone. This effect is seen as a mushroom shape of an initially spherical fireball, visible, e.g., in the CO_2 contours at 1.0 ms. The ground reflected shocks collide (at 1.0 ms) with an ingoing rarefaction wave (the origin of which is seen in figure 2 at 0.5 ms) forming a complex mixing zone around the collision point. Two new shocks are formed, one propagating upwards and one downwards, towards the ground. These shock systems form strong up– and downwashes of the detonation products that enhance the mixing. Development of these is seen from 1.0 ms to 2.0 ms in the pressure distribution. These shock systems internally expand the afterburning region, primarily in the vertical direction, as can be seen at times 1.5–2 ms. Later, at 2.5–3 ms, they then internally contract both the mixing layer and the afterburning region, as they propagate towards each other and later collide.

In the HoB case of 1.0 m above ground, Fig. 7.7, the primary shock wave expands in all direction and the first ground collision occurs at $\sim$ 0.55 ms. While the ground reflected shock travels upwards, the rarefaction wave is propagating inwards, towards the origin, resulting in an implosion at $\sim$ 1 ms, seen in pressure distribution. This is the first case that exhibits both ground collisions and an implosion. This is also manifested in the mixing layer evolution as both the ground collision and the implosion entrain plenty of air into the mixing layer, combining this with RT instabilities growth just before and slightly after the implosion, creates a thick and vorticity rich afterburning region. The origin reflected shock and the ground reflected shock collide, and also in this case, create strong vertically moving shock systems and a complicated shock pattern. One of these shocks collides with the ground; again, at $\sim$ 2.5 ms. The mixing and the afterburning regions become trapped inside the origin reflected shocks and are only influenced by the ground reflected shock

propagations, thus imposing the most spherical mixing layer yet, where more instabilities are developed with each shock passage.

For the highest HoB of 2.0 m, Fig. 7.8, the flow and combustion follow the unconfined stages of an explosion even, described in in Chapter 2.1. The strong blast wave state is during 0 to ~ 1.5 ms, as the primary blast expands outwards, as a mixing layer is established at the core of the detonation. Implosion occurs at ~ 1.5 ms, after which the reshock face begins, and the mixing layer and combustion region are more fractured by the new vortical structures. The first ground reflection occurs at ~ 2.1 ms and the initial effects of this in the fireball are first seen ~ 4ms.

7.4 Heterogeneous Afterburning

Figures 7.9-7.12 present the heterogeneous counterpart cases for all HoB, cases 7-10, here also the grey–scale contours of the mass fraction of aluminium oxide, $\widetilde{Y_{Al_2O_3}}$ are included. The flow patterns are the same, however mixing and combustion are intensified. Also the effect of particle jetting is visible (cf. [23, 25, 28]), which might be attributed to the fact that it is computational particles, which diameters are scaled up (Eq. 4.1) that are causing such patters, since these are not clearly seen on the experimental videos.

To further investigate the influence of particle combustion on the afterburning, the following results are presented in terms of separate heat release contributions from carbon reactions and gaseous aluminium reactions, respectively. The heat release (cf. Eq. 7.1) contributions from carbon reactions, Q_{C} and aluminium reactions, Q_{Al} were then defined as follows

$$Q_{\mathrm{C}} = \sum_i \left(M_i P_{ij} \overline{\dot{w}_j} h^{\theta}_{f,i} \right) \quad \text{i = C, CO } CO_2\text{, j = 1,2 from Tab. 5.1}$$
$$Q_{\mathrm{Al}} = \sum_i \left(M_i P_{ij} \overline{\dot{w}_j} h^{\theta}_{f,i} \right) \quad \text{i = Al, AlO,}AlO_2\text{, }Al_2O_3\text{, O, j = 3–7 from Tab. 5.1.}$$

The heat release contributions in Figs. 7.13 and 7.14 are shown as spatial averages,($< Q_C >$ and $< Q_{\mathrm{Al}} >$) averaged over the area of the mixing layer. The mixing layer boundaries are determined by a condition on the Atwood number, $At < 0.9$, where At is the defined as $At = \frac{\rho_H - \rho_L}{\rho_H + \rho_L}$ in which ρ_H is the heavy fluid, i.e. the detonation/combustion products and ρ_L is the light fluid, i.e. the air. For $At > 0$ the turbulent mixing is considered unstable, the evolution of perturbations that are initiated as RT instabilities continues, [121].

Figure 7.13 shows $< Q_{\mathrm{C}} >$ and $< Q_{\mathrm{Al}} >$ for all three HoB, normalized by the maximum Q of all cases. The figure is presented in a semi–log form, to facilitate visualisation of all contributions of the heat release in the same plot. Figure 7.13 clearly displays that the heat release contribution from the aluminium reactions is significantly higher than from the carbon reactions, also $< Q_{\mathrm{Al}} >$ for all HoBs are more fluctuating in time compared to $< Q_C >$. Most of the heat release from carbon reactions seems to occur at early times, after which the afterburning of carbon stagnates at a steady pace, as is the case for homogeneous explosions. The heat release from aluminium reactions is more intermittent and is thought

to be closely connected to the physical environment inside the mixing layer, which, depending on the HoB is more or less governed by the shock wave passages through it.

In Fig. 7.14 the heat release contributions from carbon and aluminium reactions are

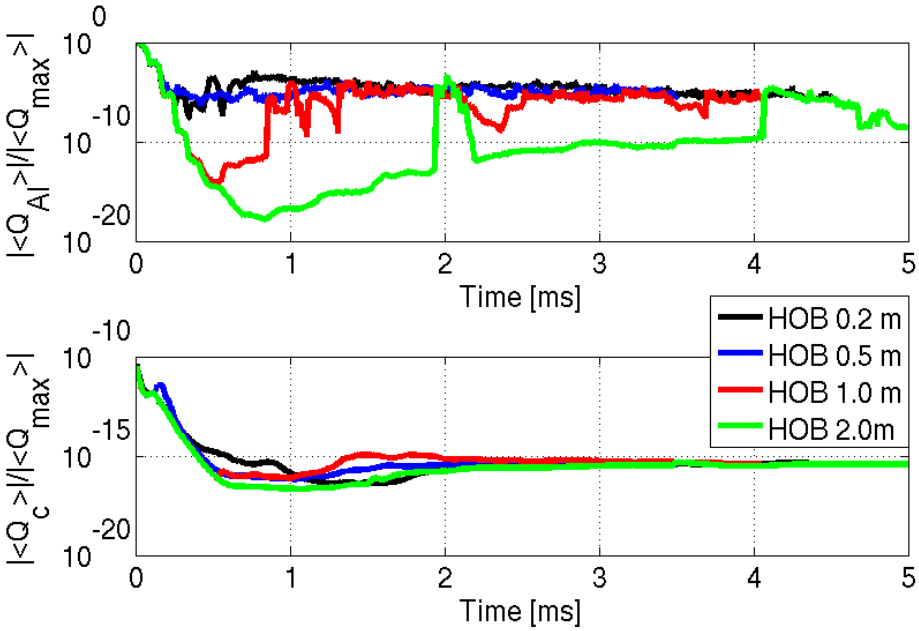

Figure 7.13: $< Q_{\mathrm{C}} >$ and $< Q_{\mathrm{Al}} >$ contributions for all HoBs.

compared to the pressure profiles, these profiles are extracted at the ground, beneath the detonation center and are meant to represent the shock wave passage through the mixing layer as the peaks in the pressure profiles indicate a ground reflection. Both the heat release contributions and the pressure profiles are plotted normalized by their respective maximum value in order to fit in the same graph. Figure 7.14 is plotted from time = 0.5 ms and onwards, excluding the effects of the main detonation and thereby focusing on the afterburning event.

Figures 7.14a and 7.14b show $< Q_C >$ and $< Q_{\mathrm{Al}} >$, respectively for HoB of 0.2 m. $< Q_C >$ shows little correlation with the shock passages, while $< Q_{\mathrm{Al}} >$ exhibits peaks related to the ground reflections, at 0.77 ms. For HoB of 0.5 m in Fig. 7.14c and 7.14d, for $< Q_C >$ and $< Q_{\mathrm{Al}} >$, respectively, the correlations between $< Q_{\mathrm{Al}} >$ and pressure is further certified in Fig. 7.14d as the peaks in $< Q_{\mathrm{Al}} >$ are occurring right before the peaks in the pressure trace. The small peak in $< Q_{\mathrm{Al}} >$ at 0.77 ms is attributed to a shock merge (as also shown in Fig. 7.10) and the largest peaks at 1.24 and 1.35 ms occur as the shock is reflected from the ground and travels upwards, into the mixing layer. Regarding $< Q_C >$ in Fig. 7.14c, the peak heat release from carbon reactions does increase after

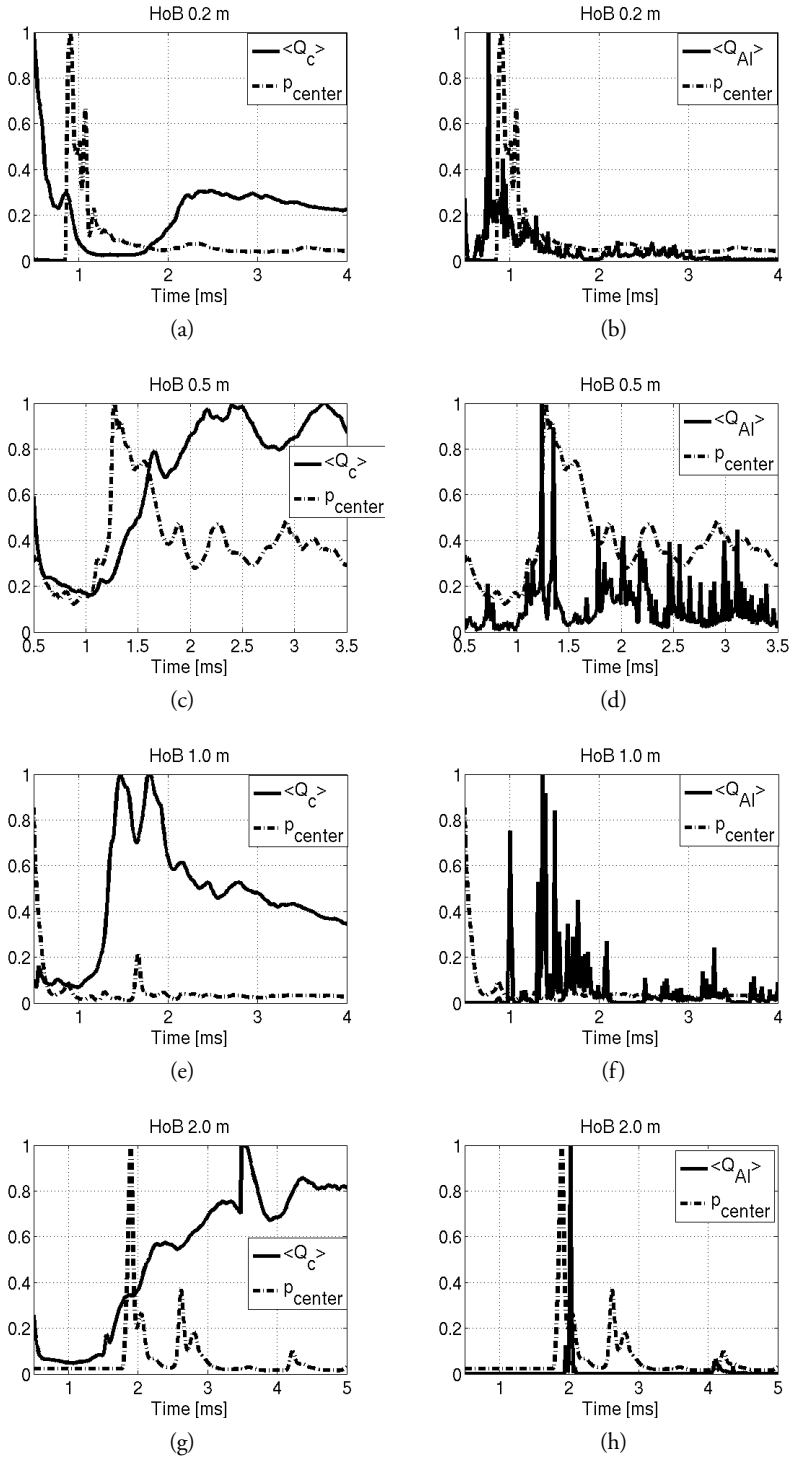

Figure 7.14: Averaged heat release contributions compared pressure profiles at ground under the center of detonation.

the ground reflection, as new air is entrained into the mixing layer, however the following variation in $< Q_C >$ are smaller and much less frequent compared to $< Q_{\mathrm{Al}} >$. The highest HoB cases of 1.0 and 2.0 m, in Fig. 7.14e and 7.14f, and 7.14g and 7.14h, exhibit both ground collisions and an implosion, (cf. Fig. 7.11 and Fig. 7.12). The mixing and the afterburning regions become trapped inside the origin-reflected shocks and are only slightly influenced by the ground reflected shock propagations, thus imposing more pronounced spherical mixing layers compared to the lower HoB cases. Considering Figure Fig. 7.14e and Fig. 7.14f, from HoB 1.0 m, one clear peak in pressure profile is shown, as the ground reflection occurs at $\sim$1.7 ms, before and after which $< Q_C >$ is at its highest values. Regarding $< Q_{\mathrm{Al}} >$, it is visible that $< Q_{\mathrm{Al}} >$ is more dependent on the physics in the mixing layer as the peaks in $< Q_{\mathrm{Al}} >$ at 1 ms, right after the implosion, around 1.7 ms and afterwards, as the reflected shock propagates through the mixing layer. For the HoB of 2.0 m in Figure 3 7.14 and 3 7.14, three distinct peaks are present in the pressure profile, to the first of which $< Q_{\mathrm{Al}} >$ responds immediately, while $< Q_C >$ shows a slower increase and seems again to develop at different time scale compared to $< Q_{\mathrm{Al}} >$.

Figure 7.14 indicates that $< Q_{\mathrm{Al}} >$ is dependent on the mixing intensity, which is established by RT and RM instabilities through shock–mixing layer (i.e. density variations) interaction. Mixing intensity in its turn varies with HoB, as the shock propagation pattern is different for all HoB, which means that in order to achieve maximum effect from aluminium inclusion to an explosive, HoB must be considered as a parameter. The HoB of 0.2 m does not seem as effective from an afterburning point of view as the HoB of 0.5 m for this charge and weight.

Figure 7.15 visualises the flow, in terms of temperature field, and the afterburning in terms of Q_{C} and Q_{Al} for HoB of 0.2 m (first row), 0.5 m (second row), 1.0 m (third row) and 2.0 m (bottom row) at times 0.77 and 0.95 ms, 0.72 and 1.3 ms, 1.01 and 1.37 ms, and 2 and 2.6 ms, respectively for each case. These times correspond to the strongest peaks in the $< Q_{\mathrm{Al}} >$ profiles in Fig. 7.14. The aluminium combustion seems to occur in fine vorticity structures around the carbon combustion, as both reactions are dependent on oxygen and thus mixing to continue to react. Particle inclusion creates these fine vorticity structures, by initiating perturbations at the interface between the detonation products and air and thereby inducing more RT and consequently RM instabilities. The results of these perturbations are visible as both quire wrinkled Q_{Al} and the chequered pressure pattern behind the primary shock, induced when the particles overtake the shock and perturb its surface. The fine vorticity structures, together with the exothermic aluminium oxide reactions that enable volumetric expansion, lead to a prolonged afterburning effect.

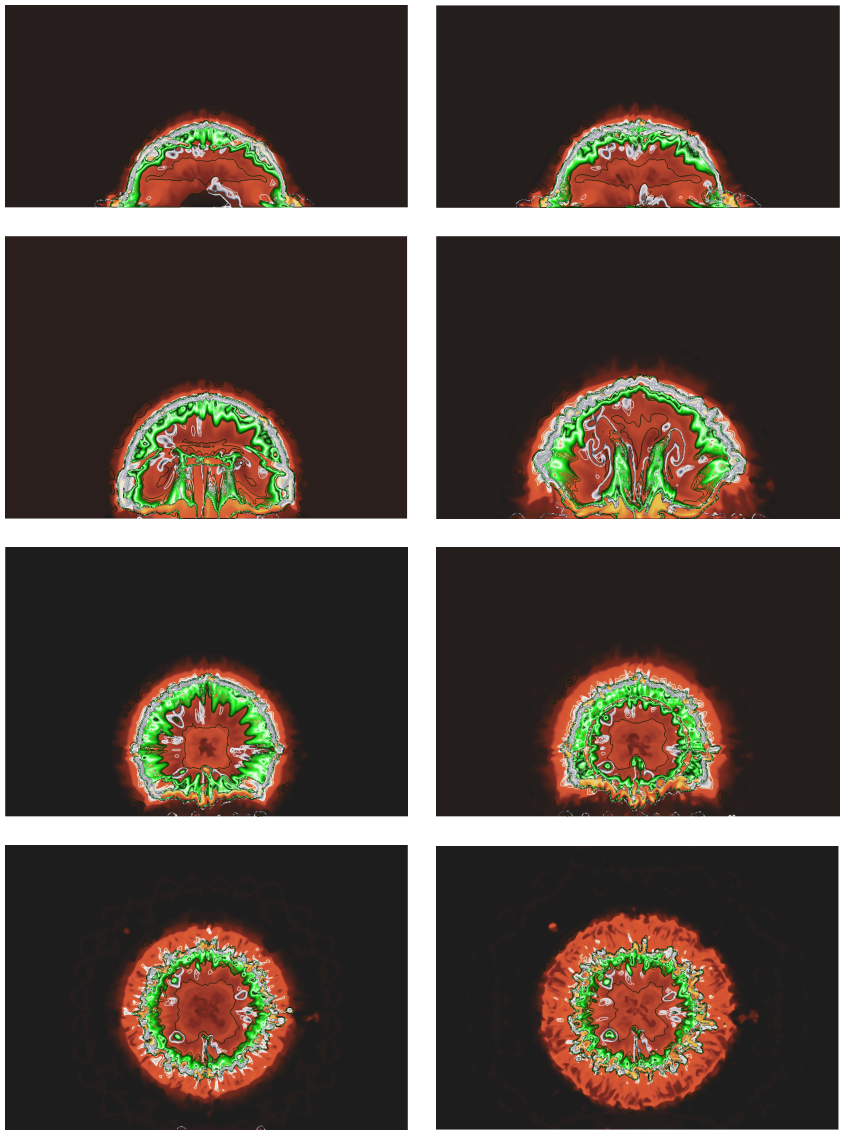

Figure 7.15: Visualisation for the flow and afterburning in terms of temperature, Q_{C} (green) and Q_{Al} (grey) at the centerline all for HoB from top to bottom at times 0.77 and 0.95 ms; 0.72 and 1.3 ms; 1.01 and 1.37 ms; and 2 ms and 2.6 ms; respectively for each case.

7.5 Comparison to Experimental Data

In this section the comparisons of simulation results with the previously described experimental data are presented starting with the pressure data for pressure probe P1 in Fig. 7.16 and comparisons with the film analysis data in Fig. 7.17 (initially presented in Chapter 6). Figure 7.16 shows pressure traces from the simulations and the experiments for all cases. The experimental pressure traces are shown with small errorbars to account for the differences in air pressure, temperature and humidity between the simulations and the experiments. The best agreement is achieved for the HoB 0.2 and 0.5 m, with cases 3 and 4 having the best agreement with experiments regarding both the arrival time of the shock wave and its magnitude. Cases 8 and 9, containing aluminium overpredict the pressure magnitude, and in the case of case 9, substantially, with the pressure magnitude overpredicted by a factor of 5. Simulation results for case 5, show the worst agreement with the experimental data, with the overprediction of the arrival time and the underprediction of the pressure magnitude. Comparison to HoB 2m is omitted, due to incomplete simulation data at P1 location.

Figure 7.17 present qualitative validation of the afterburning properties in terms of comparison of RA and RI that were obtained from film analysis (in Sec. 6.2) to the simulation results in terms of averaged area of the mixing layer (is compared to RA) and averaged temperature[4] in the mixing layer (compared to RI). In other words, the RA and RI from Figs. 6.9b and 6.8b, respectively, are compared to area and temperature[4], obtained in the simulations, respectively. Since the experimental variable are normalized with the maximum value among all cases and the simulation values are normalized with the maximum value among all simulated cases the comparisons can only be qualitative, thus only common trends can be considered.

These trends are that for pure TNT cases (cases 3-6), Fig. 7.17a,c,e,g, the RA and RI in the experiments have the same shape for each HoB, respectively, ending up at almost constant profile after $\sim$ 1 ms. The simulations appear to mimic this behaviour well, however with different values. TNT/Al cases (7-10), Fig. 7.17b,d,f,h display a general increase in RA with time and an almost stagnation of RI after $\sim$ 1 ms with small variations. These results, together with the comparisons to pressure traces indicate that the simulations results show the good overall predictive capabilities, considering the great number of complicated physical processes involved in the afterburning behind condensed phased explosions that are being modelled.

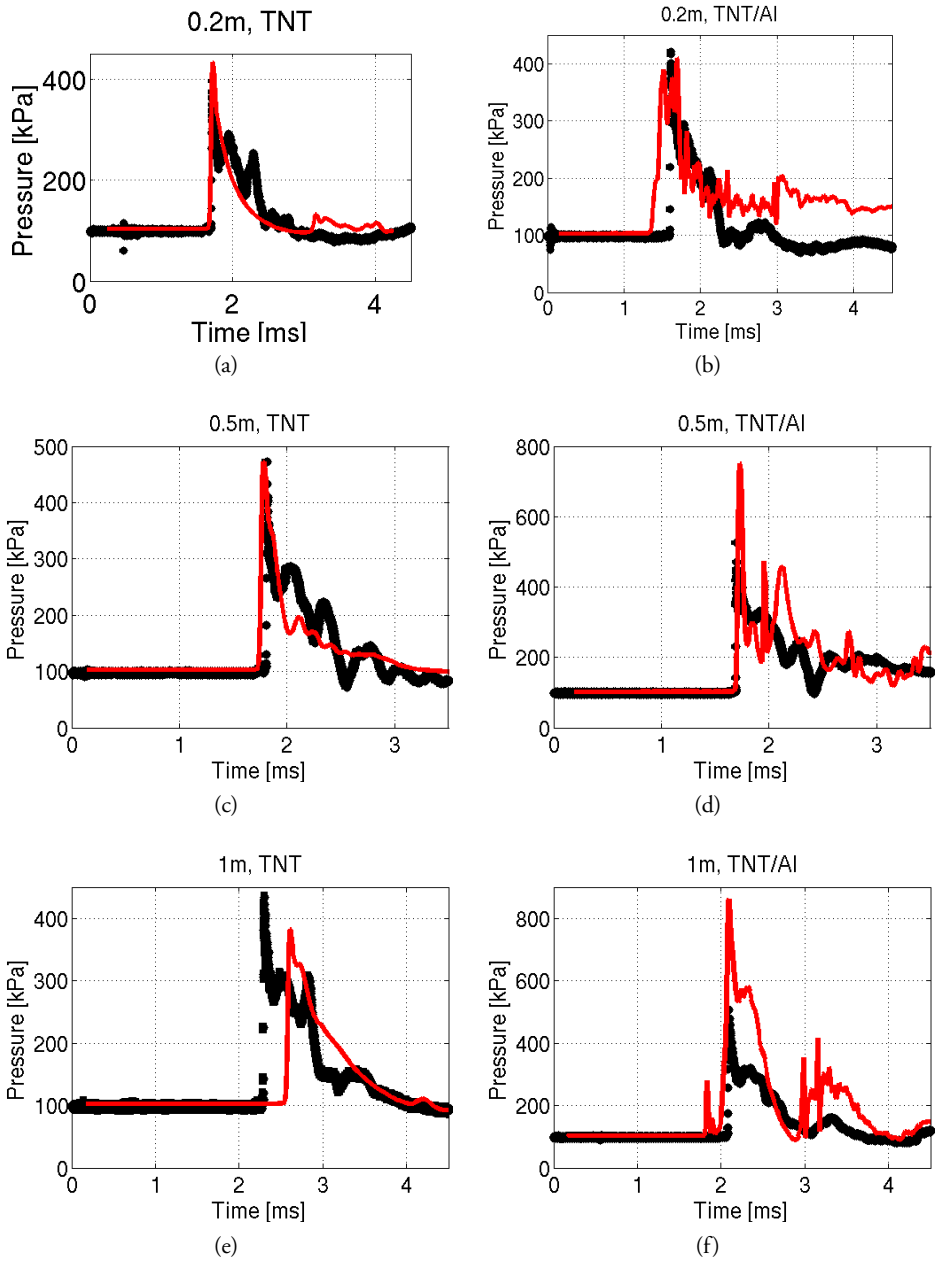

Figure 7.16: Comparisons with experimental pressure measurements at P1 for (a) TNT–HoB 0.2 m, (b) TNT/Al–HoB 0.2 m, (c) TNT–HoB 0.5 m, (d) TNT/Al–HoB 0.5 m, (e) TNT–HoB 1.0 m and (f) TNT/Al–HoB 1.0 m. Legend: (–) simulations, (⊢⊣) experiments.

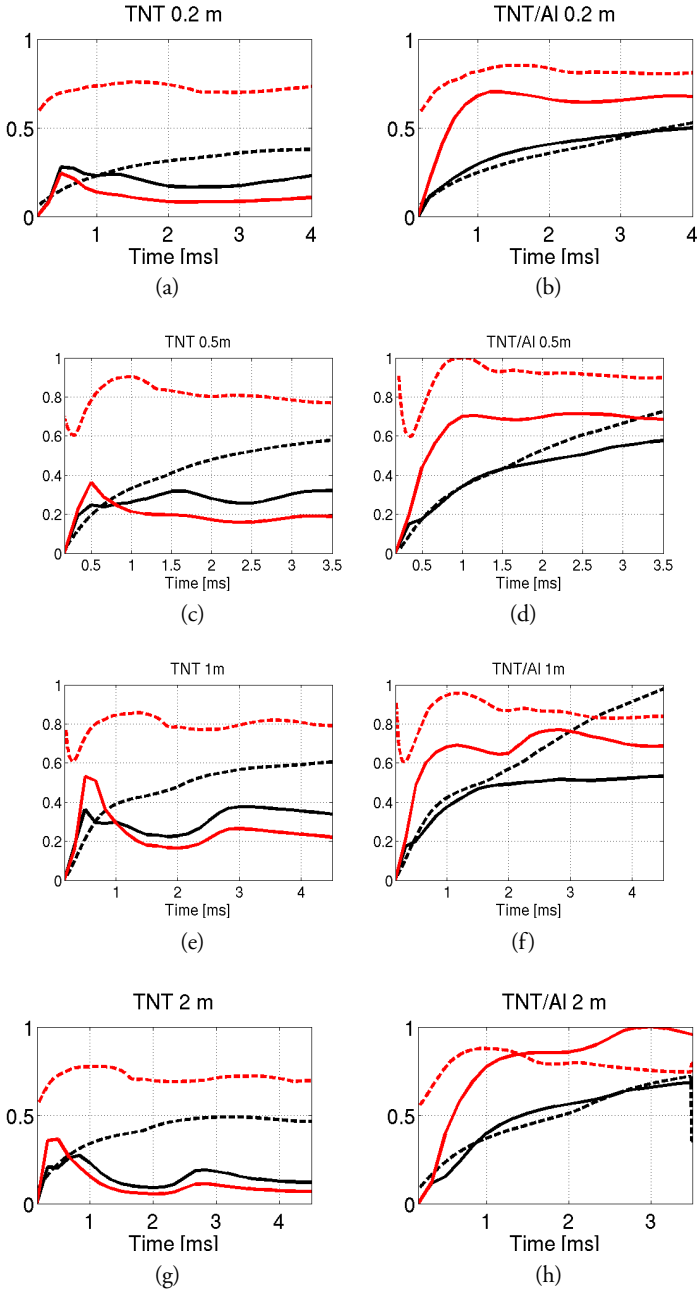

Figure 7.17: Comparisons with film analysis data for relative intensity and relative area of the mixing layer (a) TNT–HoB 0.2 m, (b) TNT/Al–HoB 0.2 m, (c) TNT–HoB 0.5 m, (d) TNT/Al–HoB 0.5 m, (e) TNT–HoB 1.0 m, (f) TNT/Al–HoB 1.0 m, (g) TNT–HoB 2.0 m and (h) TNT/Al–HoB 2.0 m. Legend: (–) RA, (–) RI, (– –) averaged area of the mixing layer (simulations), (– –) averaged temperature of the mixing layer (simulations).

Chapter 8

Concluding Remarks

Post-detonation flow and the afterburning of high explosive were simulated using a two–phase LES model in Euler–Lagrange form, with a two–way coupling between phases and finite rate Arrhenius chemistry. The model has been implemented in OpenFOAM 1.6.x and mainly 8 different cases have been investigated, 1 kg of TNT and 1 kg of TNT/Al at HoB of 0.2 m, 0.5 m, 1.0 m and 2.0 m. The simulations were conducted using LES-PaSR with ILES subgrid model. To validate the model, an experimental campaign was conducted. The simulations results showed the good overall predictive capabilities, considering the great number of complicated physical processes involved in the post-detonation afterburning that are being modelled.

The most important findings from this work, based on experience of analysing cases in Tab. 7.1, can be summarized as:

1. The heat release and thereby combustion take place around the vorticity filaments, generated by RT and RM instabilities, hence predicting the position of post-detonation afterburning. (Paper I and II)

2. All HoBs exhibited common flow features, such as shock-turbulent mixing layer interaction, the rise of RT and RM instabilities and the ground reflected shocks affecting the mixing layer dynamics. (Paper III)

3. In order to achieve maximum effect of the afterburning during an explosive blast, the turbulent mixing layer, which has to contain enough vorticity structures to support semi-stable mixing, has to be combined with frequent shock propagation through it, thereby sustaining the duration of the afterburning. (Paper III and IV)

4. The main mechanism responsible for the mixing, and therefore afterburning, is the rise of RT instabilities, which trigger the build up of a mixing layer. Shock-mixing layer interaction the creates RM instabilities, these arise and generate vorticity through baroclinic effects. The presence of particles increases the vorticity generated

by RT and RM instabilities since the particles create perturbations in the detonation product cloud, hence disrupting the alignment of the pressure and density gradients. Burning particles improve the mixing even further through volumetric expansion induced by increased heat release from particle combustion. (Paper IV)

5. The results indicate that Al afterburning in heterogeneous charges is dependent on the mixing intensity, which is established by RT and RM instabilities through shock–mixing layer (i.e. density variations) interaction. Mixing intensity in its turn varies with HoB, as the shock propagation pattern is different for all HoB, which means that in order to achieve maximum effect from aluminium inclusion to an explosive, HoB must be considered as a parameter. (Paper V)

8.1 Outlook

Further research in Al afterburning is required since the simulation results presented here are only as valid as the reaction mechanism for the $C - O_2$ and $Al - O_2$ combustion. Incorporating carbon as solid particles (instead of gaseous specie) and extending its reaction mechanism would provide additional knowledge regarding the physics of afterburning of EBX charges. Also, other weights, formulations and HoBs should be simulated to properly investigate the effect of HoB on the afterburning. This is however not a trivial nor cheap task and for the time being the presented work does demonstrate the possibilities of computational simulations and how these can aid with the background data to be incorporated in the design and optimization processes for EBX charges.

As a first step to continuation of this work and an inspiration to others, a TNT/Al case at HoB of 0.5 m (case 8, Tab. 7.1) has been resimulated using an extended Al-oxidation mechanism, featured in Tab. 8.1. Here, two new reactions are added (A6 and A7), enabling anaerobic afterburning of Al, as these two reactions are crucial for afterburning in confined space and in underwater explosions. The preliminary results from this case are shown in Fig. 8.1 with the 'old' mechanism (Tab. 5.1) on the left and the 'new' mechanism (Tab. 8.1) on the right. The bottom frames in Fig. 8.1 are visually comparable to Fig. 8.2. The pressure profiles from P1 are shown in Fig. 8.3.

Conclusions from this preliminary attempt to improve current Al-combustion mechanism are that inclusion of reactions (A6) and (A7) has improved the pressure prediction compared to experimental data. Also the combustion region is seemed more perturbed and small scale vortical structures have increased. However, combustion region (area of the fireball) is smaller for 'new' mechanism compared to old one, which is inconsistent with the snapshots for the video of the experiments and figures similar to Fig. 7.17 (not shown). This begs the questions (i) Al-combustion pathways: Al-O_2, Al-CO_2, Al-H_2O, which are preferred and under which conditions, (ii) what would results for another HoB show, (iii) are the rates in Tab. 8.1 correct or should be 'tailored' for this application, (iv) etc.?

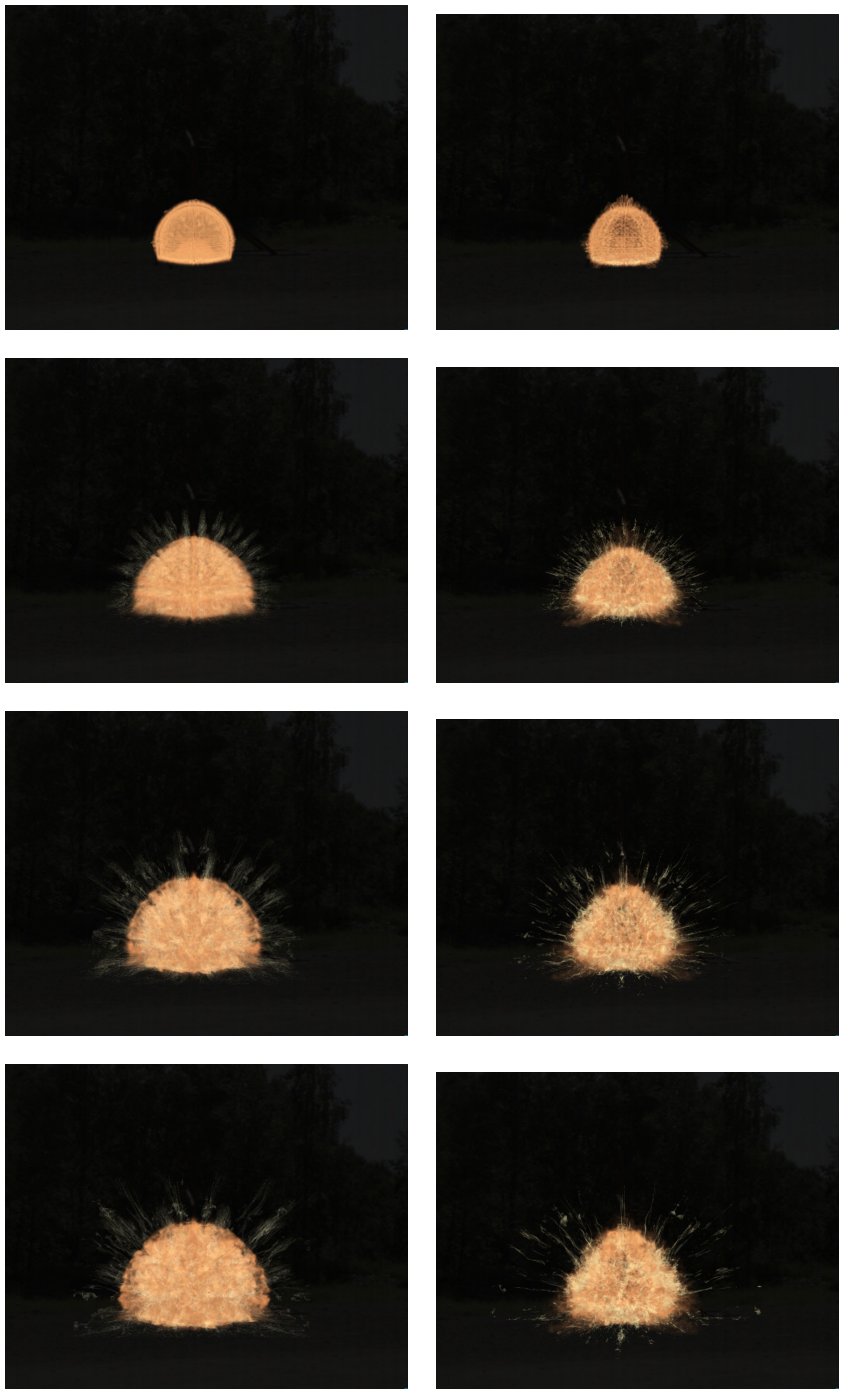

Figure 8.1: Simulation results for 'old' Al-combustion mechanism (left) and 'new' combustion mechanism, (right). Featured in terms of volume renderings of mass fraction of Al_2O_3 white-yellow and CO_2 in copper. Time series from top to bottom: 0.5, 1.5, 2.5 and 3 ms.

Figure 8.2: Snapshot of a video from a TNT/Al HoB 0.5 m case at $\sim$ 3 ms.

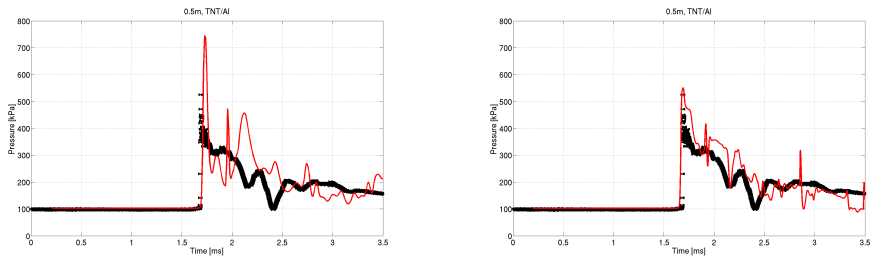

(a) (b)

Figure 8.3: Comparing pressure profiles at P1 for (a) 'old' Al-combustion mechanism (left) and (b) 'new' combustion mechanism.

Table 8.1: Rate parameters for $C-O_2$ and $Al-O_2-H_2O-CO_2$ reaction mechanisms.

No.	Reaction	A[m, kg, mol, s, K]	m	T_a[K]	Reference
C1	$C + \frac{1}{2}O_2 \rightarrow CO$	$4.84 \cdot 10^{11}$	0	5000	[110]
C2	$CO + \frac{1}{2}O_2 \rightarrow CO_2$	$6.29 \cdot 10^{12}$	0	8000	[110]
A1	$Al_{(g)} + O_2 \rightarrow AlO + O$	$1.13 \cdot 10^{11}$	0	80	[93]
A2.	$AlO + O_2 \rightarrow AlO_2 + O$	$3.36 \cdot 10^{11}$	0	10008	[93]
A3	$AlO_2 \rightarrow AlO + O$	$5.08 \cdot 10^{10}$	0	48312	[95]
A4.	$O + O + M \rightarrow O_2 + M$	$2.41 \cdot 10^{13}$	-0.5	0	[93]
A5	$2AlO + \frac{1}{2}O_2 \rightarrow Al_2O_3$	$7.27 \cdot 10^{22}$	0	0	[95]
A6.	$Al + CO_2 \rightarrow AlO + CO$	$1.74 \cdot 10^{8}$	0	3221	[116]
A7.	$Al + H_2O \rightarrow AlO + H_2$	$9.6 \cdot 10^{8}$	0	2869	[116]

These preliminary results prove to show that much work remains to be done in attaining the understanding regarding post-detonation afterburning. Following suggestion are noted in order to further improve the current two–phase afterburning model, its predictions and also gain more knowledge in these processes.

- Simulate several more HoB with new mechanism;
- Deeper investigation in Al-combustion kinetics, seeking mechanism improvements and understanding;
- Initialization of aluminium in the domain, investigate the effect of starting the simulation with non-zero initial values for mass fractions of aluminium oxides;
- Inclusion of particle size distribution (both in the domain and inside a computational particle);
- Inclusion of models for aluminium oxide condensation and dissociation together with oxide cap formation;
- Inclusion of carbon as particles;
- More detailed chemical–kinetics for carbon combustion;
- Investigate the effect of non–spherical particles and different distribution of particles in the explosive compound and how that affects the afterburning.

Bibliography

[1] G.I. Taylor. The instability of liquid surfaces when accelerated in a direction perpendicular to their planes. *Proc. of Royal Society of London. Series A*, 201:192–196, 1950.

[2] R.D. Richtmyer. Taylor instability in a shock acceleration of compressible fluids. *Com. Pure and Appl. Math.*, 13:297–319, 1960.

[3] OpenFOAM. www.openfoam.org, 2009.

[4] H.G. Weller, G. Tabor, H. Jasak, and C. Fureby. A tensorial approach to CFD using object oriented techniques. *Comp. in Physics*, 12:620–632, 1997.

[5] A.L. Kuhl. *Dynamics of Exothermicity*, chapter Spherical Mixing Layers in explosions, pages 290–320. Gordon and Breach, Longhorn, 1996.

[6] A.L. Kuhl, R.E. Fergusson, and A.K. Oppenheim. Gasdynamic model of turbulent exothermic fields in explosions. *Prog. in Astronautics and Aeronautics*, 173:251–261, 1997.

[7] A.L. Kuhl, R.E. Fergusson, and A.K. Oppenheim. Gasdynamics of combustion of TNT products in air. *Archivum Combustionis*, 19:67–89, 1999.

[8] A.L. Kuhl, A.K. Oppenheim, R.E. Fergusson, H. Reichenbach, and P. Neuwald. Effects of confinement on combustion of TNT explosion products in air. *28th International Symposium on Combustion, July 30 – August 4*, 2000.

[9] P. Neuwald, H. Reichenbach, and A.L. Kuhl. Shock–dispersed–fuel charges–combustion in chambers and tunnels. *34st International ICT Conference: Energetic Materials: Reactions of Propellants, Explosives and Pyrotechnics, June 24–27*, 2003.

[10] A.L. Kuhl and B. Khasainov. Quadratic model of thermodynamic states in SDF explosions. *38th ICT Conference*, 2007.

[11] A.L. Kuhl and H. Reichenbach. Combustion effects in confined explosions. *Proc. Comb. Inst.*, 32:2291–2298, 2009.

[12] A.L. Kuhl, J.B. Bell, V.E. Beckner, and B. Khasainov. Simulations of turbulent combustion fields of shock–dispersed aluminum using the AMR code. *41st Combustion Subcomittee/29th Airbreathing Propulsion Subcomittee and 23rd Propulsion Hazards System Subcomittee*, 2006.

[13] J.B. Bell, V.E. Beckner, and A.L. Kuhl. Simulation of enhanced–explosive devices in chambers and tunnels. *HPCMP Users Group Conference, IEEE*, 2007.

[14] A.L. Kuhl, J.B. Bell, V.E. Beckner, and B. Khasainov. Simulation of aluminum combustion and PETN afterburning in confined explosions. *21st International Colloquim on the Dynamics of Explosions and Reactive Systems (ICDERS), July 23–27, Poitiers, France*, 2007.

[15] A.L. Kuhl, B. Khasainov, and J.B. Bell. Two–phase model of combustion in explosions. *37th International Annual Conference of ICT, June 27–30*, 2006.

[16] B. Khasainov, A.L. Kuhl, S.B. Victorov, and P. Neuwald. Model of non–premixed combustion of aluminum–air mixtures. *Shock Compression of Condensed Matter*, pages 449–452, 2005.

[17] A.L. Kuhl, M. Howard, and L. Fried. Thermodynamic model of afterburning in explosions. *34th International ICT Conference: Energetic Materials: Reactions of Propellants, Explosives and Pyrotechnics, June 24–27, Karlsruhe, Germany*, 2003.

[18] A.L. Kuhl, A.K. Oppenheim R.E. Ferguson, and M.R. Seizew. Visualisation of mixing and combustion of TNT explosions. *Extreme States of Substance Detonation Shock Waves, February 26 – March 3, Sarov, Nizhni Novgorod Region, Russia*, 2001.

[19] A.L. Kuhl, J.B. Bell, and V.E. Becker. Heterogeneous continuum model of aluminum particle combustion in explosions. *Comb. Explosion and Shock Waves*, 46:433–448, 2010.

[20] A.L. Kuhl, J.B. Bell, V.E. Becker, K. Balakrishnan, and A.J. Aspden. Spherical combustion clouds in explosions. *Shock Waves*, 23:233–249, 2013.

[21] K. Balakrishnan, A.L. Kuhl, J.B. Bell, and V.E. Beckner. An empirical model for the ignition of explosively dispersed aluminium particle clouds. *Shock Waves*, 22:591–603, 2012.

[22] D.L. Frost, F. Zhang, S.B. Murrey, and S. McCahan. Critical condition for ignnition of metal particles in a condensed explosives. In *Detanation Symposia*, 2002.

[23] D.L. Frost and F. Zhang. The nature of heterogeneous blast explosives. In *Proc. 19th Military Aspects of Blast and Shock, Calgary, Canada*, 2006.

[24] D. Ritzel, R. Ripley, S. Murray, and J. Anderson. *Shock Waves*, chapter Near-field blast phenomenology of thermobaric explosions. Springer, 2009.

[25] R.C. Ripley, L. Donahue, T.E. Dunbar, S.B. Murray, C.J. Anderson, F. Zhang, and D.V. Ritzel. Ground reflection interaction with heigh-of-burst metalized explosions. In *26th International Symposium on Shock Waves*, 2009.

[26] L. Donahue, F. Zhang, and R.C. Ripley. Numerical models for afterburning of tnt detonation products in air. *Shock Waves*, 23:559–573, 2013.

[27] Z. Zarei and D.L. Frost. Simplified modeling of blast waves from metalized heterogeneous explosives. *Shock Waves*, 21:425–438, 2011.

[28] F. Zhang, R.C. Ripley, A. Yoshinaka, C.R. Findlay, J. Anderson, and B. von Rosen. Large-scale spray detonation and related particle jetting instability phenomenon. *Shock Waves*, 25:239–254, 2015.

[29] F. Zhang, J. Anderson, and A. Yoshinaka. Post-detonation energy release from tnt-aluminum explosives. In *Shock Compression of Condensed Matter*, 2007.

[30] F. Zhang, S.B. Murray, and K.B. Gerrard. Aluminum particles-air detonation at elevated pressures. *Shock Waves*, 15:313–324, 2006.

[31] R.C. Ripley, L. Donahue, and F. Zhang. Fragmentation of metal particles during heterogeneous explosions. *Shock Waves*, 25:151–167, 2015.

[32] F. Zhang, D.L. Frost, P.A. Thibault, and S.B. Murray. Explosive dispersal of solid particles. *Shock Waves*, 10:431–443, 2001.

[33] D.L. Frost, C. Ornthanalai, and Z. Zarei. Particle momentum effects from detonation of heterogeneous explosives. *J. App. Phys.*, 101:113529, 2007.

[34] F. Zhang. Metalized heterogeneous detonation and dense reactive particle flow. In *AIP Conferense Proceedings*, volume 1426, pages 27–34, 2014.

[35] D.L. Frost, Z. Zarei, and F. Zhang. Instability of combustion products interface from detonation of heterogeneous explosives. In *20th International Colloquium on the Dynamics of Explosions and Reactive Systems, Montreal, Canada*, 2005.

[36] K. Balakrishnan and S. Menon. A numerical investigation of shear instability, mixing and afterburn behind explosive blast waves. *47th AIAA Aerospace Sciences Meeting, 5–8, January, Orlando, USA, AIAA–2009–1530*, 2009.

[37] K. Balakrishnan, D.V. Nance, and S. Menon. Simulation of impulse effect from explosive charges containing metal particles. *Shock Waves*, 20:217–239, 2010.

[38] K. Balakrishnan, F. Genin, D.V. Nance, and S. Menon. Numerical study of blast characteristics from detonation of homogeneous explosives. *Shock Waves*, 20:147–162, 2010.

[39] K. Balakrishnan and S. Menon. On the role of ambient reactive particles in the mixing and afterburning behind explosive blast waves. *Comb. Sci. & Techn.*, 182:186–214, 2010.

[40] K. Balakrishnan and S. Menon. On turbulent chemical explosions into dilute aluminum particle clouds. *Comb. Theory & Model.*, 14:583–617, 2010.

[41] K. Balakrishnan and S. Menon. Characterisation of the mixing layer resultning from detonations of hetergeneous explosive charges. *Flow, Turb. & Comb.*, 87:639–671, 2011.

[42] K. Balakrishnan. *On the High Fidelity Simulation of Chemical Explosions and their Interaction with Solid Particle Clouds*. PhD thesis, Georgia Institute of Technology, 2010.

[43] C.-K. Kim and K-S. Im.

[44] C-K Kim, J.G. Moon, J-S Hwang, M-C Lai, and K-S Im. Afterburning of TNT explosive products in air with aluminum particles. *46th AIAA Aerospace Sciences Meeting, 7–10 January, Reno, Nevada, AIAA–2008–1029*, 2008.

[45] F.V. Sirotkin and J.J. Yoh. Modeling of afterburning from particle hydrodynamics of explosive product interface motion. *J. Mech. Sci. and Tech.*, 28:4781–4787, 2014.

[46] B.A. Khasainov and B. Veyssiere. Initiation of detonation regimes in hybrid two–phase mixtures. *Shock Waves*, 6:9–15, 1996.

[47] B. Veyssiere and B.A. Khasainov. Structure and multiplicity of detonation regimes in heterogeneous hybrid mixtures. *Shock Waves*, 4:171–186, 1995.

[48] Y. Grégoire, M.-O. Sturtzer, B.A. Khasainov, and B. Vyessière. Cinematographic investigations of the explosively driven dispersion and ignition of solid particles. *Shock Waves*, 24:393–402, 2014.

[49] S.B. Pope. *Turbulent Flows*. Cambridge University Press, New York, 2000.

[50] E. Fedina and C. Fureby. Numerical simulations of TNT afterburning at different Heights of Blast. In *22nd International Symposium on Military Aspects on Blast and Shock (MABS22)*, Bourges, France, 4–9 November 2012.

[51] E. Fedina and C. Fureby. Numerical simulation of afterburning during explosions. *28th International Symposium on Shock Waves, 17–22 July*, 2012. 2562.

[52] E. Fedina, K.C. Gottiparthi, C. Fureby, and S. Menon. *Coarse Grained Simulations and Turbulent Mixing*, chapter Combustion in Afterburning Behind Explosive Blasts. Cambridge Univeristy Press, 2016.

[53] S.B. Murray. Overview of the 2005 northen lights trials. In *Proc. 26th Int. Symp. Shock Waves*, Gottingen, Germany, 15-20 July 2007.

[54] R. Borghi. *Recent Advances in the Aerospace Sciences*, chapter On Structure and Morphology of Turbulent Premixed Flames, page 117. 1985.

[55] R. Borghi. Turbulent combustion modelling. *Prog. in Energy Comb. Sci.*, 14:613, 1988.

[56] G. Balakrishnan and F.A. Williams. Turbulent combustion regimes for hypersonic propulsion employing hydrogen–air diffusion flames. *J. Propulsion*, 10:434, 1993.

[57] I. Glassman and R.A. Yetter. *Combustion*. Academic Press, Elservier, 4 edition, 2008.

[58] T. Poinsot and D. Veynante. *Theoretical and Numerical Combustion*. Edwards, 2001.

[59] I.A. Johnston. The Noble–Abel equation of state: Thermodynamic derivations for ballistic modeling. Technical Report DSTO-TN-0670, Australian Government Department of Defence, Defence Science and Technology Organisation, 2005.

[60] J.A. Zukas and W.P. Walters, editors. *Explosive Effects and Applications*. Springer–Verlag, New York, USA, 1998.

[61] E.L. Lee, H.C. Hornig, and J.W. Kury. Technical Report UCRL–50422, Lawrence Livemore National Laboratory, 1968.

[62] F.F. Grinstein and K.K. Kailasanath. Three-dimensional numerical simulations of unsteady reactive square jets. *Combust. Flame*, 100:2–10, 1994.

[63] P. Sagaut. *Large Eddy Simulation for Incompressible Flows*. Springer Verlag, Heidelberg, 2001.

[64] C. Fureby. Comparison of flamelet and finite rate chemistry LES for premixed turbulent combustion. *AIAA–2007-1413, 45th AIAA Aerospace Sciences Meeting and Exhibit, 8 - 11 January 2007, Reno, Nevada*, 2007.

[65] R. Bensow and C. Fureby. On the justification and extension of mixed models in les. *J. Turbulence*, 8:54:1, 2008.

[66] J. Smagorinsky. General circulation experiments with the primitive equations.I: The basic experiment. *Month. Weath. Rev.*, 91:99–165, 1963.

[67] U. Schumann. Subgrid scale model for finite difference simulations of turbulent flows in plane channels and annuli. *J. Comput. Phys.*, 18:376–404, 1975.

[68] A.W. Cook and W.H. Cabot. Hyperviscosity for shock–turbulence interactions. *J. Comp. Phys.*, 203:379–385, 2005.

[69] J. von Neumann and R.D. Richtmyer. A method for the numerical calculations of hydrodynamical shocks. *J. Appl. Phys.*, 21:232–237, 1950.

[70] E.J. Caramana, M.J. Shashkov, and P.P. Whalen. Formulations of artificial viscosity for multi-dimensional shock wave computations. *J. Comp. Phys.*, 144:70–97, 1998.

[71] M. Germano, U. Piomelli, P. Moin, and W.H. Cabot. A dynamic subgrid–scale eddy viscosity model. *Phys. Fluids A*, 3:1760–1765, 1991.

[72] J. Boris. *Whither Turbulence? Turbulence at Crossroads*, chapter On Large Eddy Simulation using Subgrid Turbulence Models, page 344. Springer, 1990.

[73] J. Boris, F. Grinstein, E. Oran, and R. Kolbe. New insights into large eddy simulation. *Fluid Dynamics Research*, 10:199, 1992.

[74] F.F. Grinstein, L. Margolin, and B. Rider, editors. *Implicit Large Eddy Simulation: Computing Turbulent Fluid Dynamics*. Cambridge University Press, 2007.

[75] F.F. Grinstein and C. Fureby. On flux–limiting–based Implicit Large Eddy Simulation. *ASME J. Fluids Engng.*, 129:1483, 2007.

[76] D. Drikakis, M. Hahn, F.F. Grinstein, C.R. DeVore, C. Fureby, M. Liefvendahl, and D.L. Youngs. *Numerics for ILES: Limiting Algorithms*, chapter 4a. Cambridge University Press, 2007.

[77] P.J. O'Rourke and F.V. Bracco. Two scaling transformations for the numerical computation of multidimensional unsteady laminar flames. *J. Comp. Physics*, 33:185, 1979.

[78] B.F. Magnussen. On the structure of turbulence and generalized eddy dissipation concept for chemical reactions in turbulent flow. *19th AIAA Aerospace Meeting*, 1981.

[79] E. Baudoin, K.J Nogenmyr, X.S. Bai, and C. Fureby. Comparison of les models applied to a bluff body stabilized flame. *AIAA 2009-1178*, 2009.

[80] V. Sabelnikov and C. Fureby. LES combustion modelling for high re flames using a multi-phase anology. *Comb. & Flame*, 160:83–96, 2013.

[81] P. Gerlinger. Investigation of an assumed pdf approach for finite rate chemistry. *Comb. Sci & Tech.*, 175:841, 2003.

[82] G. Bulat, W.P. Jones, and A.J. Marquis. Large eddy simulation of an industrial gas turbine combustion chamber using the sub-grid pdf method. *Proc. Comb. Inst*, 34:3155, 2013.

[83] M. Berglund, E. Fedina, C. Fureby, J. Tegner, and V. Sabel'nikov. Finite rate chemistry large–eddy simulation of self–ignition in a supersonic combustion ramjet. *AIAA Journal*, 48:540–550, 2010.

[84] M. Chapuis, C. Fureby, E. Fedina, N. Alin, and J. Tegn□r. LES modeling of combustion for propulsion applications using OpenFOAM. *ECCOMAS CFD*, 2010.

[85] C. Fureby. A comparative study of flamelet and finite rate chemistry LES for a swirl stabilized flame. *ASME J. Engineering for Gas Turbines & Power*, 134(041503 (13 pages)), 2012. http://dx.doi.org/10.1115/1.4004718.

[86] M. Chapuis, E. Fedina, C. Fureby, K. Hannemann, S. Karl, and J. Martinez Schramm. A computational study of the HyShot II combustor performance. *Proc. Comb. Inst.*, 34:2101, 2013.

[87] M. Tanahashi, M. Fujimura, and T. Miyauchi. Coherent fine scale eddies in turbulent premixed flames. *Proc. Comb. Inst.*, 28:5729, 2000.

[88] P.K. Yeung, S.B. Pope, and B.L. Sawford. Reynolds number dependence of lagrangian statistics in large numerical simulations of isotropic turbulence. *J. Turb.*, 7:N58, 2006.

[89] B. van Leer. Towards the ultimate conservative difference schemes: A second order sequel to Godunov's method. *J. Comp. Phys.*, 32:101–136, 1979.

[90] G.D. Albada, B. van Leer, and W.W. Roberts. A comparative study of computational methods in cosmic gas dynamics. *Aston. Astrophys.*, 108:76–84, 1982.

[91] S. Gottlieb and C.-W. Shu. Total variation diminishing Runge–Kutta schemes. *Mathematics of Computation*, 67:73–85, 1998.

[92] R.A. Yetter and F.L. Dryer. *Microgravity Combustion: Fire in Free Fall*, chapter Metal particle combustion and classification, pages 419–478. 2001.

[93] M.W. Beckstead, Y. Liang, and K.V. Pudduppakkam. Numerical simulation of single aluminum particle combustion (review). *Comb. Explosion and Shock Waves*, 41:622–638, 2005.

[94] C. Crowe, M. Sommerfeld, and Y. Tsuji. *Multiphase Flows with Droplets and Particles*. CRC Press, Boca Raton, USA, 1998.

[95] S. Gallier, F. Sibe, and O. Orlandi. Combustion response of an aluminum droplet burning in air. *Proc. Comb. Inst.*, 33:1949–1956, 2011.

[96] Y. Liang and M.W. Beckstead. Numerical simulation of quasi–steady, single aluminum particle combustion in air. *AIAA 98–0254*, 1998.

[97] O.G. Glotov and V.A. Zhukov. The evolution of $100-\mu$m aluminum agglomerates and initially continuous aluminum particles in the flame of a model solid propellant. II. results. *Comb. Explosion & Shock Waves*, 44:671–680, 2008.

[98] W. Ingignoli. *Etude de la formation et de la propagation des detonations dans des suspensions de particules d'aluminium en atmosphere oxydante ou reactive*. PhD thesis, Universite de Poitiers, 1999.

[99] T. Bazyn, H. Krier, and N. Glumac. Evidence for the transition from the diffusion–limit in aluminum particle combustion. *Proc. Comb. Inst*, 31:2021–2028, 2007.

[100] A.L. Corcoran, V.K. Hoffmann, and E.L. Dreizin. Aluminum particle combustion in turbulent flames. *Comb. & Flame*, 160:718–724, 2013.

[101] R.A. Yetter, G.A. Risha, and S.F. Son. Metal particle combustion and nanotechnology. *Proc. Comb. Inst.*, 32:1819–1838, 2009.

[102] J. Servaites, H. Krier, and J.C. Melcher. Ignition and combustion of aluminum particles in shocked H_2O/O_2/Ar and CO_2/O_2/ar mixtures. *Comb. & Flame*, 125:1040–1054, 2001.

[103] C. Badiola, R.J. Gill, and E.L. Drezin. Combustion characteristics of micron–sized aluminum particles in oxygenated environments. *Comb. & Flame*, 158:2064–2070, 2011.

[104] P. Lynch, H. Krier, and N. Glumac. A correlation for burn time of aluminum particles in the transition regime. *Proc. Comb. Inst.*, 32:1887–1893, 2009.

[105] R.J. Gill, C. Badiola, and E.L. Drezin. Combustion times and emission profiles of micron–sized aluminum particles burning in different environments. *Comb. & Flame*, 157:2015–2023, 2010.

[106] M.W. Beckstead. Correlating aluminum burning times. *Comb. Explosion and Shock Waves*, 41:533–546, 2005.

[107] N. Zettervall, E. Fedina, K. Nordin-Bates, E. Heimdal Nilsson, and C. Fureby. Combustion les of a multi-burner annular aero-engine combustor using a skeletal reaction mechanism for jet-a air mixtures. In *AIAA – 2015–4020*, 2015.

[108] N. Zettervall, K. Nordin-Bates, E. Heimdahl Nilsson, and C. Fureby. Large eddy simulation (LES) of a premixed bluff body stabilized flame using global and skeletal reaction mechanisms. *Comb. & Flame*, 179:1–22, 2016.

[109] W.J. Pitz and C.K. Westbrook. A detailed chemical kinetic model for gas phase combustion of TNT. *Proc. Comb. Inst.*, 31:2343–2351, 2007.

[110] T.D Tran, R.L. Simpson, J. Maienschein, and C.M. Tarver. Thermal decomposition of trinitrotoluene (TNT) with a new one–dimensional time to explosion (ODTX) apparatus. *32nd International Conference of Institute of Chemistry Technology, Karlsruhe, Germany*, 2001.

[111] J. Akhavan. *The Chemistry of Explosives*. RCS Paperbacks, 2 edition, 2004.

[112] A.M. Starik, P.S. Kuheshov, A.S. Shapirov, N.S. Titova, and C-J Tsay. Numerical analysis of nanoaluminium combustion in steam. *Comb. & Flame*, 161:1659–1667, 2014.

[113] A.S. Shapirov, N.S. Titova, and A.M. Starik. Evaluation of reaction rate constants for the gas-phase $Al - CH_4$-air combustion chemistry. *Comb. Theory and Modell.*, 16:842–868, 2012.

[114] L. Catoire, J-F Legendre, and M. Giraud. Kinetic model for aluminum-sensitized ram accelerator combustion. *J. Prop. Power*, 19:196–202, 2003.

[115] Y. Huang, G.A. Risha, V. Yang, and R.A. Yetter. Analysis of nano-aluminum particle dust cloud combustion in different oxidizer enviroments. In *AIAA – 2005–0738*, 2005.

[116] E.B. Washburn, J.N. Trivedi, L. Catoire, and M.W. Beckstead. The simulation of combustion of micrometer-sized aluminum particles with steam. *Comb., Sci. & Tech.*, 180:1502–1517, 2008.

[117] B.T. Bojko, P.E.DesJardin, and E.B. Washburn. On modeling the diffusion to kinetically controlled burning limits of micron-sized aluminum particles. *Comb. & Flame*, 161:3211–3221, 2014.

[118] W.E. Baker. *Explostions in Air*. University of Texas Press, Austin and London, 1973.

[119] CONWEP–conventional weapons, 1992. Collection of conventional weapons calculations based on T–5–855-1, “Fundamentals of Protective Design for Conventional Weapons”.

[120] P.K. Kundu and I.M. Cohen. *Fluid Mechanics*. Elsevier Academic Press, San Diego, USA, 3 edition, 2004.

[121] E.E. Meshkov. One approach to the experimental study of hydrodynamic instabilities: Creation of a gas–gas interface using the dynamic tecnique. In *Proc. 5th International Workshop on Compressible Turbulent Mixing*, 1996.

Acknowledgements

This work was sponsored by the Swedish Armed Forces.

I would like to express my deepest gratitude to everybody who has supported me during this work. In particular,

To my supervisors:
Prof. Bai, thank you for enabling this dissertation.
Prof. Fureby, I'm very grateful that during my first month on the job you told me that I'll be working with afterburning and then let me research, develop and grow with the subject under your subtle guidance. I've very much appreciated your continuous encouragement during the years and all inspiring discussions when my mood and confidence were low.

To my colleagues:
My colleagues in the CFD&C group at FOI, Grindsjön, I very much value your support, and also your patience and consideration when I occasionally occupied most of the cluster and the post-processing machines while running and post-processing this work. Many many thanks (and semlor) to Jon Tegnér, for providing and maintaining the extra storage for these simulations over the years, and to Oskar Parmhed, Niklas Zettervall and Kristian Petterson for proofreading parts of this thesis.

Jonas Lundgren, Roger Berglund, Isak Sommarström and Björn Gregorsson, thank you for conducting the experiments and measurements, despite my confused directions.

To my family:
My mother, thank you for unlimited love and motivation.
My father, thank you for the inspiration to go into research.
My brother, thank you for teaching me perseverance, stubbornness and to never give up.
Mattias, thank you for helping me with the Matlab film analysis and for putting up with me during the final years of this work, 2.

Author Contributions

Paper I:
Predicting Mixing and Combustion in the Afterburn Stage of Air Blasts

E. Fedina, C. Fureby, A. Helte (2010)
48th AIAA Aerospace Sciences Meeting Including the New Horizons Forum and Aerospace Exposition
4 - 7 January 2010, Orlando, Florida
AIAA - 2010-773

In this paper the unconfined and semi-confined condensed phase explosions of TNT and HMX are studied using Large Eddy Simulations (LES) based on the unsteady, compressible, reacting, multi-species Navier-Stokes equations (NSE) with a Nobel-Able thermal equation of state. The simulation results are validated against the experiments. The analysis of the mixing and afterburning of TNT explosions in free air and near the ground indicates that the combustion region of detonation products and air is determined by the vorticity patterns, induced by the Richtmeyer-Meshkov instabilities that arise during the explosion. When explosive is detonated above ground, the ground affects the shock propagation, thereby changing the orientation of the vorticity, giving the afterburning a mushroom shape, however the mixing and combustion are found to follow the same principles as for the free air detonation.

E. Fedina set-up and conducted the simulations, part of the analysis and co-wrote the paper with the co-authors.

Paper II:
Numerical Simulation of Afterburning During Explosions

E. Fedina, C. Fureby (2011)
28th International Symposium on Shock Waves

17 - 22 July 2011, Manchester, UK

In this paper the unconfined and semi-confined TNT air blasts are studied using Large Eddy Simulations (LES) and the effects of confinement on mixing and combustion during an air blast are examined. The mixing layer evolution is found to be closely connected to the shock propagation pattern and its consequent effects of the generation of flow instabilities. A further analysis of afterburning confirms the correlation of the shock generated instabilities sustaining the mixing as well as fueling the combustion regions around the vorticity structures where the afterburning occurs.

E. Fedina set-up and conducted the simulations, performed the presented analysis and wrote the paper with the input from co-author.

Paper III:
Investigating Ground Effects on Mixing and Afterburning During a TNT Explosion

E. Fedina, C. Fureby (2013)
Shock Waves, vol. 23, pp. 251—261

In this paper, the unconfined and semi-confined condensed phase explosions of TNT are studied using LES. The analysis of the mixing and afterburning of TNT explosions in free air (unconfined) and near the ground (semi-confined) indicates that the combustion region of detonation products and air is determined by the vorticity patterns, which are induced by the Richtmeyer–Meshkov instabilities that arise during the explosion. When the explosive is detonated in the vicinity of a surface, the surface affects the shock propagation by creating complex shock systems, thereby changing the orientation of the vorticity, giving the afterburning a mushroom shape, and increasing performance of an explosive charge by prolonging the existence of the mixing layer and thereby the afterburning.

E. Fedina set-up and conducted the simulations, performed the presented analysis and wrote the paper with the input from co-author.

Paper IV:
Combustion in Afterburning Behind Explosive Blasts

E. Fedina, K.C. Gottiparthi, C. Fureby, S. Menon (2016)
in *Coarse Grained Simulation and Turbulent Mixing*, Ed. F.F. Grinstein
Cambridge University Press, New York, USA, pp. 393–432

In this chapter the work done by authors in the field of Coarse Grained Simulations (CGS) of afterburning is presented. This work includes afterburning of trinitrotoluene (TNT) in unconfined air and at different HoB as well as multi-phase afterburning of TNT/aluminum and nitromethane (NM)/steel in a spherical sector domain. The main objective of this chapter is to examine the use of combustion CGS to elucidate the physical processes involved in unconfined air and near-ground air blasts, demonstrate what affects the HoB has on the afterburning and how metal particles affect the combustion. The aim is to capture the most significant stages of turbulent mixing, involving the initial blast wave, secondary and reflected shocks, possible implosions and the constant mixing stage(s), providing further knowledge of the complicated processes during a condensed phase explosion event.

E. Fedina was the responsible author for this chapter. She edited and complied the text from all authors, including her own. She also developed the two-phase, Al combustion code used in TNT/Al simulations presented in this chapter. She set-up and conducted the simulations, the analysis and wrote the material in Sections 13.4 and 13.5.

Paper V:
Analysis of Heat-Release During TNT/Aluminum Afterburning by Means of Numerical Simulations

E. Fedina, C. Fureby (2017)
Proceedings of the Combustion Institute, vol. 36, pp. 2841–-2848

The present study investigates the afterburning from an explosion of a spherical TNT charge containing aluminum particles at four different HoB, to demonstrate that numerical simulations can facilitate the evaluation of the performance of EBX. The simulations are conducted using a two-phase Large Eddy Simulation model in Euler-Lagrange form, incorporating interaction between gaseous and solid phases by means of a two-way coupling. Finite rate Arrhenius chemistry is used to simulate the afterburning process, thereby enabling the examination of the separate heat-release contributions from carbon and aluminum afterburning reactions. The simulation results indicate the heat-release contribution from the aluminum reactions is significantly higher than from the carbon reactions, also does the heat-release from aluminum reactions, for all HoBs, fluctuate more in time compared to the heat-release from the carbon reaction. Most of the heat-release from carbon seems to occur at early times, after which the afterburning of carbon stagnates at a steady rate. The heat-release from aluminum reactions is more intermittent and is thought to be closely connected to the physical environment inside the mixing layer.

E. Fedina conducted the simulations, the analysis and wrote the paper.

Lund University
Faculty of Engineering
Department of Energy Science

ISBN 978-91-629-0221-6
ISSN 0282-1990
ISRN LUTMDN/TMHP-17/1132-SE